Near-surface void characterization and sensitivity analysis using enhanced processing procedures on passive Multi-Channel Analysis of Surface Waves (MASW) data

By

Jeffery Jordan Nolan

Submitted to the graduate degree program in Geology and the Graduate Faculty of the University of Kansas in partial fulfillment of the requirements for the degree of Master of Science.

_____

Chairperson Richard D. Miller

_____

Douglas Walker

_____

Jennifer A. Roberts

_____

Steven D. Sloan

Date Defended: May 9, 2016

The Thesis Committee for Jeffery Jordan Nolan

certifies that this is the approved version of the following thesis:

Near-surface void characterization and sensitivity analysis using enhanced processing procedures on passive Multi-Channel Analysis of Surface Waves (MASW) data

_____

Chairperson Richard D. Miller

Date approved: July 14, 2016

ABSTRACT

Enhanced processing procedures on passive multichannel analysis of surface-waves (MASW) data were utilized to identify velocity anomalies above known salt solution voids in Hutchinson, Kansas, likely caused by the changing stress field due to the migration and/or expansion of the void. Previous geophysical studies within the study area provided information about the origin of the dominant passive surface-wave energy, allowing for an optimal spread orientation consisting of both 1D survey lines and a 2D grid. Occasional passing trains throughout the night generated surface-wave energy ranging from ~4 Hz to ~20 Hz for most recorded events. The use of the 2D grid allowed for identification of the orientation of wave propagation to correct the high apparent velocities caused by the oblique source orientation. Following acquisition, enhanced processing procedures such as time window stacking, percent keep, and source stacking, generated an overtone image with a higher signal-to-noise ratio and more pronounced fundamental mode energy. This visual improvement facilitated the extraction of fundamental mode energy, ultimately increasing the accuracy of the final shear-wave velocity profile. Velocity anomalies within the velocity profiles could likely be attributed to the changing of the stress field during the movement of the void. As the void expands laterally, the roof span increases. The increasing roof span likely increases the stress and shear velocity in the overburden load causing high-velocity haloes in the velocity profile. When the roof span becomes too large to support the overburden load, the roof rock will collapse, causing the migration of the void. Upon collapse, the non-collapsed overburden should accumulate stress due to the lack of underlying support, while the collapsed rock (rubble) should decrease in shear-wave velocity.

ACKNOWLEDGMENTS

I would like to thank Rick Miller, Shelby Peterie, Tyler Schwenk, Brett Bennett, Brett Wedel, Joe Anderson, Brett Judy, Ryan Nelson, and Brian Brooks for their help in the acquisition of these data within this study. I also thank Shelby Peterie, Tyler Schwenk, and Julian Ivanov for their help in the processing of these data. All of their help was greatly appreciated. I would also like to thank Steve Sloan for the assistance in getting accepted into graduate school, as well as, funding part of my GRA position. I would also like to thank entire committee, Rick Miller, Jen Roberts, Doug Walker, and Steve Sloan for their time and input on this project.

TABLE OF CONTENTS

TABLE OF FIGURES

INTRODUCTION

Sinkholes caused by the collapse of known salt solution voids pose serious threats to the citizens in and around Hutchinson, Kansas. While not all are in imminent danger of collapse, the status of the majority of these subsurface voids remains unknown. The accumulation of stresses overlying said voids can be potential indicators of voids that are nearing collapse, while the inverse could indicate signs of partial collapse beneath the ground surface. Stress anomalies overlying these salt voids can be very difficult to identify, but can provide valuable information about the status of the void, as well as the overlying units. The shear-wave velocity is directly related to shear-stress, making anomalies in the shear-wave velocity field ideal for identifying relative changes in shear-stress. Multi-channel analysis of surface-waves (MASW) ultimately generates a 2D vertical shear-wave velocity profile through an inversion of the surface-wave seismic data. These velocity profiles can then be analyzed to illuminate anomalous velocity zones.

Geologic Setting

The test site for this project was in Hutchinson, Kansas. Hutchinson is in south-central Kansas in the Sedgwick Basin, which is south-east of the Central Kansas Uplift (CKU) and east of the Pratt Anticline (Figure 1). The surface, along with the upper 20 meters at this specific site, consists of coarse alluvial bedded loose sands and gravels and the Pleistocene Equus beds (Figure 2). These Pleistocene Equus beds act as the regional unconfined aquifer (Figure 3). This aquifer overlies the Sumner Group, which consist of the Ninnescah Shale and the Wellington formation within the site location.

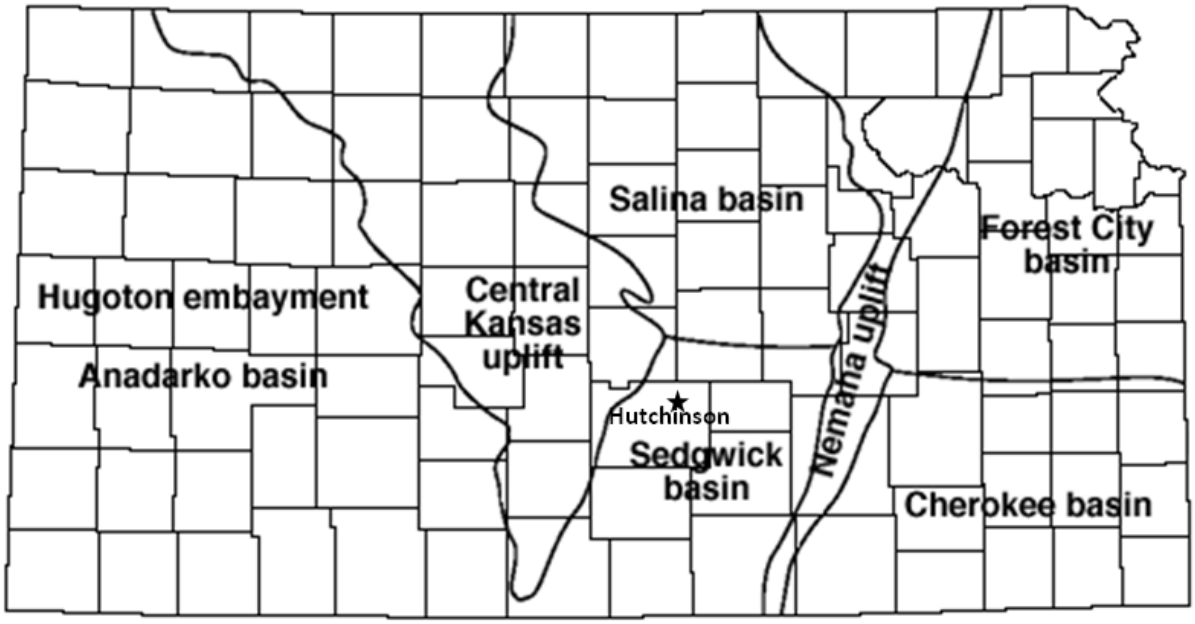

Figure 1: Regional structural features across the state of Kansas with the city of Hutchinson highlighted by the black star (modified from Baars et al., 1989)

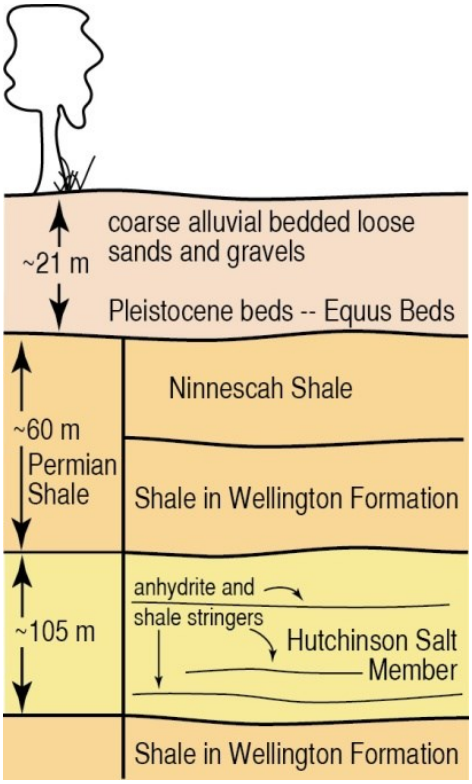

Figure 2: Cartoon representing the generalized geology based on common seismic reflectors of the Hutchinson, Kansas, area (modified (Miller, 2007) from Walters, 1978).

The Permian aged Wellington formation is primarily a shale sequence in most of south-central Kansas (Tasch, 1964). The Wellington formation consists of the Upper Wellington, the Hutchinson salt member, and the Lower Wellington. Although generally discussed in isolation, the Hutchinson salt member actually lies within the Lower Wellington. Both the Upper and Lower Wellington formations contain mostly shales, while the Hutchinson salt member contains interbedded salt, anhydrites, and shale stringers (Figure 4). A cross section approximately 1.5 km (1 mile) north of the study area provides an understanding of the approximate subsurface depth of key formations within the study area (Figure 5 and Figure 6). From these wells, which are much closer than the well in Figure 4, the top of the bedrock is approximately 20 meters deep. The top of the Upper Wellington formation is approximately 65 meters deep. The top of the 3-finger dolomite is approximately 70 meters deep, and the top of the Hutchinson salt is approximately 125 meters deep.

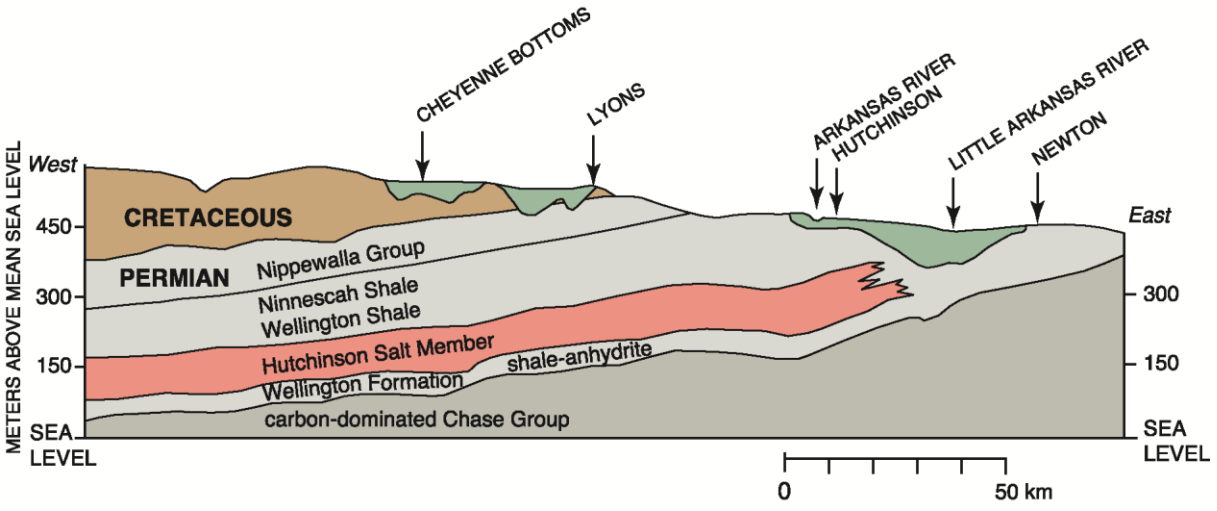

Figure 3: Generalized geologic cross-section with major units identified and mapped from well data (modified (Miller, 2007) from Spinazola et al., 1985).

The Hutchinson salt member as a whole is laterally continuous with intermittent interbeds of salt and shale continuous for only a few kilometers (Walters, 1978). The Hutchinson salt member stretches from central Kansas, northwestern Oklahoma, into the northeast portion of the Texas panhandle (Figure 7). Halite-rich marine cycles of variable thickness and purity alternate throughout the Hutchinson salt member across the region (Watney et al., 1988). Varying from approximately 75 meters thick up to about 150 meters thick, the Hutchinson salt member is approximately 65 meters thick in the study area (Walters, 1978).

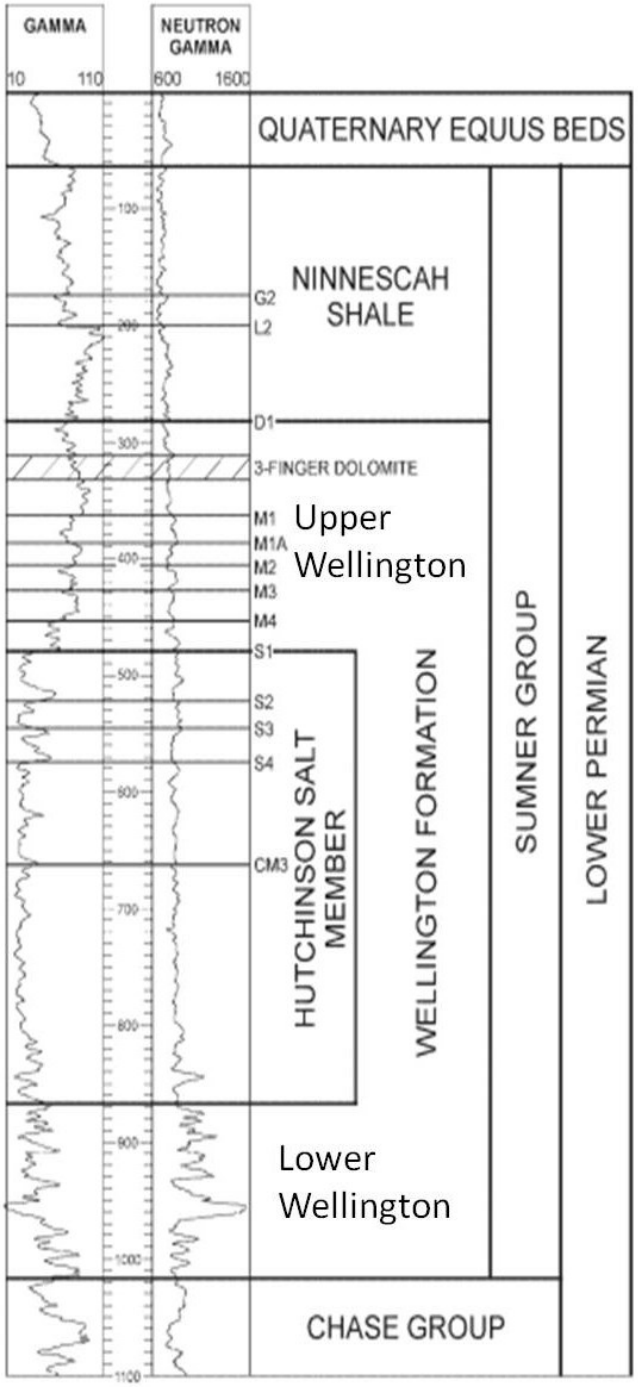

Figure 4: Geologic section approximately 8 km (5 miles) west of the study area (modified from Watney et al., 2003).

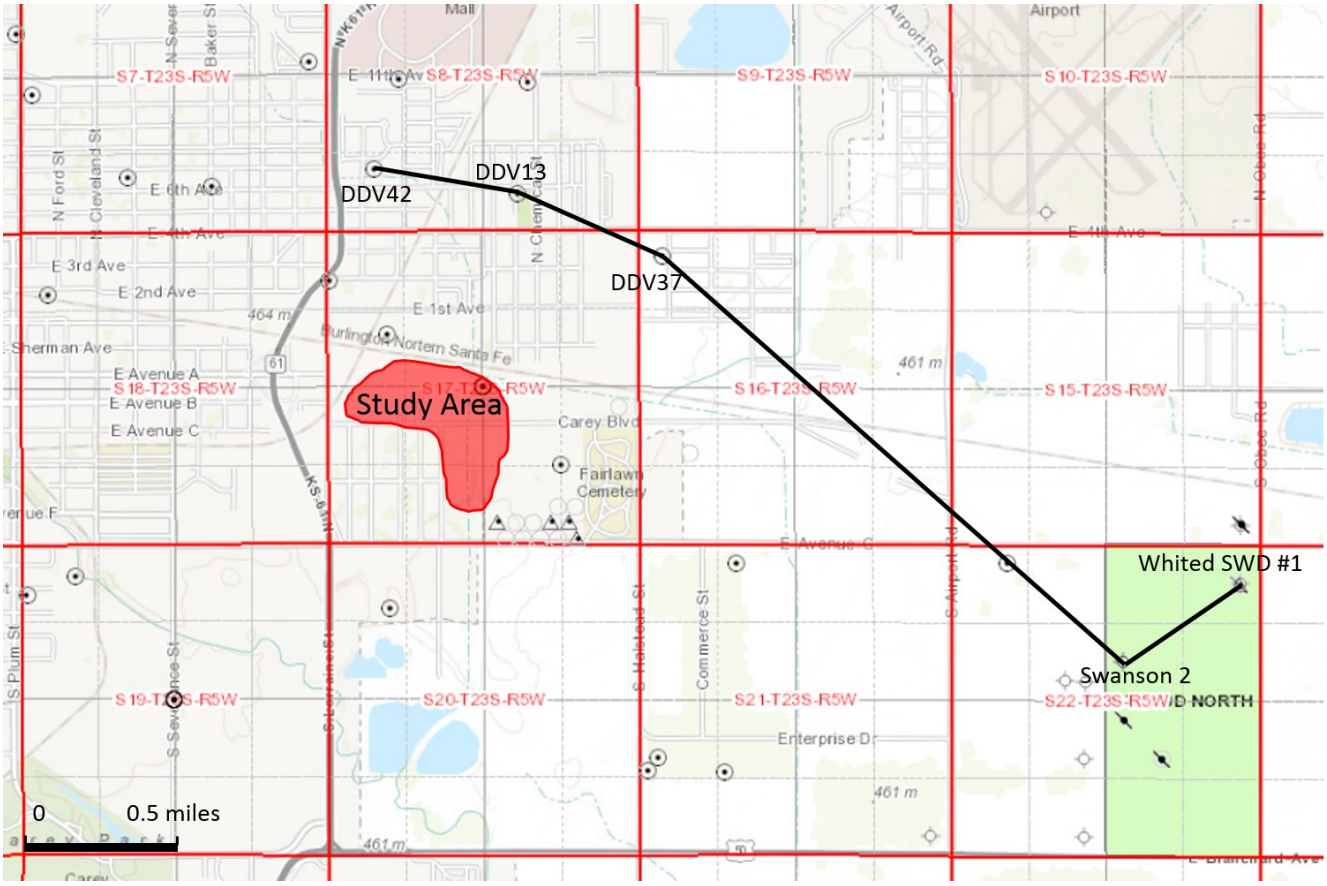

Figure 5: Map view of the following cross section with the study area highlighted in red. Wells included in this cross section include DDV42, DDV13, DDV37, Swanson 2, and Whited SWD #1.

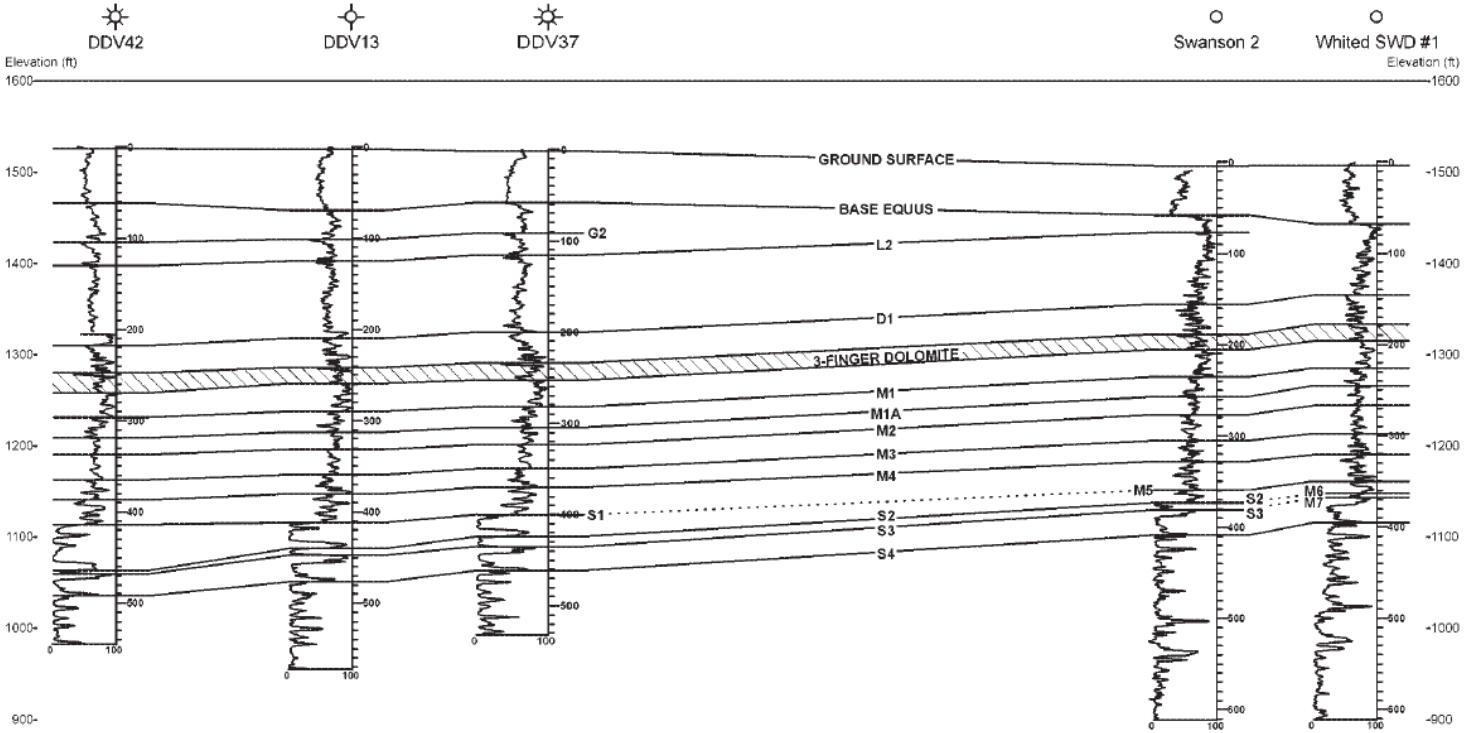

Figure 6: Cross section through the subsurface approximately 1.5 km (1 mile) north of the study area in Hutchinson, KS (Watney et al., 2003).

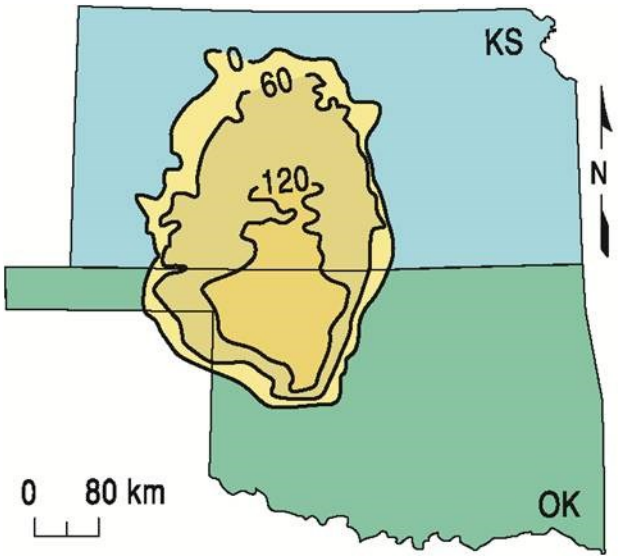

Figure 7: Isopach map representing the thickness of the Hutchinson salt member with a contour interval of 60 meters. The lateral continuity across Kansas, Oklahoma, and northern Texas can also be observed (modified (Miller, 2007) from Walters, 1978).

During the early-to-mid 1900's, salt mining in this area was very popular (Taft, 1946; Walters, 1978). Salt miners would dissolve the salt in the Hutchinson salt member, and leave various sized voids in the salt interval following extraction of the brine. Although the voids manifest themselves within the Hutchinson salt member, or the Lower Wellington, this study primarily focusses on tracking potential void movement into the overlying units. Directly overlying the Hutchinson salt is the Upper Wellington, consisting primarily of shale with thin beds of gypsum, anhydrite, dolomite, and siltstone. The most prolific interbed within the Upper Wellington is the '3-finger dolomite' (~70 m deep), which gets its name from the pattern formed by the three thin dolomite beds of low natural gamma ray signature on the well log (Nissen and Watney, 2003).

Overlying the Upper Wellington is more shale within the Ninnescah Shale, which acts as the bedrock in this area. The contact between the Upper Wellington shales and the Ninnescah shale is indistinguishable on well logs because of the similarities of the rock types (Leonard and Kleinschmidt, 1976). The Ninnescah shale mainly consists of brick-red shale, but also includes some beds of green shale and thin argillaceous limestone near the base, along with a regionally consistent limestone approximately 1 meter thick in the middle of the formation (Williams and Lohman, 1949). Also included within the Ninnescah Shale are thin beds of light-gray and red sandstone ranging from very fine to medium grain sizes. These thin sandstones are located near the top of the shale interval. Gypsum can be found in veins throughout the shales within the Ninnescah shale (Williams and Lohman, 1949).

MASW Background

The MASW method generally uses surface-wave seismic data acquired in a roll-along manner along a profile line (Miller et al., 1999). Each record is acquired at a different shot station along the profile line and is transformed into a plot of phase velocity—frequency domain known as an overtone image (Park et al., 1998; Park et al., 1999a). Fundamental mode and several higher mode dispersion curve trends are visible depending on the geology (Park et al., 1999b). However, generally the fundamental mode is the most uniquely identifiable and is elemental in surface-wave processing. An overtone image is a plot of frequency vs. phase velocity. A dispersion curve is a curve on an overtone image that represents the change in velocity with frequency. In order to use this curve quantitatively, points are picked along the maximum amplitude of the fundamental mode dispersion curve.

Each dispersion curve in a succession of shots along a profile line is inverted into a 1D vertical shear-wave velocity (V_S) profile representative of the midstation of the record (Xia et al., 1999). The individual 1D V_S profiles are then sutured together producing a 2D V_S cross section (Miller et al., 1999). Using a priori data, if available, interpolation between the measured velocities of the 1D inversion produces a continuous 2D velocity profile.

MASW History

The concepts of MASW are loosely derived from the spectral analysis of surface-waves (SASW) engineering approach. Introduced in the early 1980's (Nazarian and Stokoe II, 1983; Nazarian et al., 1983), SASW uses only two geophones with varying source-receiver offsets and receiver spacings. These offsets and spacings determine the wavelengths of recorded energy. Different wavelengths represent a different depth of investigation; therefore multiple measurements are required to reach the desired range of sampling depth and vertical resolution. The numerous tests required increases the amount of time in the field, and compromise the uniqueness of interpreted energy.

The MASW method tries to overcome a few of the weaknesses of the SASW method, primarily the presence of noise, identification of higher modes, and acquisition time (Park et al., 1997, Park et al., 1999b). MASW includes concepts from the SASW approach and the popular seismic reflection common midpoint (CMP) concept. The SASW approach over a multichannel record in MASW provides for faster acquisition and many more options while processing. The rapid production of overtone images within the MASW method allow the efficient interrogation of the dispersive properties of each record. The common seismic reflection CMP concept for

field layout is incorporated into MASW acquisition providing a linear spread of geophones. Using these two approaches simultaneously allows for efficient acquisition of the raw surface-wave data and results in a continuous 2D shear-wave velocity profile.

In the same fashion that surface-waves are commonly considered noise on seismic reflection and seismic refraction surveys, body-waves (direct, refracted, and reflected waves) are considered noise in a MASW survey. However, while the processing of seismic reflection data is facilitated by the filtering or muting of the surface-waves, MASW does not require the filtering or muting of the body waves. Body wave "noise" can be identified on a multi-channel record by coherency, apparent velocity, frequency, and arrival times, and show up significantly different than surface-waves on overtone images.

The MASW method has even aided in the development of new surface-wave methods. The refraction microtremor analysis (ReMi) combines the urban utility and ease of microtremor array techniques with the operational simplicity of the SASW technique and the shallow accuracy of the MASW technique (Louie, 2001). By recording urban microtremors on a linear array of a large number of lightweight seismometers, or geophones, the ReMi method achieves the fast and easy field data collection without any need for the time-consuming heavy source required for SASW and MASW work (Louie, 2001). The MASW method allows for the recording of "background" noise for use in passive surface-wave analysis as well (Park and Miller, 2005). By retaining all the original seismograms, and by applying a time-domain velocity analysis technique, as is done in MASW, the analysis described here can separate Rayleigh waves from body waves, air waves, and other coherent noise (Louie, 2001). A study by the USGS compared

the passive ReMi method with the active MASW method (Asten and Boore, 2005; Stephenson et al., 2005). This study showed weight drop sources commonly used in the active MASW technique generated much higher frequency surface-wave energy (to at least 30 Hz) than was generally observed in the microtremor data (Figure 8) (Asten and Boore, 2005; Stephenson et al., 2005). While the two techniques were processed as similarly as possible, the final 1D velocity profile (1D because only one dispersion curve for each were utilized) showed both methods are comparable to about 30 m depth (Asten and Boore, 2005; Stephenson et al., 2005). Deeper than 30 m, the MASW result showed increased velocity to about 70 m, where the two solutions converged again (Asten and Boore, 2005; Stephenson et al., 2005).

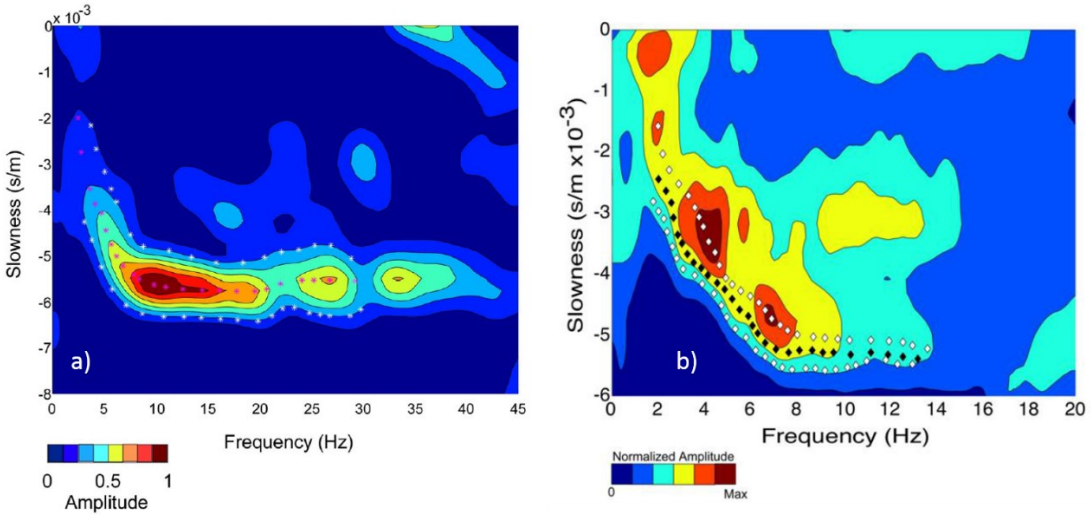

Figure 8: The overtone images produced from an accelerated weight drop (a) and passive microtremor technique (b). The weight drop produced significantly higher frequencies than the microtremor technique, while the microtremor method has much more defined lower frequency signal (modified from Asten and Boore, 2005; Stephenson et al., 2005)

MASW Theory

The two most common types of surface-waves are Rayleigh waves and Love waves (Dobrin and Savit, 1988). Rayleigh waves, or ground roll, account for more than two thirds of the seismic energy transmitted into the ground for compressional wave sources (Heisey et al., 1982). In a layered medium in which seismic velocity changes with depth, both types of surface-waves possess the dispersion property, which can be indicative of elastic moduli of near-surface earth materials: different wavelengths have different penetration depth and propagate with different velocities (Haskell, 1953). Shorter wavelengths will sample the shallower depths while the longer wavelengths will penetrate deeper into the subsurface. As a rule of thumb, the depth of penetration of the ground roll is approximately equal to its wavelength (Richart et al., 1970), while shear-wave velocities can be reasonably calculated to a depth approximately half the longest recorded wavelength (Rix and Leipski, 1991). Each wavelength, and therefore frequency, has a specific velocity associated with it known as the phase velocity (Båth, 1973). There are several contributing parameters which influence the phase velocity: V_S, P-wave velocity (V_P), density (ρ), and Poisson's ratio (σ). Generally, the velocity of the ground roll is approximately 92% of the V_S, and can vary from approximately 88-95% dependent upon the Poisson's Ratio (Sheriff, 2002; Stokoe et al., 1994).

The MASW technique is composed of three components: acquisition of data, imaging of the overtone image, and inversion of the extracted dispersion curves. Acquisition parameters can dramatically affect the overall quality of the data (Ivanov et al., 2008). For example, using a shorter spread length will incompletely sample the long wavelengths, and therefore limit the sampling depth. However, shorter spread lengths will increase horizontal resolution because it

samples the average velocity over a smaller length. Selecting the correct combination of parameters (source-receiver offset, station spacing, source selection, record length, sample interval, etc.) maximizes data quality, as well as sampling the target depths at the desired resolution.

The quality of the seismic data and the quality of the overtone images are not directly related, meaning good quality seismic data can still produce a poor overtone image. A poor overtone image can be contaminated by higher modes, lack desired broadband bandwidth, or just contain noise. The inverse is also true; a medium to poor quality seismic record can still produce a good overtone image depending on the velocity structure. A good overtone image, consisting of high-amplitude, high signal-to-noise ratio, broad bandwidth, and continuity is desired when extracting the fundamental mode dispersion curve (DC) energy (Figure 9) (Park et al., 2007). Using the Least Squares Approach, an iterative inversion of these dispersion curves can be used to calculate the depths associated with each individual frequency/velocity pick (Xia et al., 1999).

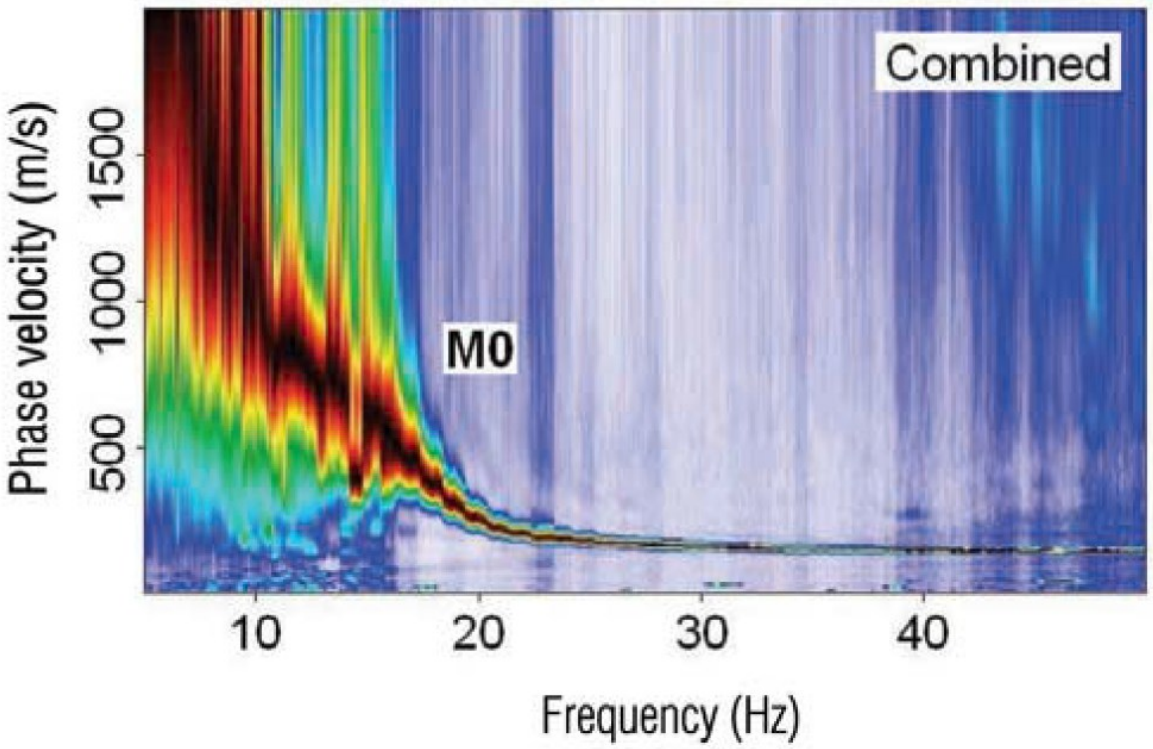

Figure 9: An example of a high quality dispersion curve that shows high-amplitude, high signal-to-noise ratio, broad bandwidth, and a continuous trend of the fundamental mode (M0) surface-wave energy (Park et al., 2007).

Active surveys have a known and controllable source, while passive surveys have an unknown or uncontrollable source. Both active surveys and passive surveys can be implemented using the MASW method. Active surveys use sources (hammer, weight drop, accelerated weight drop, air gun, or any other source capable of generating surface-waves) at a known distance (source-receiver offset) from the first receiver or geophone. Active MASW surveys use a linear spread of geophones, generally collecting data in a roll-along acquisition geometry.

A passive survey utilizes a source with an origin that may be unknown and/or uncontrollable. Passive surface-wave recording allows for interference of multiple uncontrolled seismic energy sources, likely considered noise in many active surveys, such as passing trains, manufacturing facilities, heavy vehicles on roadways, processing plants, heavy construction equipment, or a variety of other surface-wave sources (Louie, 2001; Park et al., 2008, Ivanov et al., 2013). Passive surveys can be advantageous in situations where active surveys are not producing the low frequencies required to reach the desired depths, site limitations restrict active sources such as an urban area, or the survey site is susceptible to high noise such as a high-traffic roadway. Passive MASW surveys are separated into 2 subcategories: roadside passive and remote passive (Figure 10) (Park et al., 2007).

Remote passive MASW surveys have been acquired using a 2D spread of geophones in patterns such as a cross, a circle, a square, or a sawtooth spread containing sharp bends. Symmetrical grids, or arrays, are preferred for the remote passive method because they lack bias in any particular direction (Leitner, 2015). The 2D array of the remote passive survey can be utilized for a regional 1D V_S profile, as well as provide the azimuthal direction of surface-wave energy when acquired simultaneously with other lines.

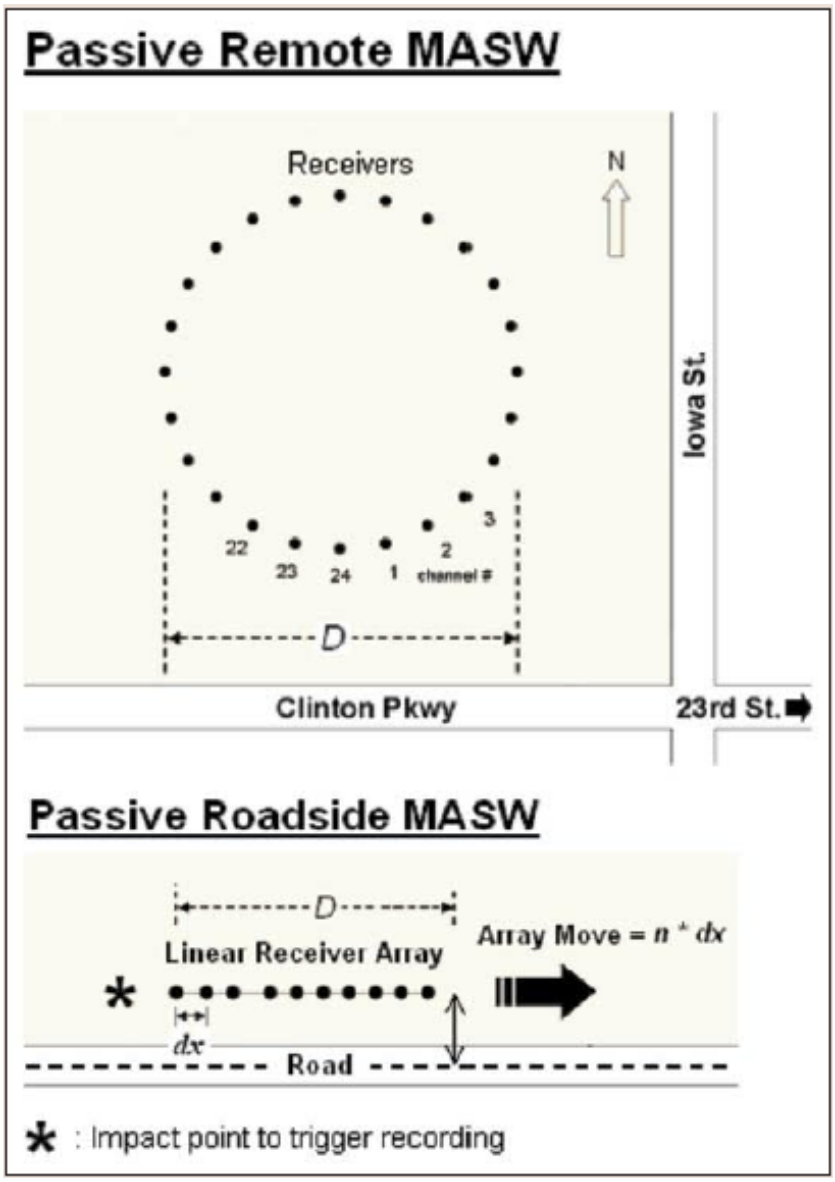

Figure 10: Schematic of data acquisition with passive remote and passive roadside MASW techniques (Park et al., 2007).

Roadside passive MASW surveys use the same linear array approach as the active MASW survey. Generally, the roadside passive method is used when the approximate source orientation is known. However, if the approximate source orientation is unknown, the roadside

passive method is vulnerable to elevated apparent velocities due to oblique surface-wave propagation (Park and Miller, 2006).

MASW Applications

Applications of the MASW method have included mapping bedrock, weak zone detection, fault/fracture zones, void detection, pavement characterization, structural interpretation, and identification of key stratigraphic units (Hayashi, and Inazaki, 2006; Miller et al., 1999; Ryden et al., 2004; Sloan et al., 2010; Socco et al., 2010; Watabe and Sassa, 2008).

The feasibility of a hydrophone streamer for surface-wave data acquisition has been tested and confirmed (Kaufmann et al., 2005). This hydrophone streamer has proven to record sufficient shear-wave velocities when compared to data acquired on land (Kaufmann et al., 2005). However, when surface-wave measurements are made at the interface between water and solid materials the wave is known as a Scholte wave, rather than a Rayleigh wave (Grant and West, 1965; Kaufmann et al., 2005). This can be very helpful in providing continuity in the survey when land conditions are heterogeneous, the area of interest is under water, and the transition zone from shallow marine to land. Multiple underwater applications using the MASW method have characterized stiffness distribution of water-bottom sediments in both shallow water and deep water environments (Park et al., 2005b).

The effects of an earthquake in Japan have even been analyzed using the surface-wave method (Hayashi and Hirade, 2008, Hayashi et al., 2008). The Noto Peninsula Earthquake produced variable shaking at the surface, which was suggested to be related to the change in

bedrock depth as measured using the surface-wave method (Hayashi and Hirade, 2008; Hayashi et al., 2008).

Joint analysis of refractions and surface-waves have been utilized to provide a valid initial V_S model for refraction tomography (Ivanov et al., 2006; Schuler, 2008). Near-surface shear-wave velocity profiles have also been created using refracted P-waves as a priori information in the inversion (Boiero and Socco, 2014).

In situations where the overlying units are stiffer than the underlying units, higher-modes (harmonic solutions to elastic wave equations (Haskell, 1953)) can be observed (Luke et al., 1996; Park et al., 1999c; Xia et al., 2003). These higher-modes and high-frequencies have been researched in great detail with varying results and impact on the accuracy of the final inverted velocity (Ivanov et al., 2010; Luo et al., 2007; Luo et al., 2008; O'Neill et al., 2005; Park et al., 1999c; Ryden et al., 2004; Xia et al., 2003; Xia et al., 2005; Xia et al., 2006; Xia et al., 2007a). Higher-modes can increase depth of investigation (Siavashpoo and Siahkoohi, 2012) if modes are clearly separated or can adversely affect the fundamental mode analysis procedure (Morton et al., 2015).

Backscattered surface-waves have also been used to detect near-surface voids (Sloan et al., 2010; Xia et al., 2006a; Xia et al., 2006c; Zeng et al., 2009). Data from 1D survey lines that were coincidentally interpreted to produce a pseudo-3D MASW cube was utilized as a pilot study for characterizing sinkholes (Park and Taylor, 2010). The velocity structure using this pseudo-3D surveying approach showed results reasonably consistent with the geologic cross section compiled from drilling and other geophysical methods (Park and Taylor, 2010).

Passive MASW has proven a popular technique when an active source is not available, the ambient noise or cultural noise overpowers active sources, site limitations restrict active sources, and to record lower frequencies and therefore image greater depths. Many use passive MASW to acquire data in areas with limited space to acquire a 2D receiver spread of geophones (Hayashi et al., 2005; Park et al., 2007; Park and Miller, 2006; Park and Miller, 2008). Aside from choosing the particular type of MASW survey most suited for the application, a combination of active MASW and passive MASW can increase the resolution and the depth of sampling (Park et al., 2005a; Yoon and Rix, 2004).

Collapse Process/Solution Mining

Subsidence processes can progress gradually or catastrophically due to the collapse, or movement of subsurface materials (Peng, 1992). These subsidence progressions commonly create sinkholes at the earth's surface. Sinkholes, also known as dolines, are very common in areas underlain by evaporites (Martinez et al., 1998).

Sinkholes within the dissolution mine fields in and around the city of Hutchinson, Kansas, have been associated with roof rock failure due to the mining of salt for over 90 years (Walters, 1978). Specifically, the single-well solution method was the most popular method for extracting salt in this area (Walters, 1978). The Solution Mining Research Institute defines solution mining as the mining of underground, water-soluble minerals, usually using one or more drilled wells to dissolve the minerals (in this case salt) with water.

The single-well method is utilized by injecting fresh water near the bottom of the salt interval and recovering the extracted brine solution near the top of the salt interval through a

multi-plumbed borehole (Figure 11) (Ege, 1979; Quiero, 1977). Top injection is an older technique that is often associated with some of the uncontrolled subsidences that have occurred in brine fields, and has largely been replaced by more sophisticated techniques, such as the air or oil pad method or the multi-well method (hydrofracture technique) (Ege, 1979; Quiero, 1977).

The air or oil pad method consists of an impermeable layer of air or oil at the top of the void to retard the dissolution of material from the roof of the cavity (Figure 12) (Ege, 1979; Quiero, 1977). Using this method, control of cavity geometry is maintained to keep a predetermined thickness of evaporite (in this case, salt) overlying the void (Ege, 1979; Quiero, 1977).

The multi-well method, or hydrofracture method, uses the oil industry technique of an injector and a producer (Figure 13) (Ege, 1979; Quiero, 1977). By injecting water into the injection well, and extracting the brine in the producing well, maximum control of extraction rates and cavity geometry is established (Ege, 1979; Quiero, 1977).

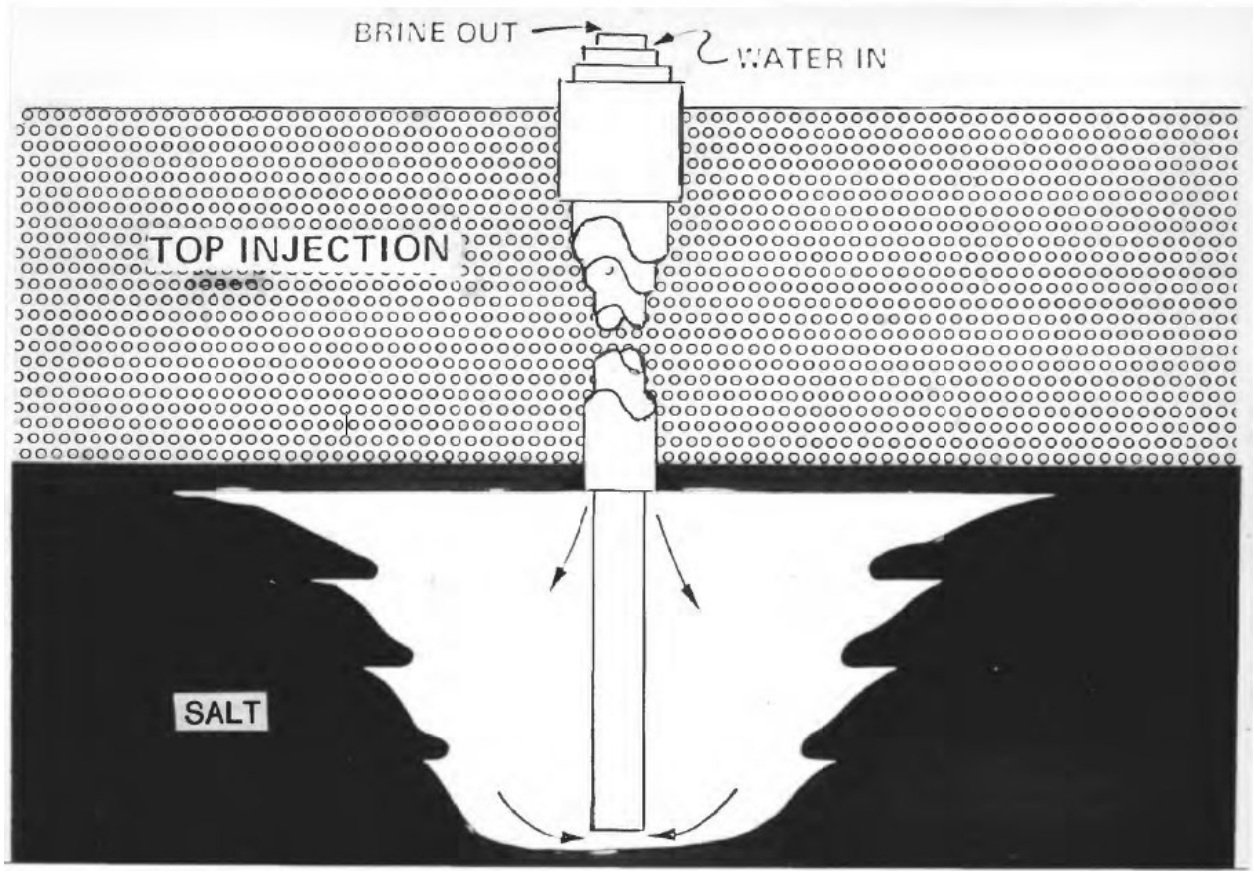

Figure 11: Single-well solution mining by top (annular) injection single well method. Fresh-water is pumped down at the top of the salt interval, and the brine is extracted from the base of the interval (modified (Ege, 1979) from Quiero, 1977).

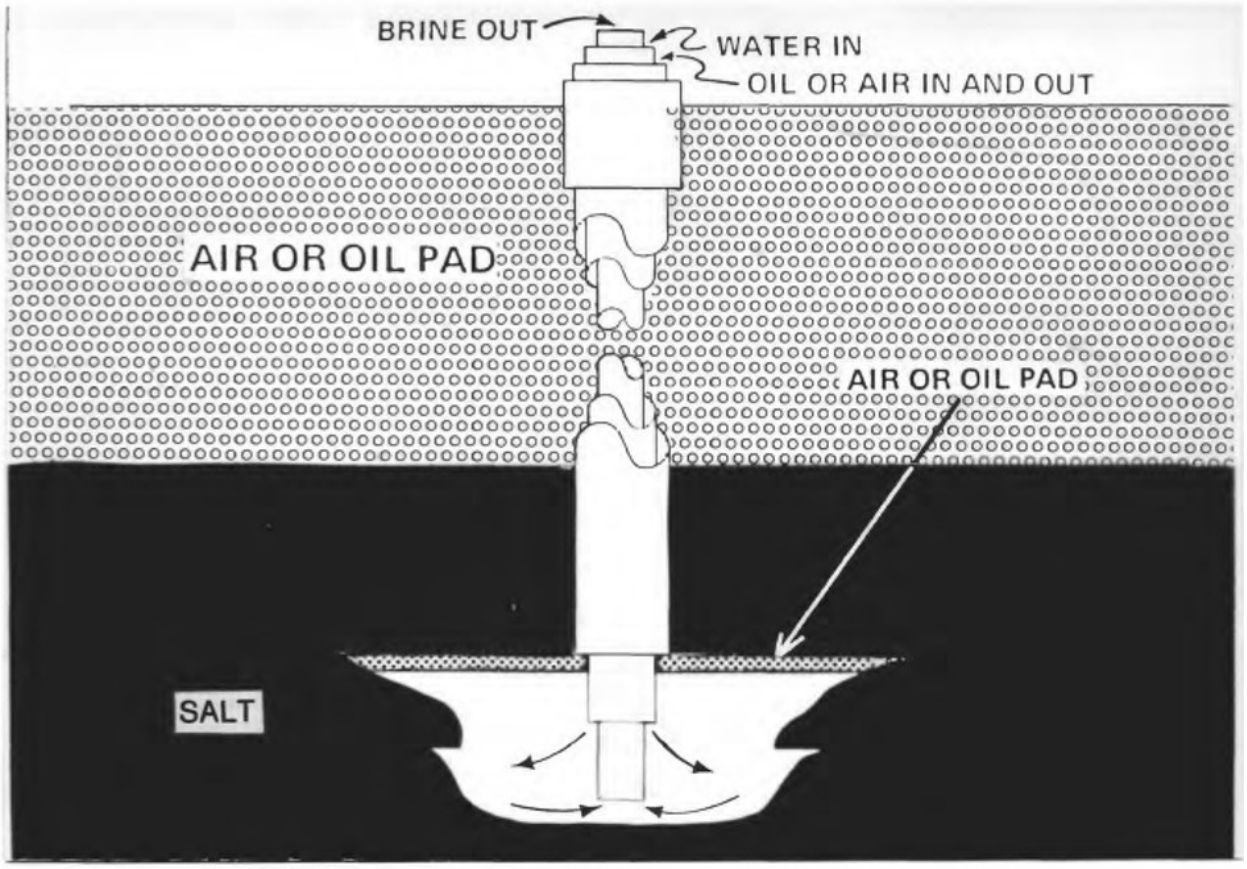

Figure 12: Solution mining by the air or hydrocarbon pad method. The lighter gas or oil pad floats on the heavier injected freshwater forming an impermeable barrier between the salt and the dissolving water (modified (Ege, 1979) from Quiero, 1977).

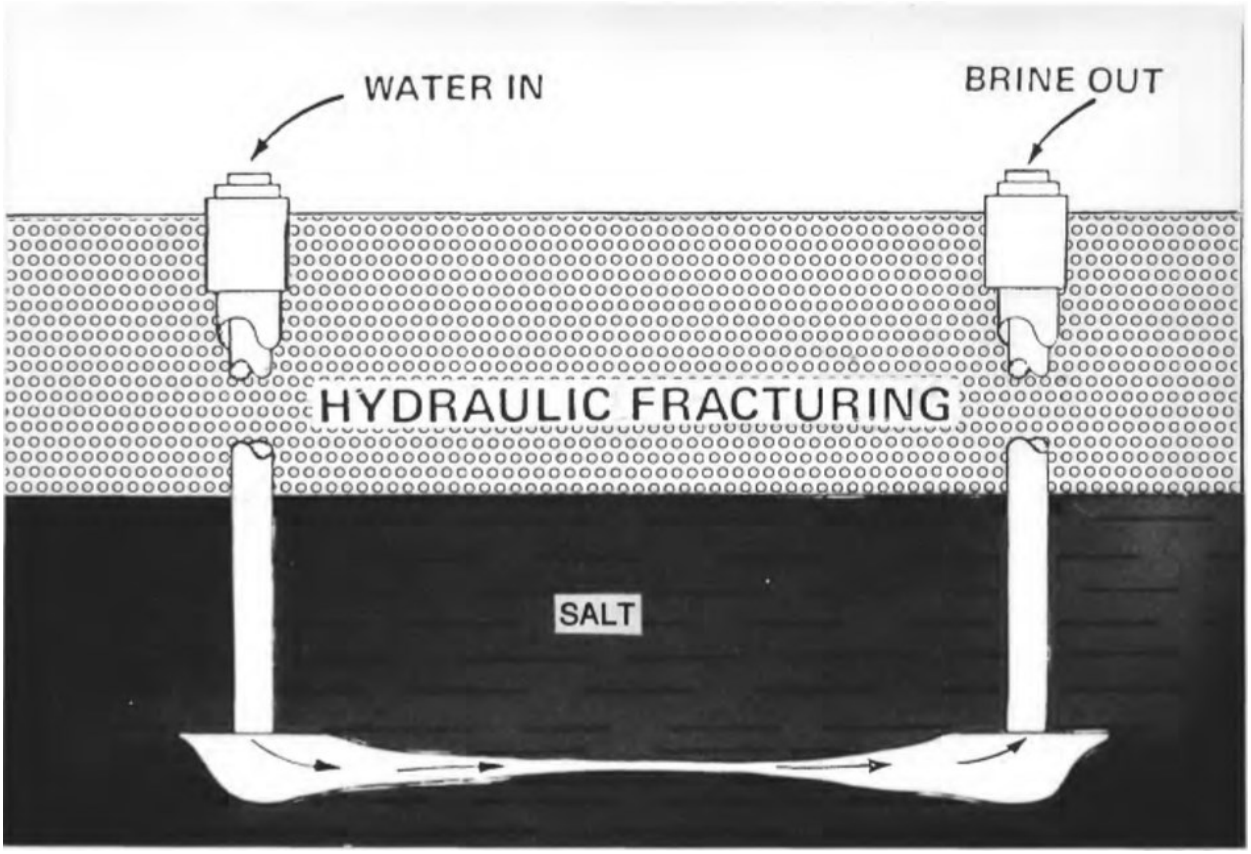

Figure 13: Multi-well, or hydrofracture method, between two brining wells. Hydrofracturing is used to coalesce a system of wells into a gallery by the application of pressured water at the desired depths (modified (Ege, 1979) from Quiero, 1977).

As mentioned before, the single-well method was the most popular used in Hutchinson during this time (Walters, 1978). During the single-well solution mining method, as the brine is being extracted the void is growing (Figure 14) (Quiero, 1979; Miller, 2007). When this void migrates vertically to an impermeable or bounding layer, it starts to expand laterally. This lateral expansion eventually reaches a point where the unsupported roof rock span exceeds a distance its strength can support. Once the roof span is too great, the bounding layer fails. This causes the dissolution zone to expand upward. This process can occur multiple times, likely depending on the number shale or anhydrite stringers to act as a bounding layer in the Hutchinson salt member at the specific well location.

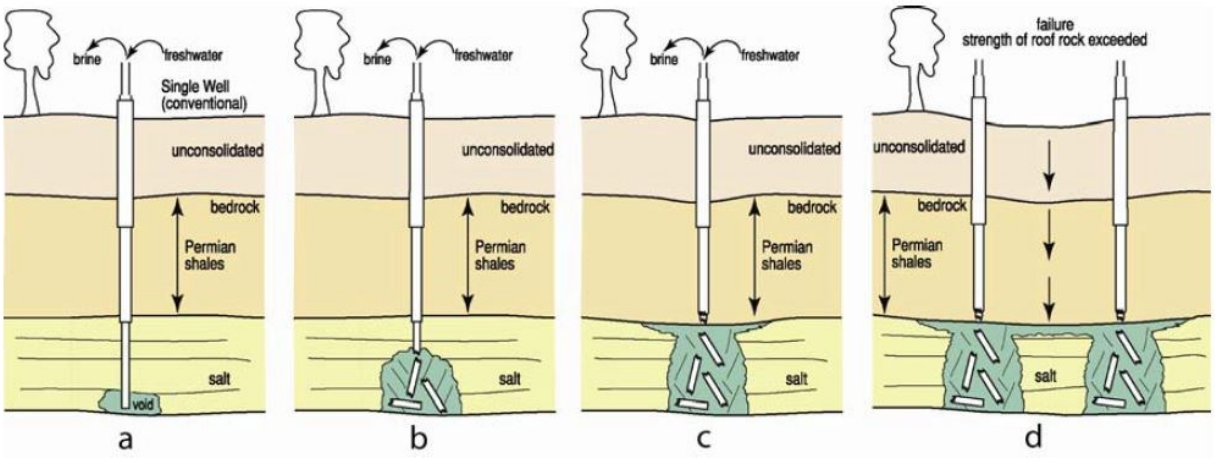

Figure 14: Historic progress of single-well solution mining from base of salt (a) through over-production (c) and the development of lateral expansion structure at the top of salt. (d) Represents the inadvertent formation of a gallery from the joining of multiple voids through horizontal expansion, connecting the two voids (modified from Miller, 2007).

As this incremental collapse within the Hutchinson salt member and overlying units continues to expand, eventually it can reach the 3-finger dolomite, which can act as a cap rock. This 3-finger dolomite has a higher Young's Modulus than the surrounding rock (Figure 15), meaning the dolomite is stiffer or resists the change of shape more than the surrounding shales (Joe Ratigan, personal communication, 2016; Watney et al., 2003). Once at the cap rock, the expansion process during the actual mining becomes primarily horizontal. The combination of two voids from adjacent wells forms a gallery between the two wells. These galleries can possess roof spans that are too wide to support the overburden load, causing collapse. This collapse of the roof rock causes the volume of the void to expand (Nelson, 1965), which was later coined "bulking" (Landes and Piper, 1972). This expansion of volume is dependent on the shape of the fragments that collapse (Barczak, 2006).

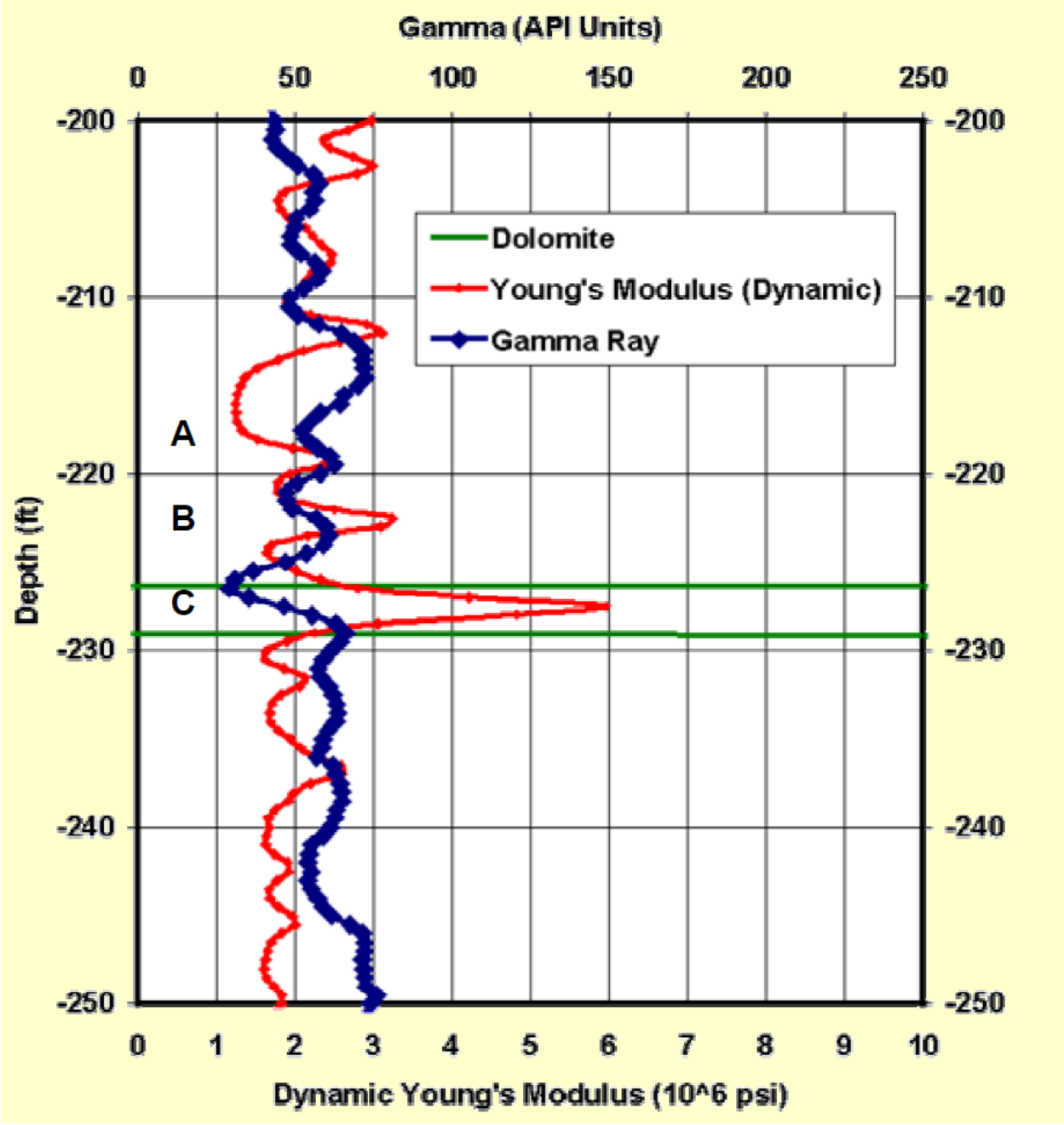

Figure 15: Dynamic Young's Modulus calculation for a well within Hutchinson, KS (Joe Ratigan, personal communication, 2016; Watney et al., 2003). This well is approximately 2 mile west-southwest of the study area, but the dolomite section highlighted is 3-finger equivalent. The dolomite has a significantly higher Young's Modulus, meaning the rock is stiffer than the surrounding rock.

The stress field expands as the roof span of a void increases creating a tensional dome (Figure 16) (Davies, 1951). Distortion within the tensional dome (a volume called the "compressional stress zone") acts as a compressional stress environment (Miller, 2007). Failure of this roof rock normally occurs under compressional stress, with failure centered at the location the stress is the greatest (Sofianos, 1996). How this deformation migrates to the ground surface is highly dependent on void geometry, physical condition and strength of roof rock, and the characteristics of the rocks that make up the overburden section (Miller, 2007).

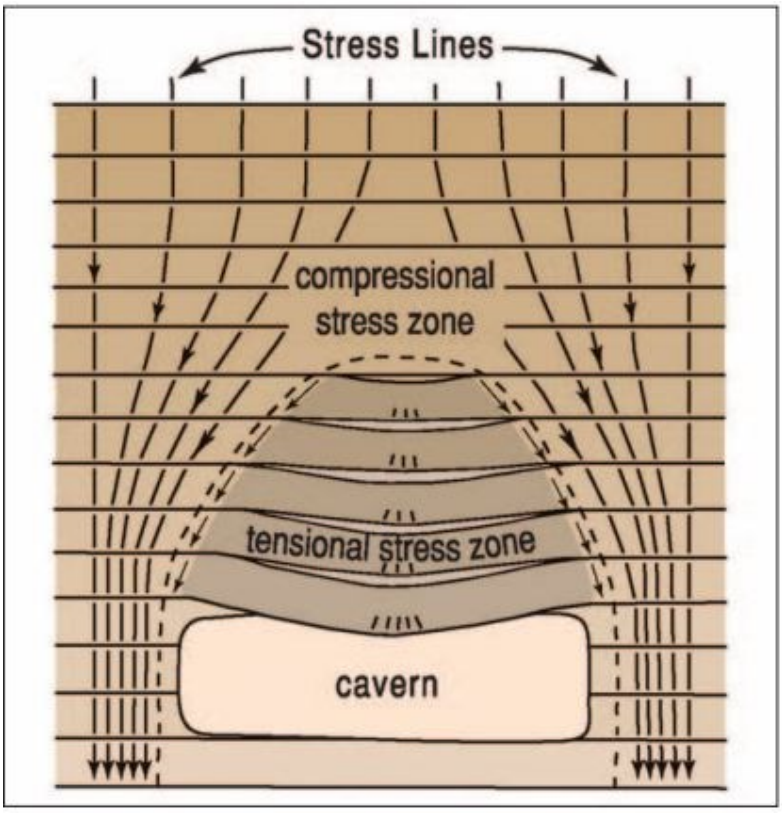

Figure 16: Tension dome and distribution of stress lines around a cavern opening in horizontal strata (modified (Miller, 2007) from Davies, 1951).

The shape and size of the void along with the lithology of the roof and pillar are important factors in determining the load bearing potential of a void's roof rock. The rock's strength under tension and flexure is generally negligible, while significantly higher under compression (Miller, 2007). This means a void containing flat roof rock geometry will not be as capable of supporting a larger diameter void, as a void with an arched roof. Failure of an arched roof under stress (load bearing) will occur when the load exceeds the strength of the arch system or redistribution of load (stress), due to enlargement of unsupported roof span, exceeds strength (Miller, 2007).

Depending on the characteristics of the overburden and volume of the void, failure can migrate at a rapid pace (catastrophically) or a series of smaller collapses (gradational) that migrates towards the ground surface much slower. During this gradational collapse, if only a portion of the overburden collapses, a new roof higher in the section with a reduced span will support the remaining overburden load (Miller, 2007).

Stress/Velocity Relationship

Changes in shear-wave velocity can be indicative of previous subsidence events or areas where void growth has elevated the stress field and increased the potential for roof collapse (Sloan et al., 2009). Because V_S is directly related to the shear modulus it is dependent on the rock matrix. Therefore, monitoring shear velocity should represent a highly sensitive method of detecting stress exceeding or dropping below native material which arises from nonlinear changes in strain relative to the stress (Sloan et al., 2010). V_S can be expressed as:

$$V_S = \sqrt{\frac{\mu}{\rho}}\,, \tag{1}$$

where μ is the shear modulus and ρ is the bulk density. Changes in the shear-wave velocity field for each specific rock are related to the differential stress and corresponding non-linearity in the stress-strain relationship (Dvorkin et al., 1996). Assuming bulk density remains constant, the shear-wave velocity is controlled by the shear modulus (Miller et al., 2009). Shear modulus (μ) is the change in shearing force per unit area (stress) divided by the change of length per unit length (strain):

$$\mu = \frac{\sigma}{\gamma} = \frac{\Delta F/A}{\Delta L/L}\,. \tag{2}$$

Measurements in a laboratory of p- and s-wave velocities show non-linear increase with confining stress (Eberhart-Phillips et al., 1989; Khaksar et al., 1999; Siggins, 2006). On the elastic deformation portion of the stress-strain curve, the shear-modulus is assumed to remain constant under static pressure (Sloan et al., 2010) (Figure 17). However, once the elastic limit is reached, the rock no longer behaves elastically, meaning the ratio between stress and strain is no longer linear. This makes it possible to detect plastic deformation during failure because of the increase in strain and decrease in stress.

Mechanical damage within the rock decreases the shear-wave velocity as a result of stress-induced plastic deformation (Winkler, 2005). A decrease in shear velocity could mean the rock has exceeded the elastic limit and requires less increase in stress to accomplish greater

strain than implied by the linear relationship during elastic deformation (Dvorkin et al., 1996). A localized increase in shear-wave velocity within the overburden overlying a void could be indicative of the increased load, creating a high shear-wave velocity "halo" (Sloan et al., 2009). An increase in V_S is due to an increase in the shear modulus or decrease in the bulk density. These high-velocity haloes suggest stresses have been transferred to areas surrounding void. Such anomalies could likely be key indicators of near-term roof failure (Sloan et al., 2009).

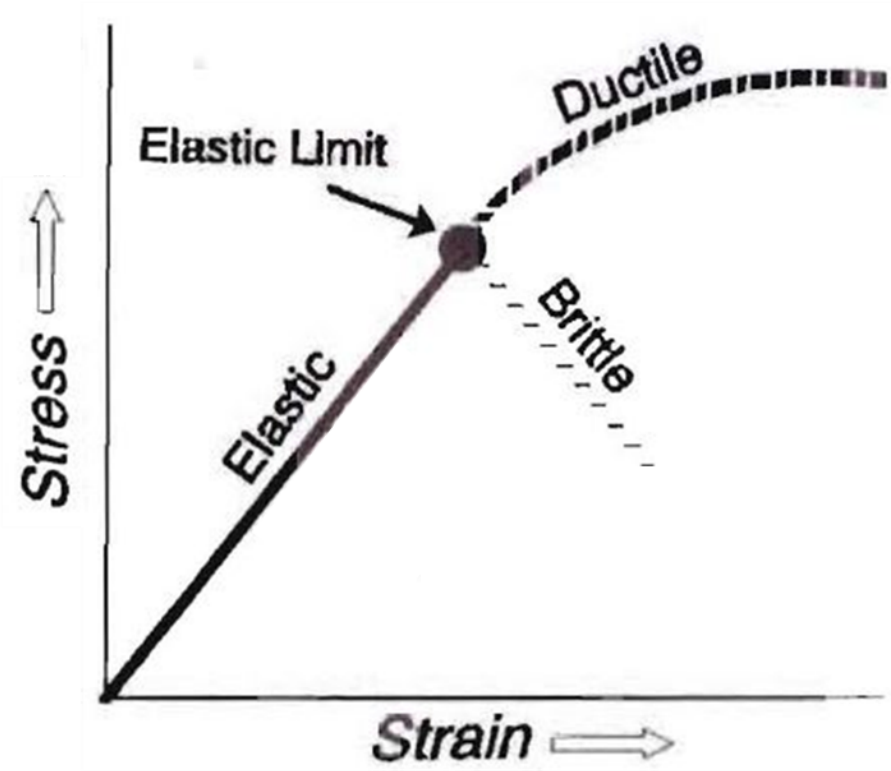

Figure 17: Generic stress/strain curve (modified from Little, 1999).

Challenges of Previous Work at Site

Extensive geophysical research has been conducted at the Hutchinson, Kansas, site including two P-wave seismic reflection surveys, two S-wave seismic reflection surveys, two

active MASW surveys, one 3D passive MASW survey, one passive MASW survey not included in this study, and the three passive MASW surveys included in this study. The first study was a P-wave seismic reflection survey in 1993 (Miller et al., 1993). This survey, primarily a feasibility study, successfully delineated the subsurface extent of roof failure associated with the dissolution mining of a 120-m (400-ft) deep and 60-m (200-ft) thick salt bed (Miller et al., 1993). With the findings of the first P-wave survey, future surveys aimed to extend the methodology and extract even more information from the subsurface.

A second P-wave seismic reflection survey was acquired at the site to investigate the shallow subsurface between a sinkhole that formed catastrophically within a few tens of meters of a main east/west rail line (Miller et al., 2005). These data were acquired in a rapid response following the collapse under extreme site access restrictions due to the location of the subsidence and rate of sinkhole growth. The overall data quality for this survey was below expectations and not equivalent to other seismic data from this area where acquisition parameters, equipment, and target intervals were similar (Miller et al., 2005).

The previous two P-wave surveys effectively delineated collapse structures at this site after sinkhole formation (Miller et al., 2009). However, if the void has not vertically migrated completely through the Ninnescah Shale, P-wave reflection surveys would not independently provide sufficient information about material properties to confidently predict the location and intensity of the tensional dome within the remaining shale overburden (Miller et al., 2009). Therefore, the new scope of work switched to acquire seismic information that would allow

predictions as to an individual void's relative potential (in comparison to all voids in the field) to migrate to the bedrock surface (Miller et al., 2009).

Downhole shear-wave vertical seismic profile (VSP), S-wave seismic reflection survey, and an active MASW survey were acquired in 2009 at the site to rank known salt mines by the highest risk of collapse based on elevated shear-wave velocities that represent elevated stress. Reflection data from the 2009 study are the first to provide empirical evidence that the changes in stress related to the tensional dome concept (Davies, 1951) can be non-invasively measured for underground caverns using shear-wave seismic reflection (Miller et al., 2009). However, for shear-wave seismic reflection to be a viable method to characterize the degree of change in stress associated with a single cavern at this site, resolution must be improved and the velocity-discrimination techniques must be developed that can isolate changes in shear-velocity at sub-spread distances (Miller et al., 2009).

MASW data from the 2009 survey showed consistent velocities and velocity structures with seismic reflection interpretations within the unconsolidated portion of the subsurface (Miller et al., 2009). However, the surface-waves did not possess long enough wavelengths to sample the depth necessary to interrogate the status of the void without aid from another method (Miller et al., 2009). The active MASW data acquired recorded surface-wave seismic energy down to approximately 7 Hz allowing for a sampling depth of approximately 20 meters, while the desired minimum depth of investigation is approximately 70 meters (Miller et al., 2009).

Following the 2009 acquisition in Hutchinson, the next study consisted of both remote passive and roadside passive MASW (Ivanov et al., 2011; Leitner, 2011; Leitner, 2015). This combination of remote and roadside passive MASW, similar to the 2009 study, aimed to estimate and rank the relative apparent stress based on the shear-wave velocity in the roof rock of the voids, or jugs, along the northern boundary of the investigation site (Ivanov et al., 2011; Leitner, 2011; Leitner, 2015). Passive surface-wave energy was recorded using a combination of multiple 1D survey lines in different arrangements to create 2D arrays in the field. A total of four grids were acquired, along with a long 1D survey line parallel with the East-West oriented train tracks. One grid of 336 geophones, oriented in a crisscross pattern (Figure 18) was centered about a well with known vertical void migration (Leitner, 2015). One grid with the exact same acquisition parameters (number of geophones, receiver spacings, record length, array orientation, etc.) was centered about a well known to have a salt roof and no vertical migration. One grid consisted of three intersecting 1D survey lines with 24 geophones each. Due to the limitations in acquisition, the small grid of crossing 1D survey lines did not produce results of any significance. A grid of 275 geophones, oriented in a 2D spread (Figure 18) was also set up over recently destroyed houses; however, the underground foundation, pipes, and surface conditions negatively impacted the recorded surface-wave energy (Leitner, 2015).

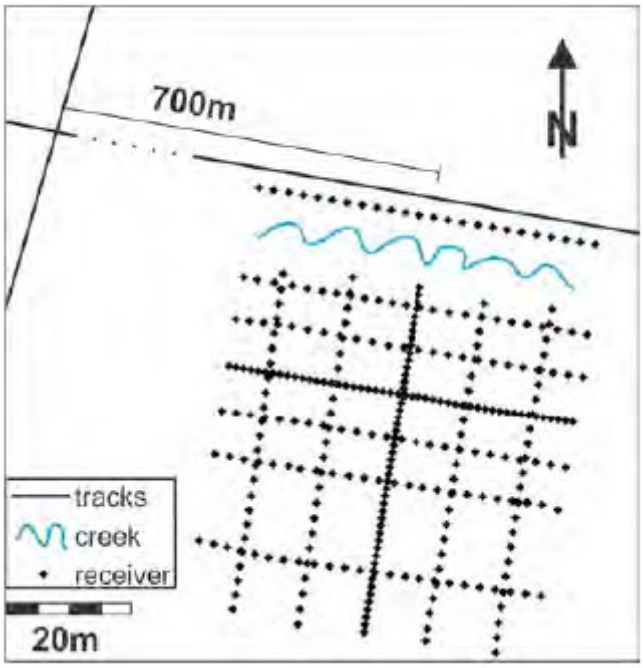

Figure 18: Passive MASW acquisition utilizing crisscrossed 1D linear arrays connected (acquired simultaneously) to create a 2D array (Leitner, 2015).

Data processing was aided by a novel automated computer technique that determines the incidence angle of the seismic energy and then selects receivers within the 2D grid that are in-line with the source to create several pseudo survey lines (Ivanov et al., 2011; Leitner et al., 2011). Each of these lines are then processed, creating overtone images for each line individually. The extracted dispersion curves for each pseudo line, provided there exists a source with sufficient energy, are then inverted to generate a 1D velocity function. Because the 1D velocity function is assigned to the midstation of the line, combining all in-line pseudo lines produces midstations scattered throughout the 2D grid. Utilizing multiple sources from different incidence angles and variable receivers within the 2D grid provides a variety of

midstation locations. These 1D velocity functions can then be interpolated both horizontally and vertically, essentially creating a 3D volume of shear-wave velocity (Leitner, 2015).

METHODS

Approach

To advance the use of shear-wave velocity gradients as a method for determining the fitness of abandoned dissolution mine voids, a program was developed using a combination of roadside passive MASW and remote passive MASW survey techniques. The roadside passive MASW survey lines were utilized to determine the vertical shear-wave velocity profiles. The remote passive MASW survey grid was acquired to ensure high-quality and accurate results by providing azimuthal direction of seismic energy (Leitner, 2011; Leitner, 2015). The combination of the two allowed for adjustments to ensure accurate velocities in the 1D survey lines. The data were acquired over three separate surveys requiring one night recording each due to equipment availability and software capabilities. Data were acquired throughout the night when the cultural noise was significantly lower, allowing for our target surface-wave source (the nearby passing trains), to have a higher signal-to-noise ratio. With cultural noise minimized, the dominant surface-wave energy recorded should be produced from the nearby trains.

Acquisition

Eight 1D survey lines were acquired at the site location with several target voids throughout the area (Figure 19). Each survey line was strategically oriented to be in-line with the two main sets of railroad tracks. While orientation and target void might be different, these survey lines have very similar acquisition parameters (Table 1). All data were acquired with 4.5-Hz vertical-component geophones spaced 3 meters apart. Seismic lines oriented near north-

south or east-west best match source orientations. Data were acquired along each line throughout the night with a 400+ channel 24-bit Geometrics Geode distributed seismic system. Each record saved a total of 30 seconds of data. The frequency of the recorded surface-wave energy must remain below the Nyquist frequency in order to avoid aliasing. A sample interval of 2 milliseconds produces a Nyquist frequency of 250 Hz, which is sufficient for this study.

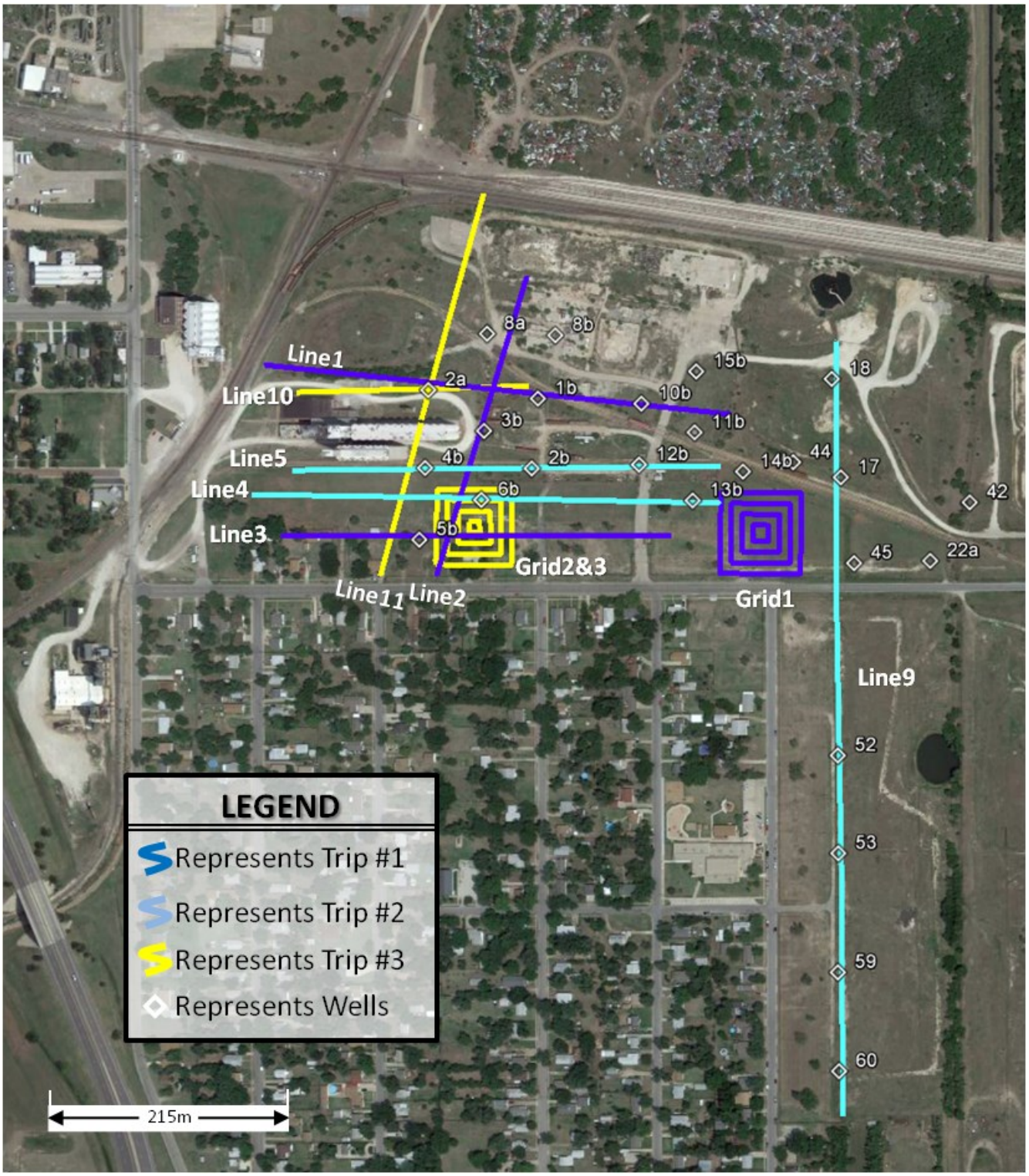

Figure 19: Acquisition layout utilized at the Hutchinson, Kansas, site in relation to the intersection of two nearby railways.

	Line1	Line2	Line3	Line4	Line5	Line9	Line10	Line11
# of Receivers	144	96	126	144	144	240	72	115
Station Spacing (m)	3	3	3	3	3	3	3	3
Total length (m)	429	285	375	429	429	720	213	342

Table 1: Number of receivers, station spacing, and total length of the 1D survey lines included in this study.

When looking at the raw data, clear coherent signal can be observed when a passing train was producing recordable energy (Figure 20). Without an identified train, the data look very noisy with no coherent signal throughout the record (Figure 21).

A 2D grid of geophones was deployed and data acquired simultaneously with the 1D lines as a tool to determine the orientation of the seismic energy (Leitner, 2011; Leitner, 2015). Data from the 2D grid can be gathered and analyzed to establish amplitude, frequency, and azimuthal direction relative to north, assisting in the selection of a single source event. Grids oriented with a dominant one-dimensional component, such as an elongated oval or a rectangle, have proven to possess geometry-induced velocity errors and can lack desired low frequencies (Leitner, 2015). A square geometry for the 2D grid was chosen to eliminate potential bias of a single orientation by providing the opportunity to record phase velocities propagating in all orientations (Leitner, 2015). For each trip, the grids were deployed with the same orientation, same number of geophones, and the same acquisition parameters but were moved slightly to facilitate data acquisition of each specific trip. The grids contained 128 geophones with a 5 meter in-line spacing and configured to form four concentric expanding squares with 15, 35, 55, and 75 meter sides. Seismic records, like the 1D survey lines, were 30 seconds long with a 2 millisecond sampling interval. Other than simple quality control, due to the nonlinearity of the survey grid, analysis on the raw seismic record is very limited (Figure 22).

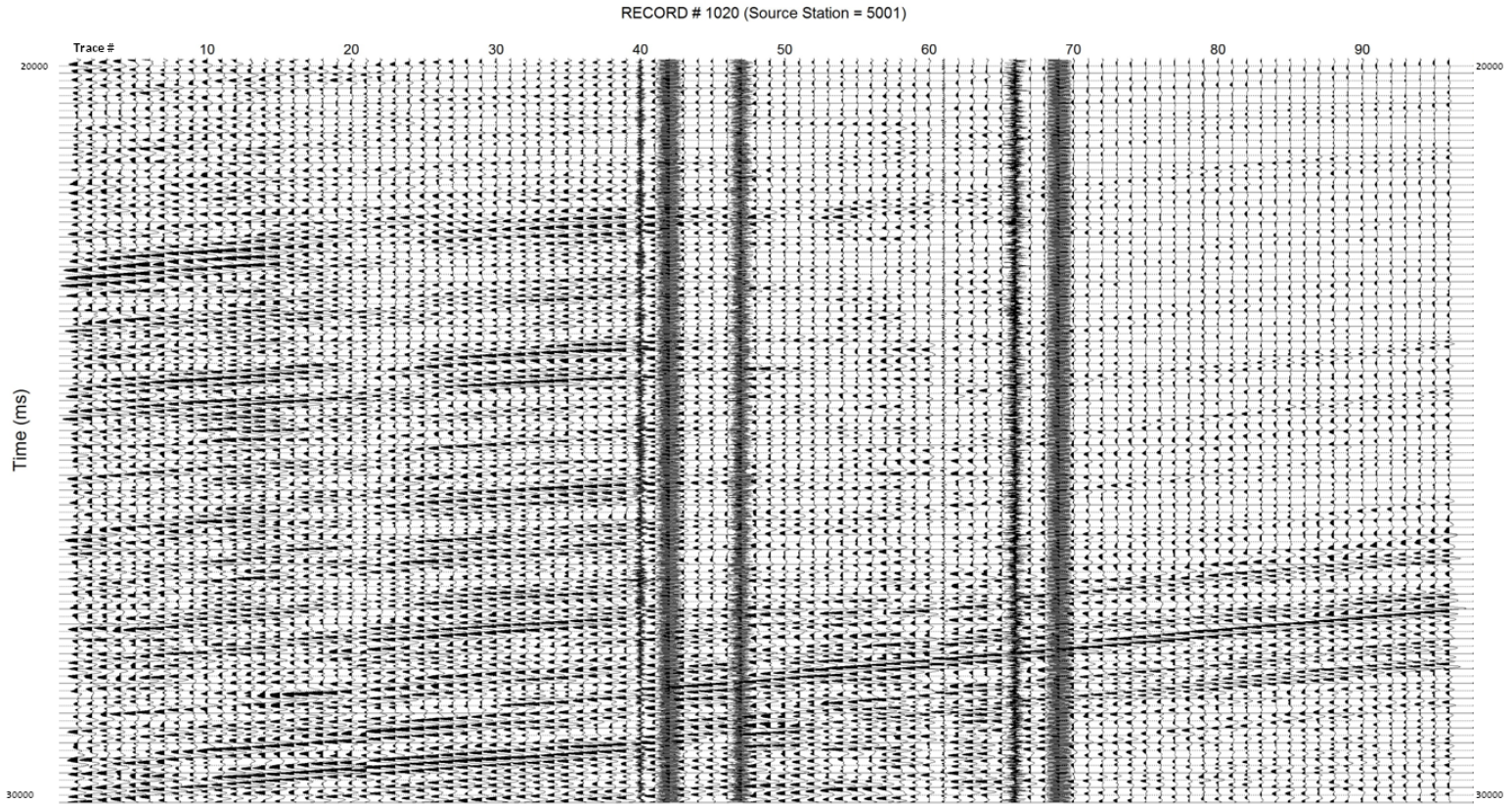

Figure 20: Raw seismic record for a 1D survey line recording surface-wave energy from a train event.

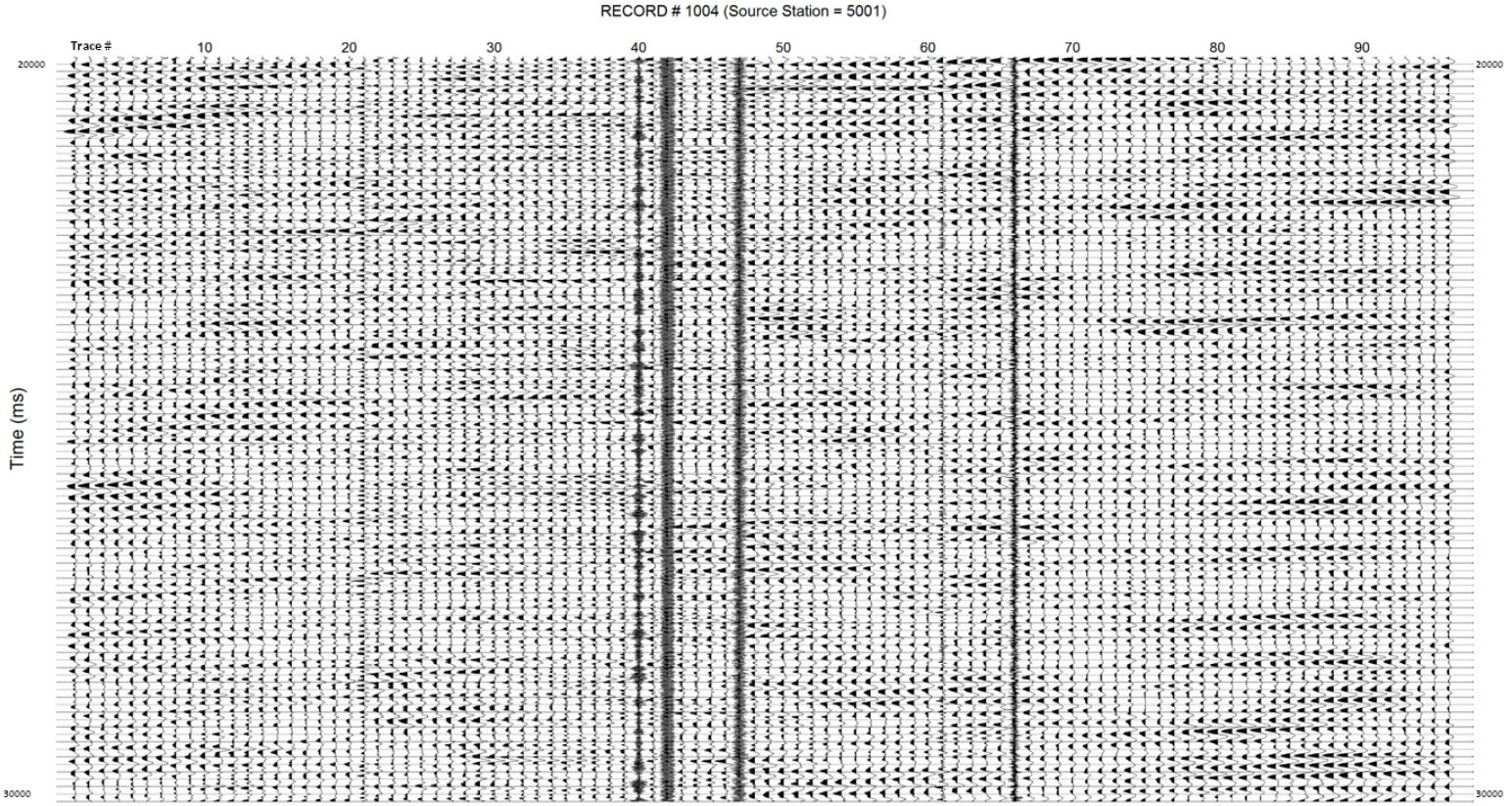

Figure 21: Raw seismic record for a 1D survey line with no evident train event.

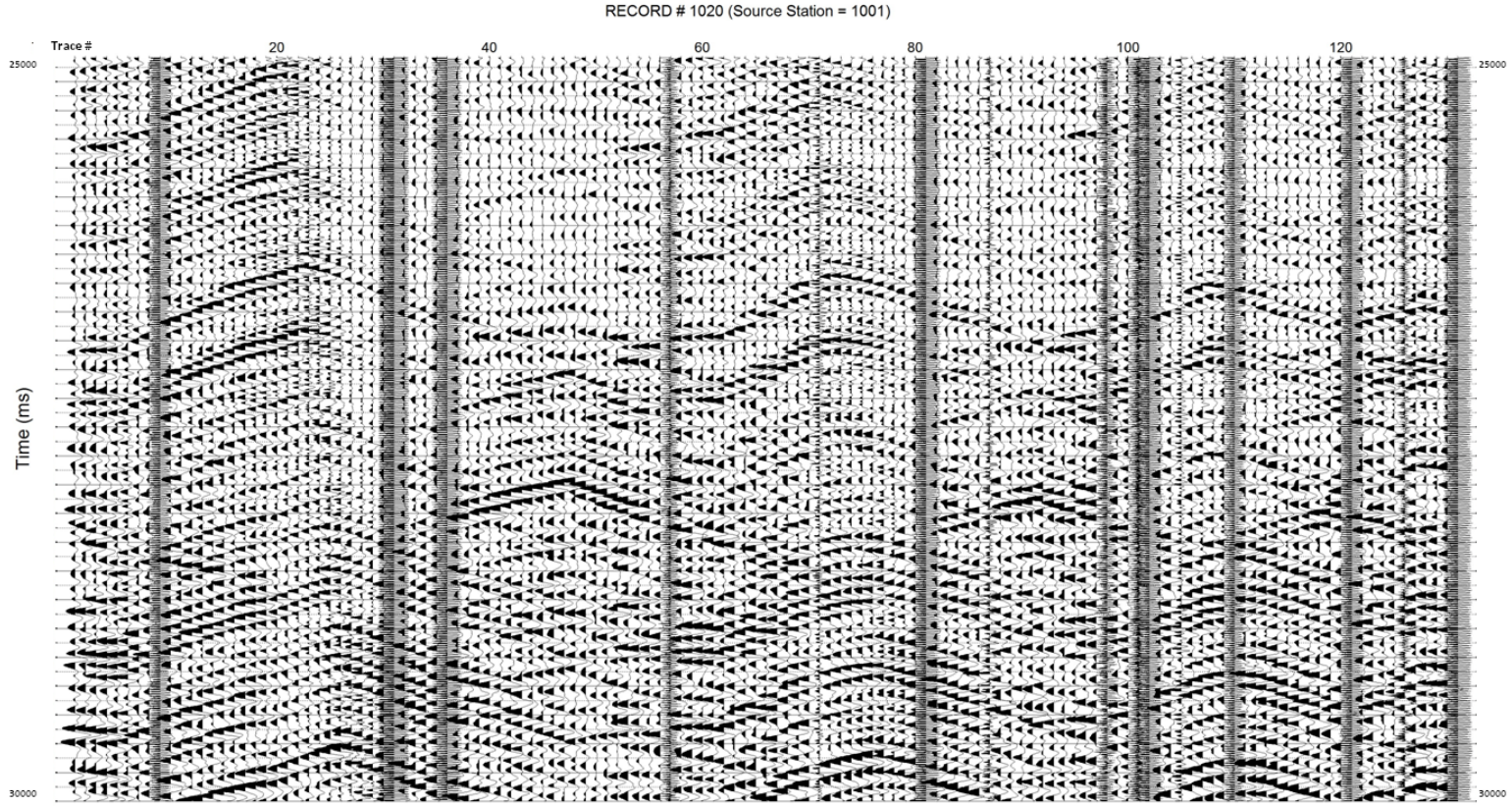

Figure 22: Raw seismic record for a 2D grid recording surface-wave energy from a train event.

Processing Workflow

Proprietary software developed at the Kansas Geological Survey, including SurfSeis and SeisUtilities, was utilized to process all data. The workflow for passive MASW processing can be very basic, or can be quite complex (Figure 23). The first step after data acquisition is sorting the data into its lines and grids. Once the data has been sorted correctly, it is ready for pre-processing. This pre-processing includes conversion from raw field data SEG-2 format to KGS processing format. Once the data has been converted, geometry is assigned based on the field notes. The assignment of geometry is critical for correct spatial designation and to calculate velocities and populate the 1D velocity field.

Approximately 1000 records were recorded for each line. However, the majority of these records did not capture the desired surface-wave energy generated by the nearby passing trains since there were approximately 20 recorded trains passing each night with each train providing about 20 seconds of useful data. However, all of these records are included in the early stages of processing in case a passing train was not properly logged in the field notes. The next step is to determine a sufficient source record based off the quality of the generated overtone images. The overtone images for each 1D survey line and the 2D grids are generated independently.

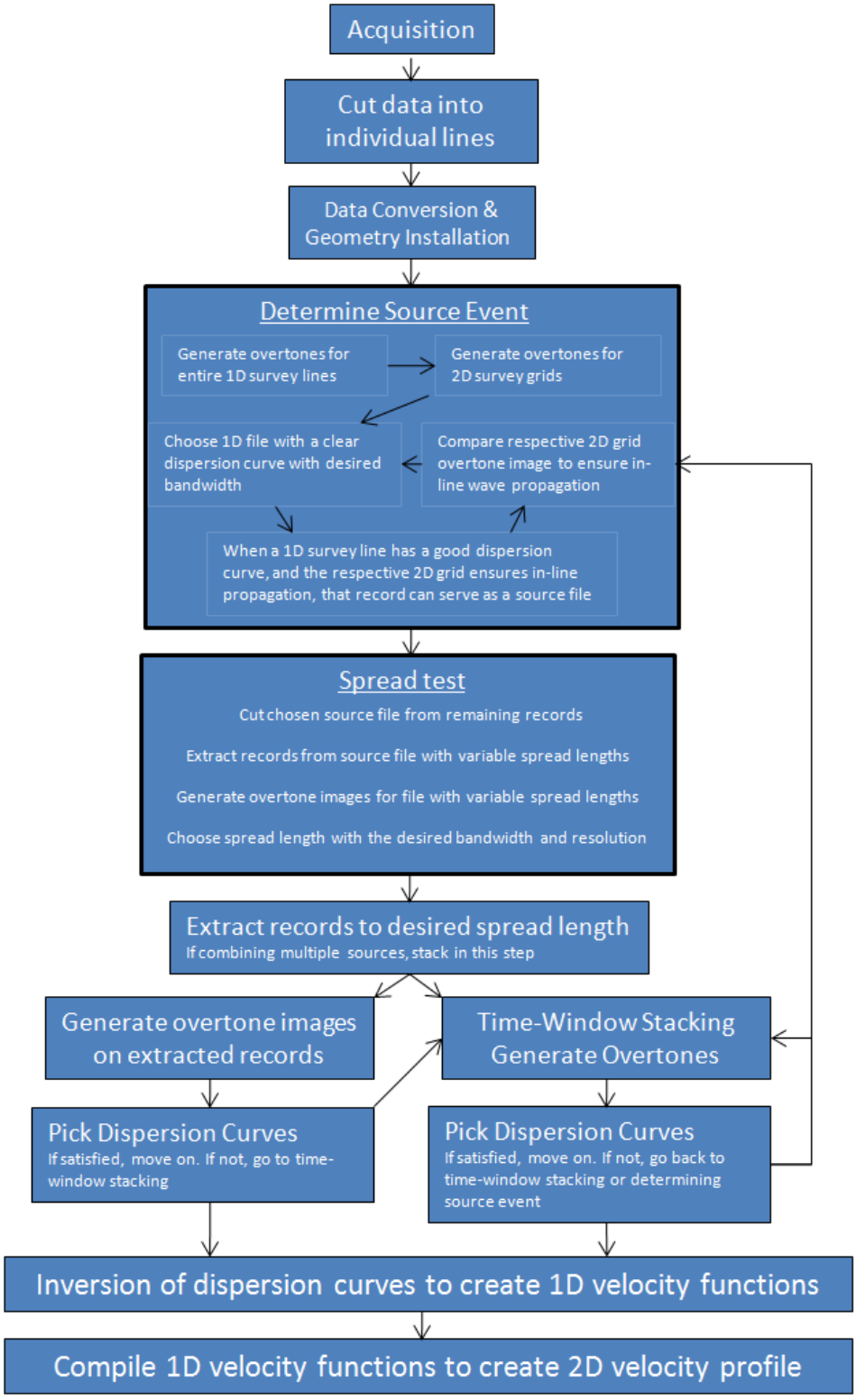

Figure 23: Passive MASW processing workflow utilized in this study.

Generally, the data gathered from 1D survey lines will be analyzed first because files with little-to-no recorded train seismic energy can quickly be eliminated as a potential source record. Any file that when transformed into phase velocity vs. frequency space (overtone image) results in a continuous, coherent, broad-bandwidth, and high-resolution dispersion curve, meets the basic requirements. Once all of the dispersion curves for a given 1D survey line have been analyzed, data from the 2D grids are then analyzed. Because data from the 1D survey line and 2D grid were acquired simultaneously, it is easy to identify files that recorded the same passing train event. A plot with the frequency on the x-axis and azimuth (0°-360°) on the y-axis is an amplitude spectra relative to azimuth (Figure 24). This allows the dominant direction of the wave propagation to be determined. These azimuth plots are produced by scanning the raw seismic file with a varying orientation of a designated interval, then stacking all traces along that orientation. The data are then filtered according to frequency creating a 2D plot representing the amplitude of each frequency for each orientation (0°-360°).

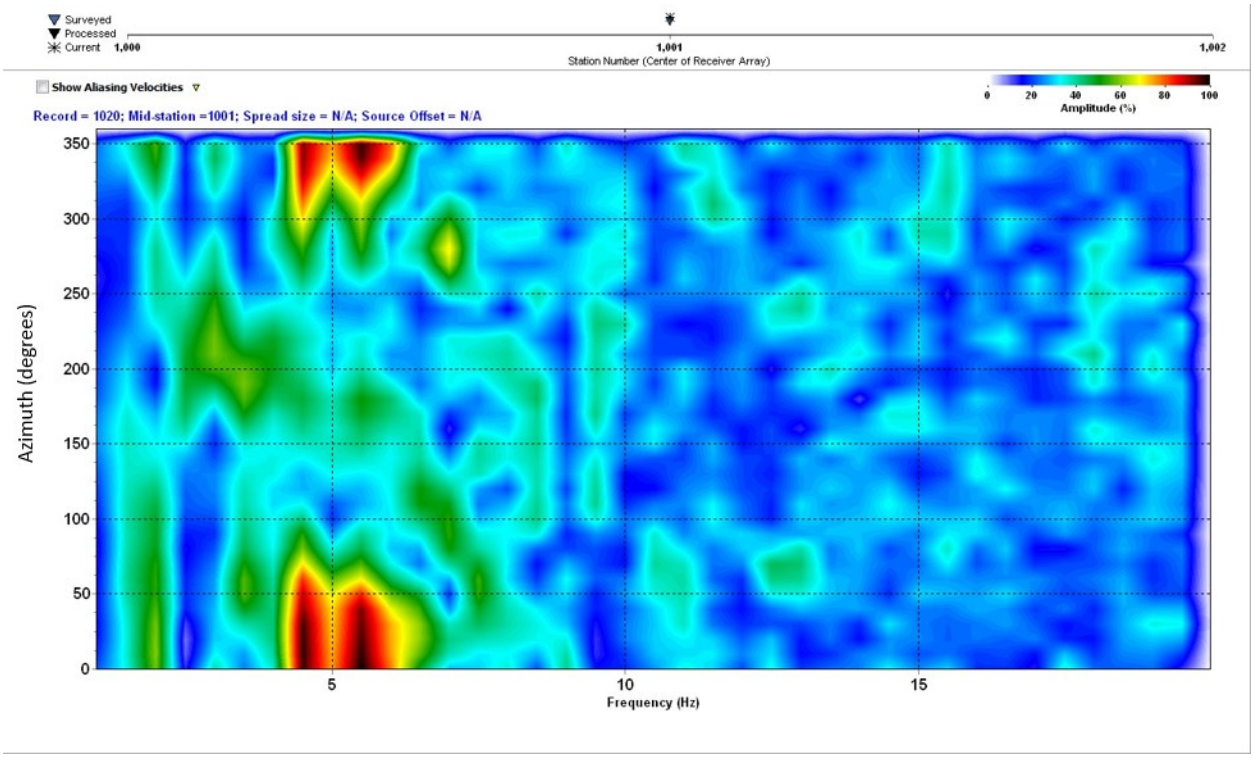

Figure 24: Example azimuthal overtone image plotting frequency vs. degrees. In this example the dominant frequencies are centered about 0°.

The selection of gathers with in-line wave propagation is vital to selecting the proper gathers that will ensure the overall accuracy of the final velocity profile. A record with dominant energy propagation no more than 30° away from the orientation of the survey line is required to maintain as close to in-line wave propagation as possible and avoid significant contamination of elevated velocity errors. Oblique angle source energy relative to the orientation of the survey line can result in an elevated apparent velocity (Park and Miller, 2008). A simple calculation can be used to determine the effect on velocity of energy propagating oblique to the survey line. This change in velocity can be expressed as a percentage by:

$$\Delta v = [1 - \cos(\theta_1 - \theta_2)] * 100, \quad (3)$$

where Δv is the change in velocity, θ_1 is the orientation of the wave propagation (in degrees counterclockwise from east), and θ_2 is the line orientation (in degrees counterclockwise from east). Table 2 represents the approximate velocity errors, calculated by Equation 3, due to slight oblique angles between source orientation and line orientation. A $\Delta\theta$ of 30° or less will inherent a velocity error within the 15% uncertainty of the passive MASW method (Xia et al., 2000). Staying within this $\Delta\theta$ of 30° is important because the velocity cannot be adjusted outside of that window. Outside of 30°, the wave has propagated through a different medium, therefore sampling a different midpoint. If the azimuth plot shows significant scattered energy, incoherent orientation, or high-amplitude (actual values are relative to surrounding azimuth values and frequencies) energy in a completely different orientation (>30° between receiver line and energy propagation), that record is then disregarded (Figure 25). Once an azimuth plot contains coherent, broadband signal that is characterized as in-line (or within the 30° window) energy propagation, it can then be classified as a 'source record.' Multiple records can serve as source records, but initially just one record should be processed.

Line	Source Orientation	Line Orientation	$\Delta\theta$	Δv
1	10°	-5°	-15°	4%
2	225°	255°	30°	15%
3	10°	-5°	15°	5%
4	0°	358°	2°	<1%
5	355°	1°	6°	<1%
9	88°	91°	6°	<1%
10	350°	1°	11°	2%
11	237°	254°	17°	4.5%

Table 2: Direction of the passive sources and the 1D survey lines (in degrees counterclockwise from east), the angle of the source with respect to the line ($\boldsymbol{\Delta\theta}$), and the percent change in apparent velocity caused by the oblique source orientation ($\boldsymbol{\Delta v}$). These values will later be used to eliminate the oblique apparent velocity error.

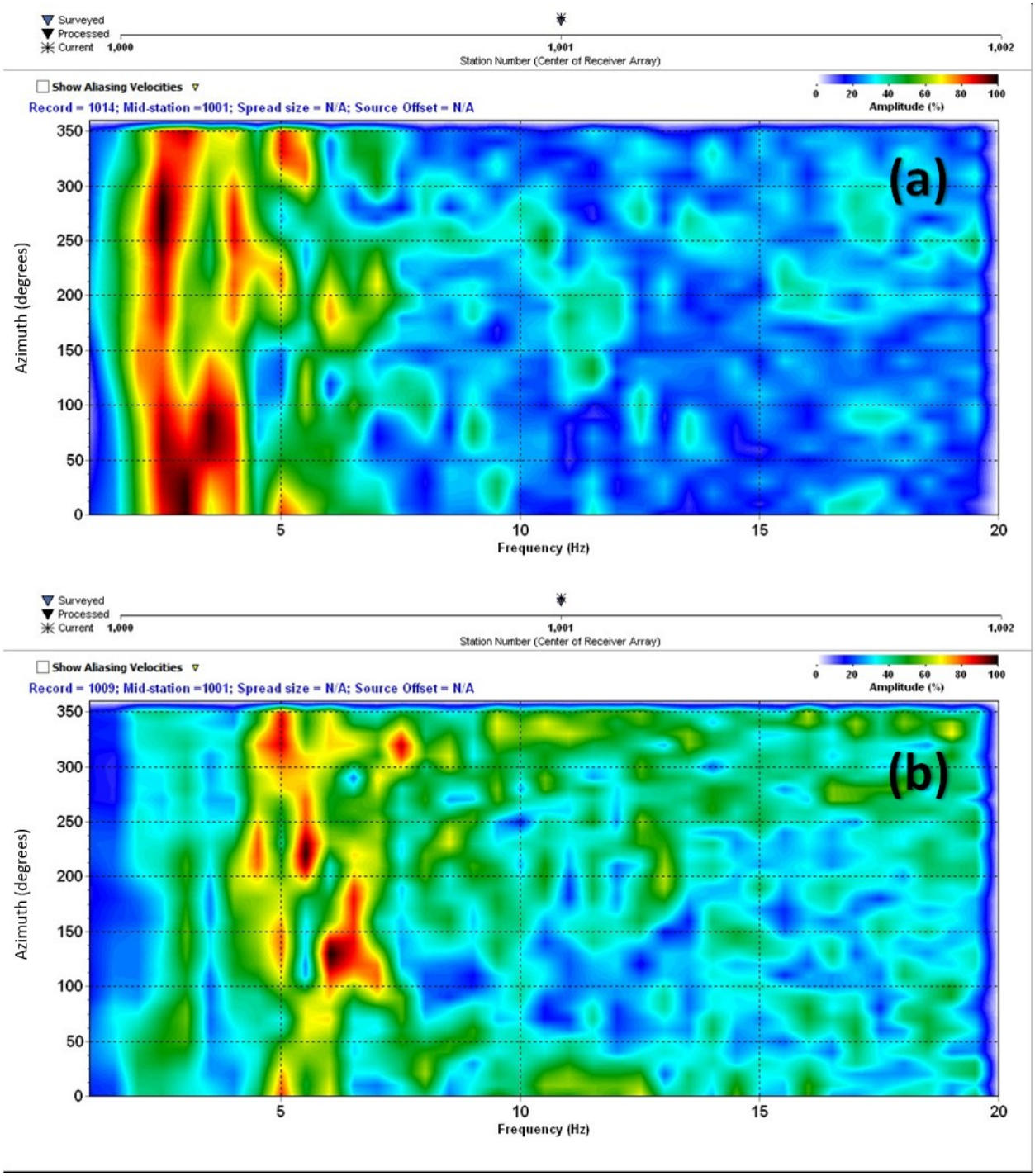

Figure 25: Bad azimuth overtones from the 2D grid that were disregarded because the energy was full azimuthal (a) and lack of any coherent signal in the desired frequency range (b).

Once a source record has been chosen, a spread test must be performed to determine the optimal spread size for this combination of source and site velocity structure. Within this spread test, the desired source record is extracted from the other records to keep the file sizes manageable. Once the record is extracted, individual gathers are extracted from the entire record with variable sized sub-spreads. A common method is to start with a predetermined spread size in the center of the record, and add receivers to the end of each line at a set interval (Figure 26).This will ensure the same midpoint is being sampled from one gather to the next once the gather has been transformed into an overtone image.

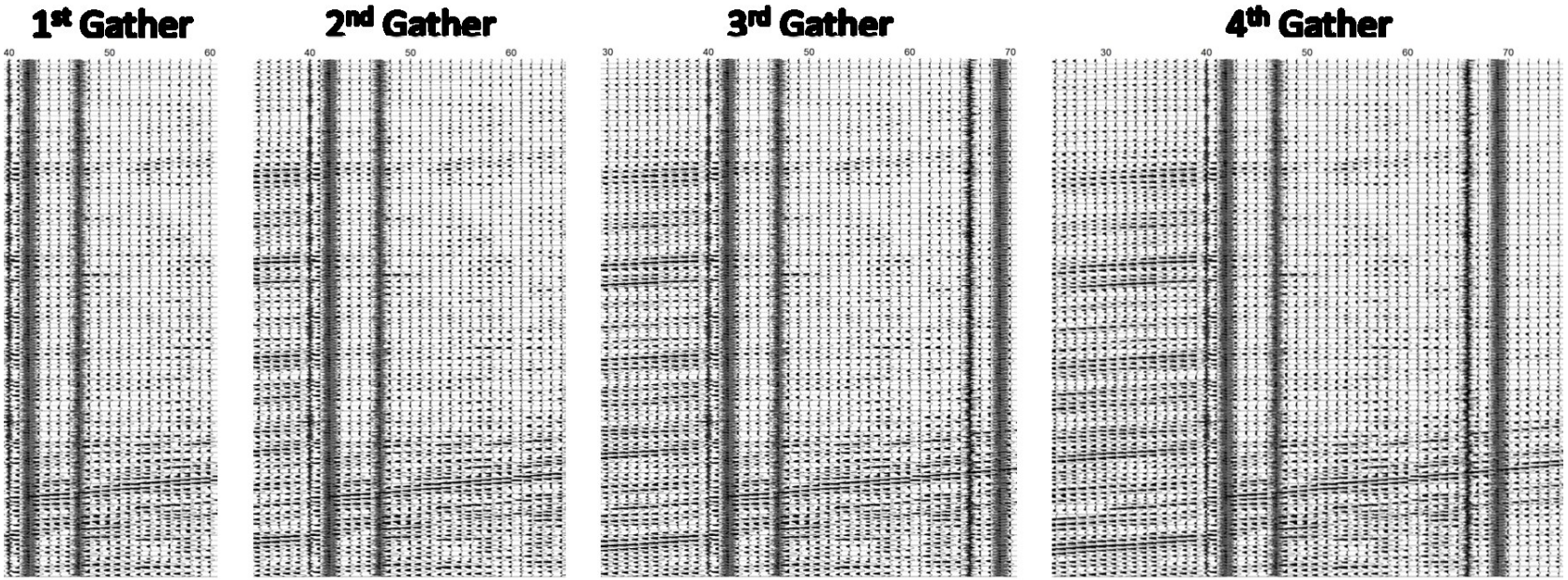

Figure 26: Gathers extracted from the chosen record with varying sub-spread sizes. Each gather in this example adds 10 receivers, 5 on each side.

The number of total sub-spread sizes is dependent on the total number of receivers active in the initial deployment of the survey line. These sub-gathers are then transformed, producing the overtone images. The overtone images are analyzed and qualitatively compared relative to each other to determine the optimal spread size based on frequency range, coherency of signal, and signal-to-noise ratio. After an optimum spread size is chosen, the initial record (pre-spread-test) is decimated into several gathers each containing this optimum spread length (Figure 27).

Overtone images are then transformed from the gathers containing the optimum spread lengths. Combination of multiple sources is done post-transformation to ensure desired surface-wave signal is not destructively stacked from the record. These stacked overtone images must have the same mid-stations, so it is more accurate if gathers with the same receiver spread lengths are stacked.

The next step in the generic processing procedure would be to generate overtone images and pick appropriate dispersion curves for the extracted gathers. Resolution of these overtone images are dependent on the transformation technique, the acquisition layout, and the processing parameters utilized (Park et al., 1998; Rix and Leipski, 1991). Acquisition parameters affecting resolution include sample interval, record length, geophone spacing, survey length, frequency of the geophones used, coupling of receivers, and source utilized. A general rule of thumb is the receiver spread size is approximately the maximum depth of investigation.

Overtone images are generated for a group of receivers and produce an image representative of a single midstation. The dispersion curve extracted from the overtone image can be inverted into a vertical 1D velocity profile that represents a lateral average of the velocity associated with the receiver spread chosen. Therefore, utilizing smaller receiver spreads will average less surface area, increasing horizontal resolution in the final velocity profile. However, generally the longer receiver spread lengths generate a more pronounced and coherent fundamental mode dispersion curve trend on the overtone image (Dal Moro et al., 2003; Ivanov et al., 2008; Xu et al., 2006).

If the dispersion curve is still not clear or not coherent, enhanced processing techniques can be utilized. Time-window stacking (Ivanov et al., 2013; Leitner, 2015) extracts small windows of time within each record, generates an overtone image for that time window, then scrolls down a specified time increment and repeats the process for the next time window (Figure 28). An option to “keep” (retain) every overtone image (100% keep), or eliminate overtones with lower signal to noise based on percentage is available within the software. This is known as percent keep in this study. For instance, a 90% keep eliminates the 10% of the records with the lowest signal-to-noise ratio. This percent keep option can significantly change the signature of the overtone images, so by default all records are kept. The optimal percent keep parameters are likely different for each site based on velocity structure.

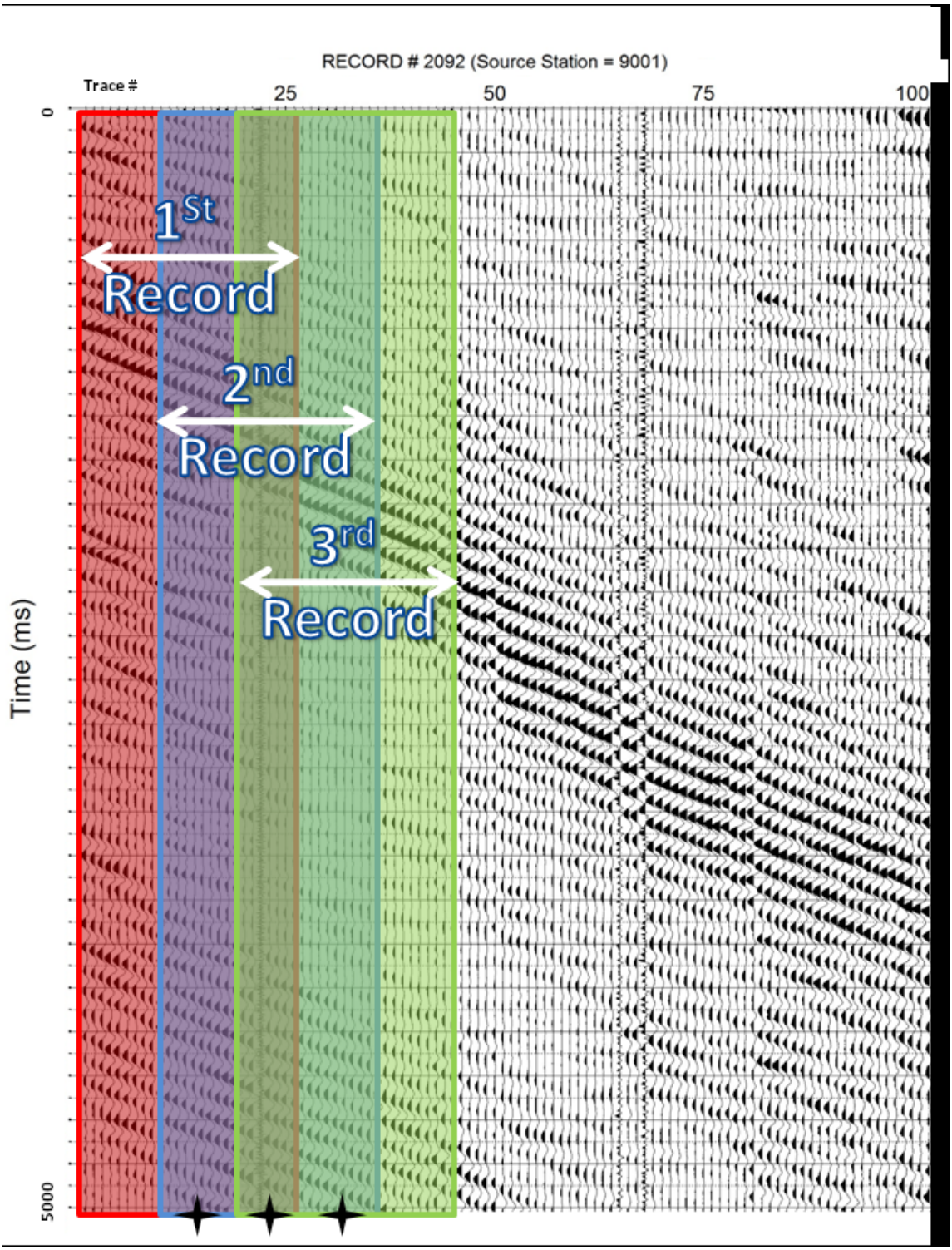

Figure 27: Once the optimum spread size has been chosen, records from the source file can be extracted to generate many gathers within the source file. Each record is denoted by a different color and the black star at the bottom represents the midstation associated with each record. The location and frequency of these stars determine the limits and spatial sampling of the final velocity profile.

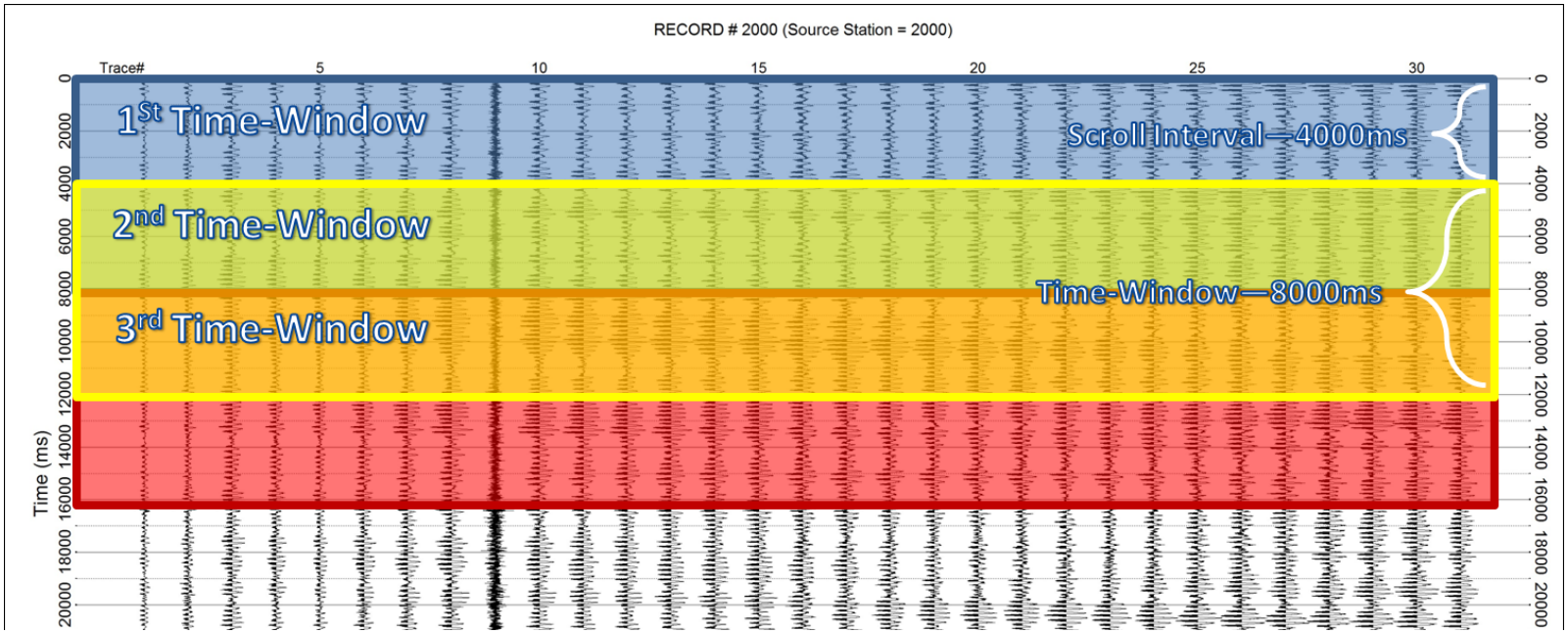

Figure 28: If the time-window stacking option is chosen, specific parameters must be applied. In this case, a time-window of 8000 ms and scroll increment of 4000 ms is shown.

The different parameters within time window stacking and percent keep functions have been explored on these data with variable results. For example, using a time window of 4000 ms, a scroll increment of 2000 ms, and a percent keep of 100%, the resolution of both the fundamental mode (M0) and the first higher mode (M1) is increased (Figure 29 and Figure 30a). Utilizing a percent keep of 90%, higher resolution between the two modes (M0 and M1) and a more pronounced low frequency trend within the fundamental mode is observed (Figure 30a and Figure 30b). However, eliminating too many overtones prior to stacking images can decimate the data in a negative way by eliminating desired signal. Using the same record (Figure 29), an 80% percent keep actually decreases the resolution of the low frequency trend. This suggests an 80% keep is likely eliminating a time window that includes helpful surface-wave energy (Figure 30).

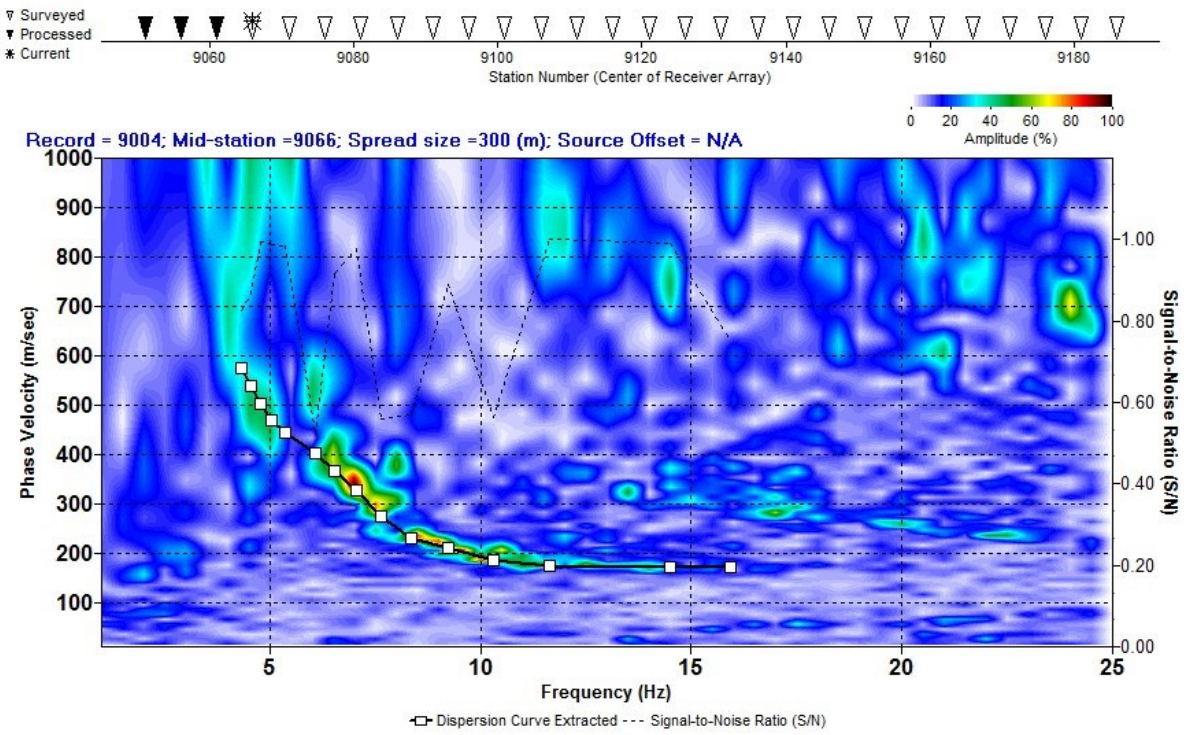

Figure 29: Overtone image with the fundamental mode dispersion curve highlighted. This overtone image was generated using default parameters, and no enhanced processing techniques.

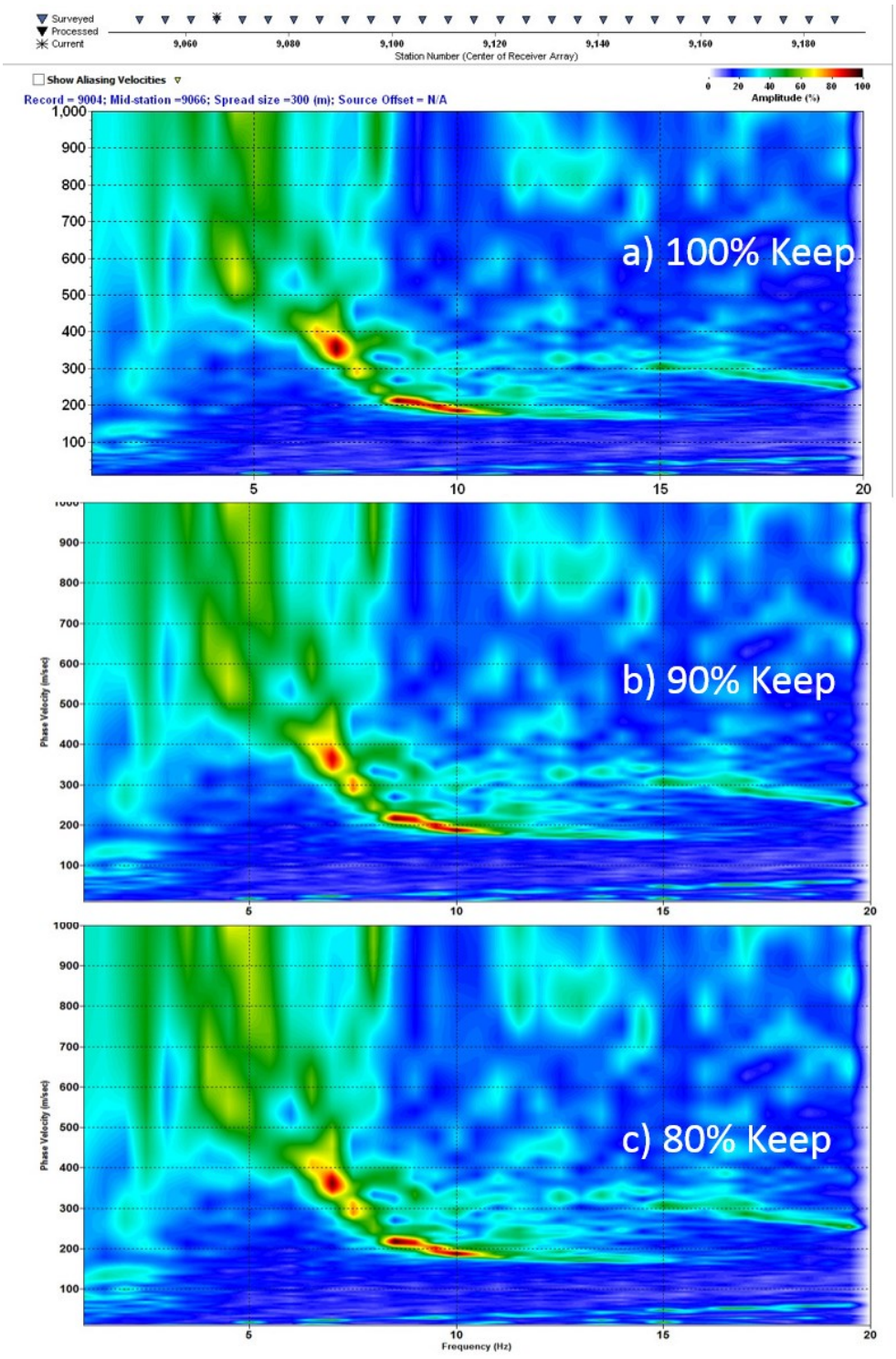

Figure 30: Time-window percent keep sensitivity utilizing a record that has been time-window stacked with a 4000 ms window and a 2000 ms scroll increment to produce a total of 15 total windows. a) 100% percent keep keeps all 15 windows. b) A 90% keep eliminated 2 records without decimating the overall quality of the high-amplitude trend. c) The 80% keep in this particular case, has excluded 3 windows, but reduced the resolution of the low frequency trend in the fundamental mode.

The time-window stacking and percent keep functions have generated overtones with a more pronounced fundamental mode dispersion curve. If the overtone image is noisy (incoherent, discontinuous, or clearly influenced by higher modes), the selection of a new source record may be required. Another overtone image enhancement is the combination of multiple source gathers. Similar to the time window stacking, these source gathers are vertically stacked in the frequency domain. To ensure accurate results the pre-stacked overtone images for both source records are generated with the same parameters. This technique can also significantly improve the coherency of the fundamental mode and produce a broadband continuous overtone image by increasing the signal-to-noise ratio (Figure 31). For instance, an overtone image with high-amplitude low-frequencies (down to ~3 Hz) (Figure 31a) vertically stacked with an overtone image with high-amplitude high-frequencies (~20 Hz) (Figure 31b), produce a high-amplitude broadband dispersion curve on the final overtone image (Figure 31c). However, the proper selection of in-line sources is vital for overtone enhancement. If one source is oblique, and one in-line, the elevated apparent velocities from the oblique source will contaminate the signal from the in-line producing a low signal-to-noise, undesirable overtone image with significant challenges for picking a dispersion curve.

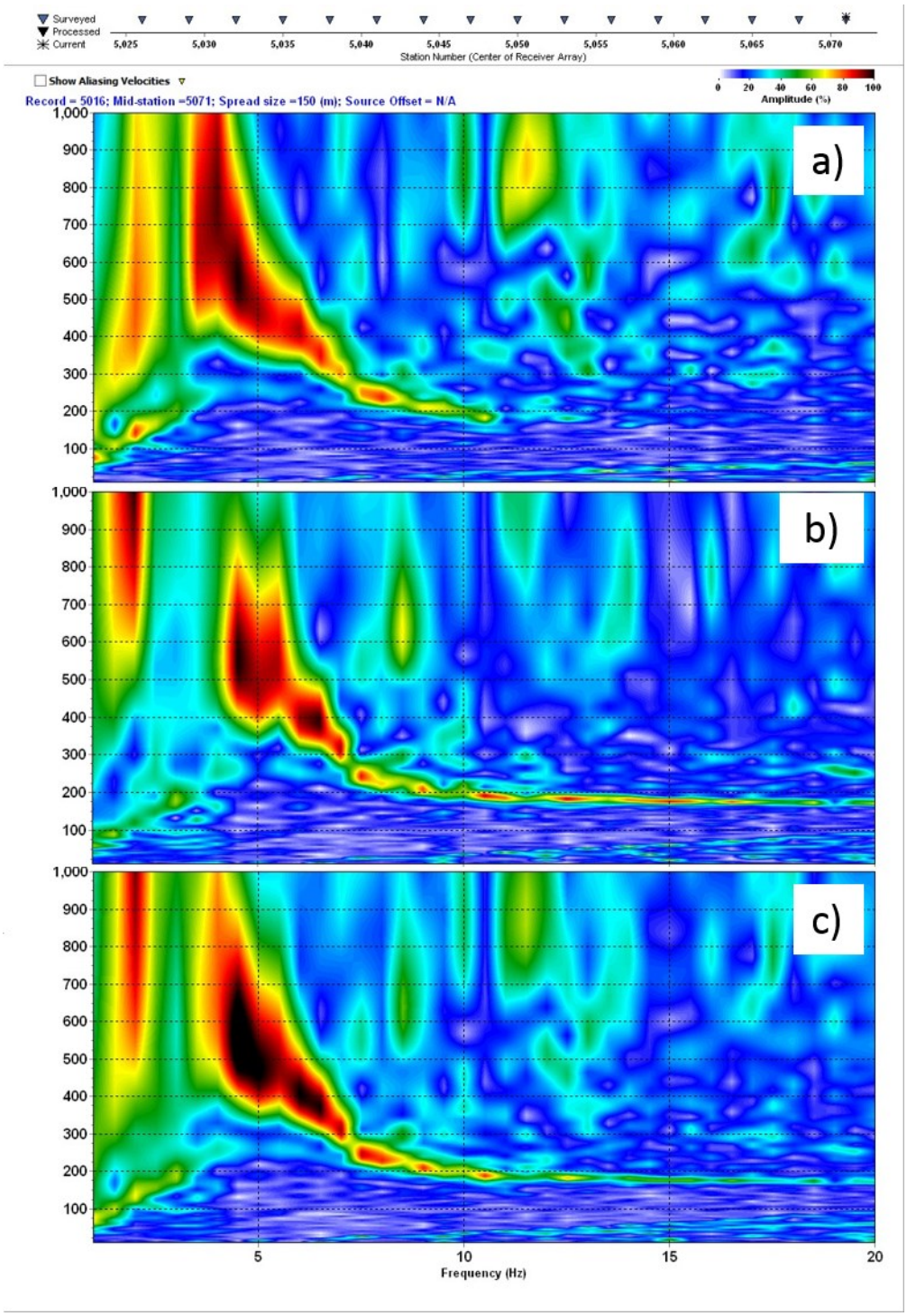

Figure 31: An overtone image with good low-frequency energy (a), an overtone image with good high-frequency signal (b), stacked together to form a broadband high-amplitude fundamental mode (c).

Once dispersion curves have been extracted, they are inverted (Xia et al., 1999; Xia et al., 2008) into a 1D velocity function using a Least-Squares approach. This 1D velocity function averages the velocity across the chosen spread (Figure 32) and assigned to the midstation of the record. These midstations are spaced at the chosen processing interval, as discussed earlier. Each of these 1D velocity functions are then gathered according to spatial distribution and interpolation between sample points to generate a 2D shear-wave velocity profile. This interpolation has several different possible a priori inputs, including P-wave velocity, density, P-wave/S-wave ratio, or S-wave velocity based on another method.

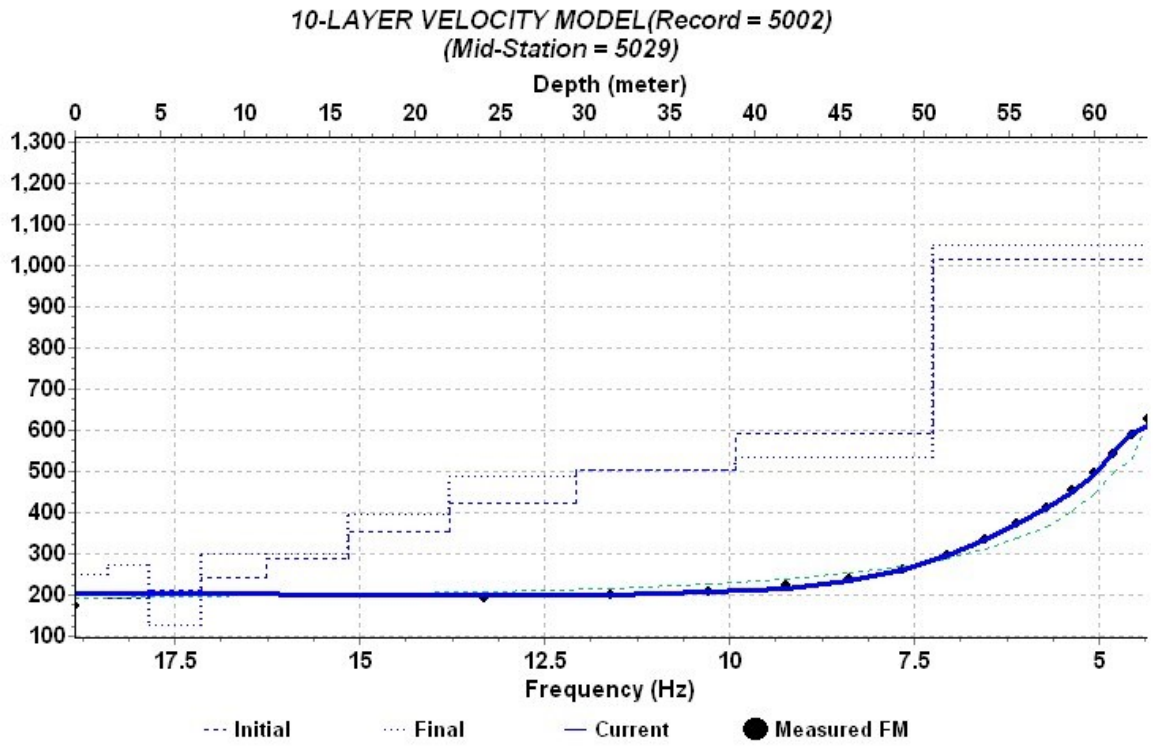

Figure 32: 1D velocity function for a 1D survey line. This represents one dispersion curve picked, assigned to one midstation.

Processing Setbacks

Processing at this site was challenging for a couple reasons. The number of clear sources was limited, as there were fewer than 10 train passing events with clear signal in the desired orientation for each survey line. However, combining multiple sources overcomes the low sampling coverage. Combining multiple sources with compatible characterization helped boost the signal from the trains and attenuate the majority of the other random cultural noise (Figure 33). Aside from combining multiple sources, enhanced processing such as time-window stacking was utilized to boost the confidence in the selection of the fundamental mode energy on the overtone images (Figure 34).

Ground Truth

Numerous well logs have been acquired throughout the survey area. However, the majority of these logs are either unavailable or do not contain samples within the desired intervals. A downhole shear-wave vertical seismic profile (VSP) acquired in a well at the site (Miller et al., 2009) provided a plot of the average shear-wave velocity with depth. The raw data for this VSP was unavailable, so the actual values were estimated from a cross plot of shear-wave velocity vs. depth (Figure 35) (Miller et al., 2009). Using the Dix Equation, the interval velocities can be calculated from the average velocities to produce a 1D velocity function. This 1D velocity function is then replicated to enhance visualization of the vertical range and variability of the V_S function (Figure 36). The calculated 2D velocity profile can serve as the comparison to insure final velocity profiles produced by the passive MASW approach are accurate.

Perfect correlation between the downhole model and the resulting velocity profiles are not expected. This downhole model was created using extracted values from a published plot rather than the actual values. This can produce velocities that are estimated, and close, but not exact. The downhole model was also generated using a single VSP. Multiple VSPs would be ideal when creating a velocity model over an area with significant geologic variation.

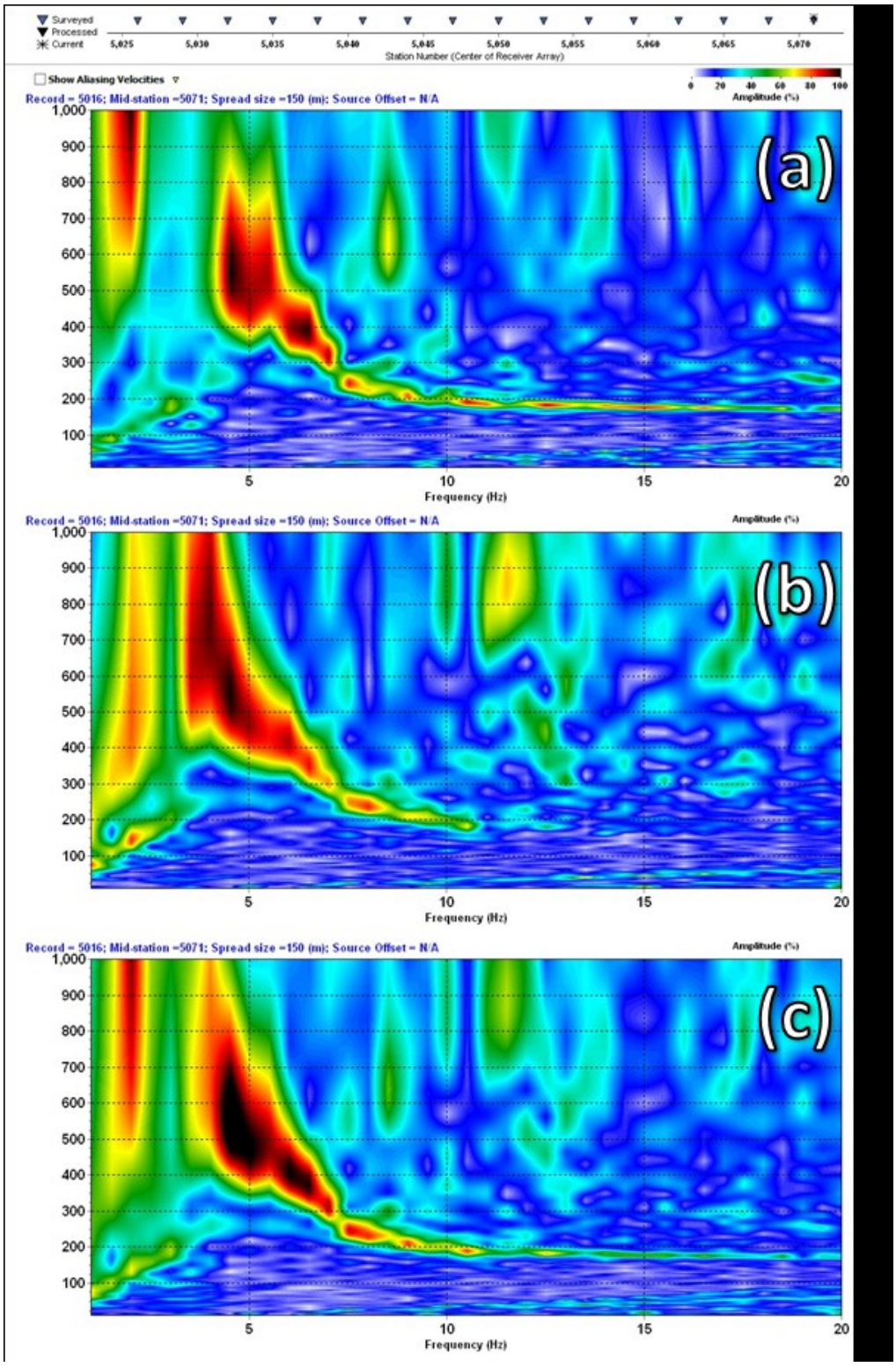

Figure 33: (a) represents a single source with good high frequencies, (b) represents a source with a good low frequency trend, and (c) represents the combination of these two sources.

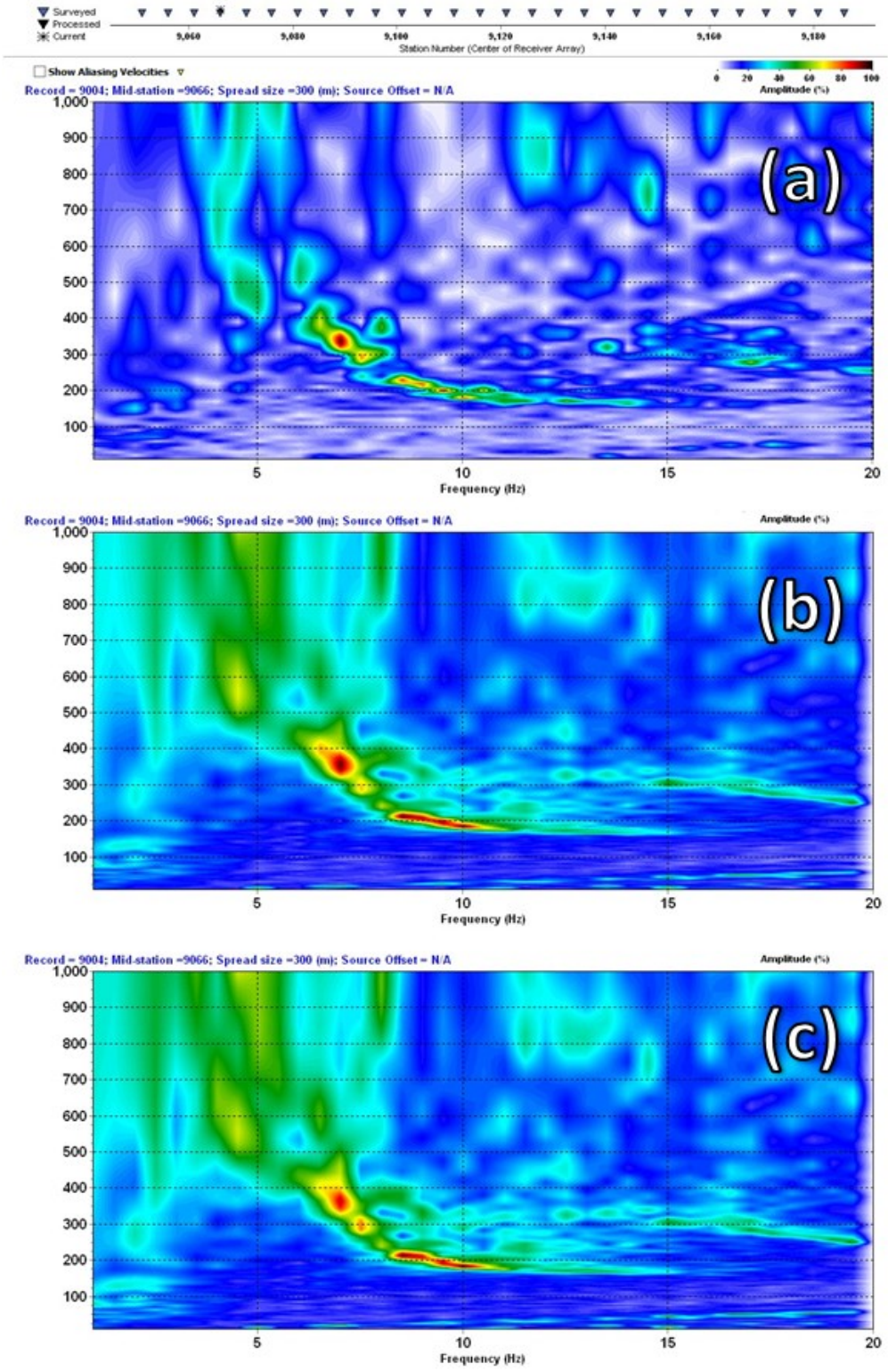

Figure 34: (a) represents the original overtone image, (b) represents the initial time-window stacking using a time-window of 4000 ms and a scroll interval of 2000 ms, and (c) represents the time-window stacked overtone with a percent keep of 90%.

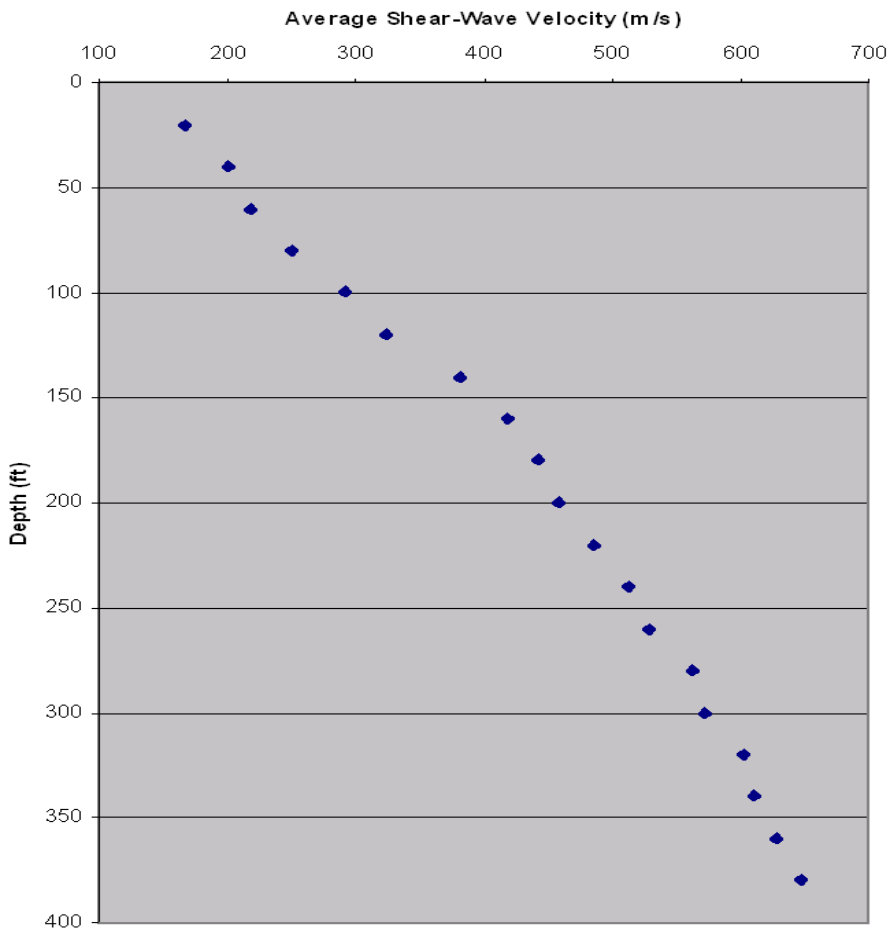

Figure 35: Average downhole shear-wave velocity produced from a VSP (Miller et al., 2009).

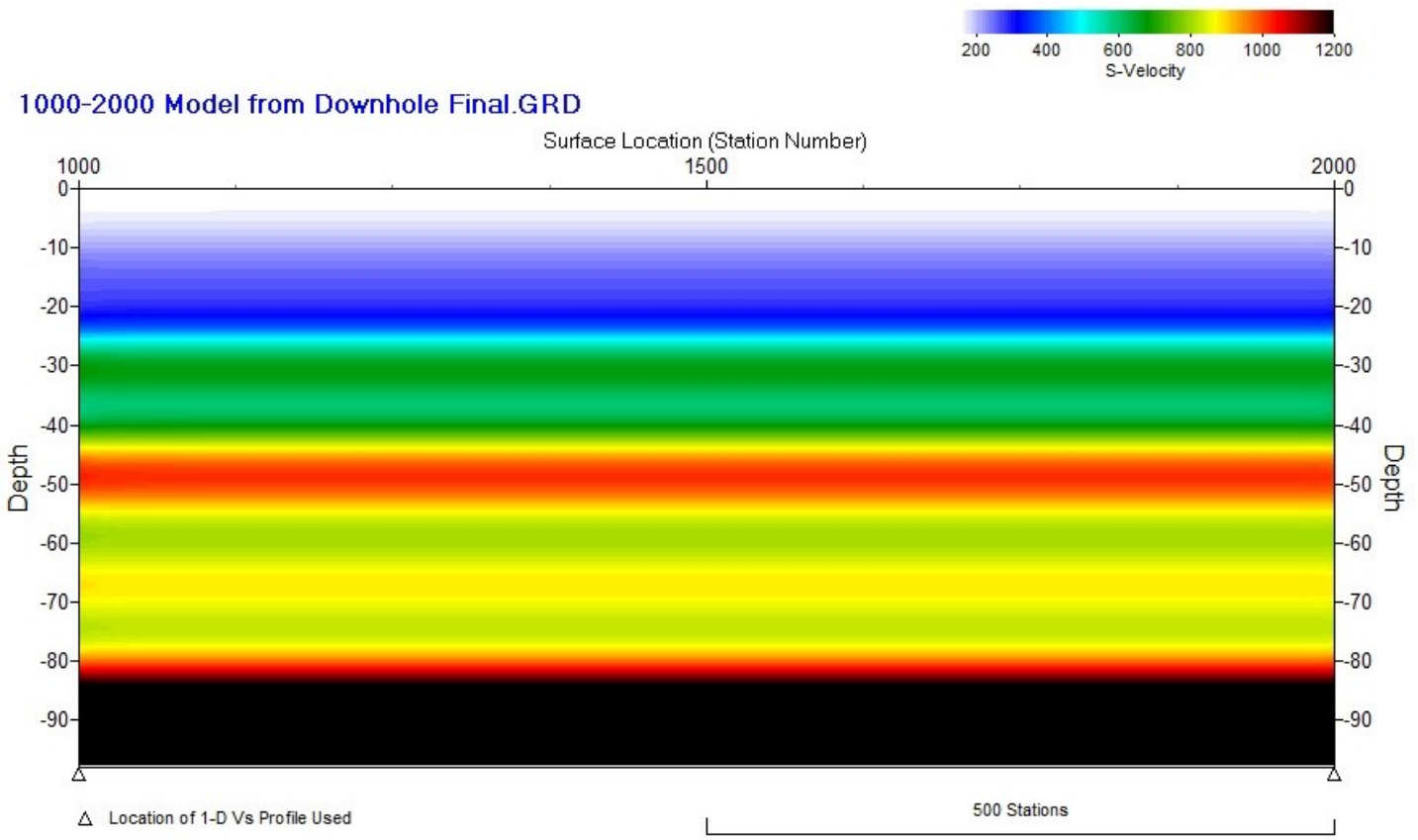

Figure 36: Downhole model to compare to the final velocity profiles produced from the interval velocities calculated from the average downhole velocity.

RESULTS

Line 1 is oriented east-west, covering 2 wells (W2A and W1B). Original processing for Line 1 was done by the KGS staff, then reprocessed. From Table 2, the line orientation and source orientation are approximately 15° apart, allowing for an approximate 4% increase in velocity. The final velocity profile was adjusted by 4% to eliminate potential error due to the oblique source. The resulting velocity profile for Line 1 (Figure 37) is fairly consistent with the downhole model calculated from the downhole VSP. Line 1 crosses Line 11 at approximately station 1097 and Line 2 at approximately station 1073. Overall, the velocity gradients at both intersections are consistent between the two lines. The velocity structure is layered and laterally consistent, most notably it lacks areas of elevated velocities indicative of significant stress accumulation. The sampling depth ranges from ~70-100 meters, while the velocity ranges from approximately 150 m/s at the surface to approximately 1100 m/s at maximum sampling depth. There is a small anomaly overlying well 1B, at approximately midstation 1060, identifiable by a slight increase in velocity (<10%) relative to surrounding areas. Despite the increase is sampling depth between the two wells, the overall velocity gradient remains constant.

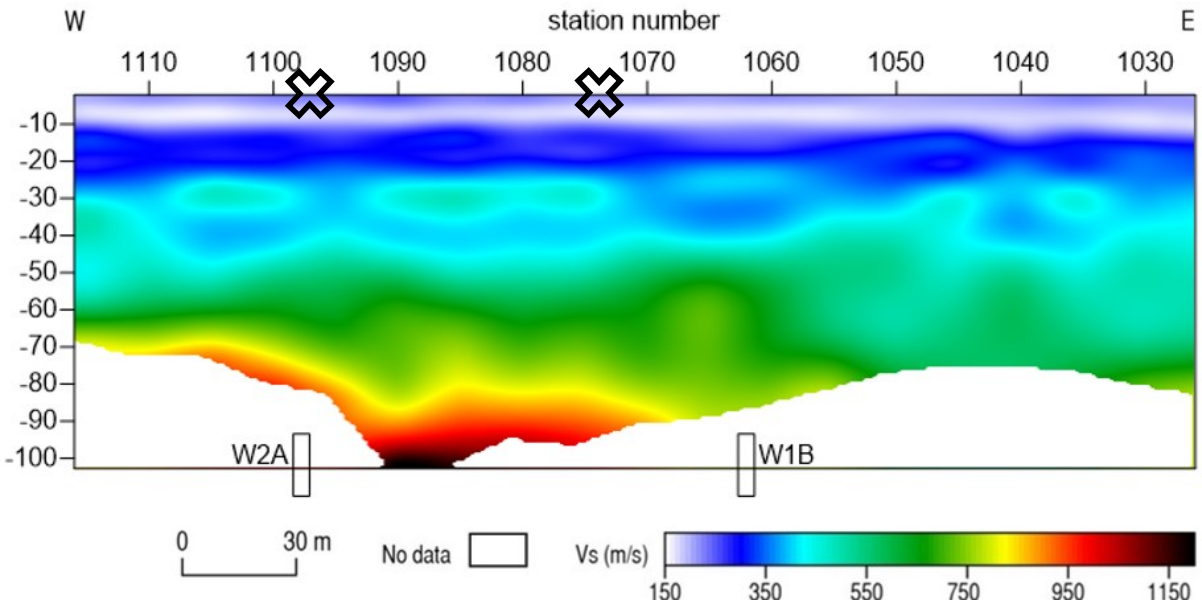

Figure 37: 2D vertical shear-wave velocity profile for Line 1. The 'X' at station 1097 highlights the intersection of Line 11 and the 'X' at station 1073 highlights the intersection of Line 2.

Line 2, a north-south oriented line, crosses a single well (W3B). Original processing for Line 2 was done by the KGS staff, then reprocessed. From Table 2, the line orientation and source orientation for Line 2 is approximately 30°, allowing for an increase in velocity of approximately 15%. The final velocity profile has been adjusted to eliminate the velocity error associated with the oblique source orientation. Line 2 crosses multiple lines (Line 1 at station 2058, Line 3 (no overlap in velocity profiles), Line 4 at station 2026, and Line 5 at station 2041). The velocity profile along Line 2 (Figure 38) is consistent with the downhole model velocity. The depth of sampling is about 70-90 meters, and the velocity ranges from ~150 m/s at the surface to ~900 m/s at maximum sampling depth.

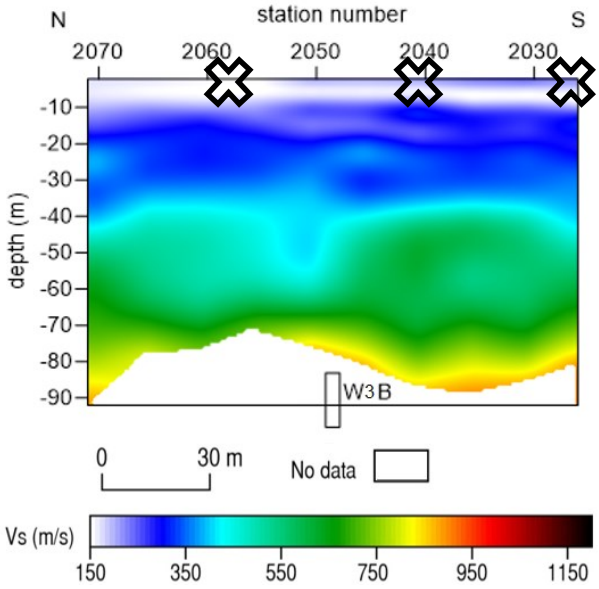

Figure 38: 2D vertical shear-wave velocity profile for Line 2. The 'X' at station 2058 highlights the intersection of Line1. The 'X' at station 2041 highlights the intersection of Line 5. The 'X' at station 2026 highlights the intersection of Line 4.

Throughout the majority of the velocity profile for the east-west oriented Line 3 (Figure 39), the velocities and velocity structure are consistent with the downhole model. Processing used for Line 3 was done by the KGS staff using variable time-window stacking parameters. From Table 2, the source orientation and line orientation differ by approximately 15%, allowing for approximately 5% increase in velocity. The final velocity profile has been adjusted to eliminate the velocity error associated with the oblique source orientation. Line 3 passes the southern portion of Line 2 and Line 11, but no overlap in the final velocity profiles. Sampling depths from 60-90 meters are as expected based on spread lengths utilized and frequencies recorded. The velocity range for this line is similar to the other lines, from approximately 150 m/s at the surface to 1050 m/s at the maximum depth of sampling. However, an elevated

velocity of about 18-20% is observed directly over W5B. The diameter of the anomaly is approximately 65 meters. This size and amplitude (>15% increase in velocity) of this anomaly indicatives the rocks overlying the void may have started accumulating stress above the known dissolution void. Although this anomaly could suggest elevated stress, an area of low velocity directly below the high velocity halo is not observed as in previous studies over migration voids (Sloan et al., 2009; Sloan et al., 2010). This is suggestive that roof rock is under increased stress, but has either not started migration into the 3-finger dolomite (~70-m) or the low velocities within the void are below the sampling depth. Because the 3-finger dolomite in theory should hinder the collapse process (Figure 15) due to the rocks' stiffness, collapse due to this void in not considered imminent or high-risk until the void itself has migrated into the 3-finger dolomite.

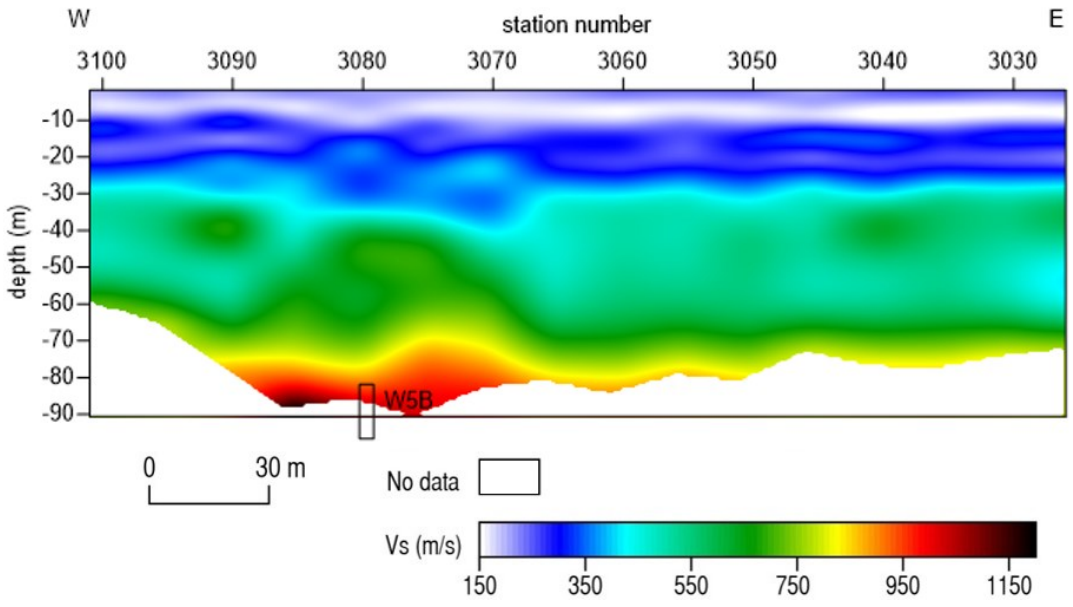

Figure 39: 2D vertical shear-wave velocity profile for Line 3 (modified from (Ivanov et al., 2013)).

The velocity profile for the east-west oriented Line 4 (Figure 40) shows a uniform velocity gradient consistent with the downhole model and other profiles within the survey area. From Table 2, the source orientation and line orientation differ by only 2%, ensuring less than 1% error associated with the slightly oblique source orientation. Line 4 crosses the southern portion of Line 11 and Line 2, with no overlap in final velocity profiles. The velocity structure over W6B seems to be consistent within geologic variation, signifying a normal stress regime. Sampling depths of approximately 70-80 meters are consistent with the other lines at this site. The observed velocity range is also consistent with the downhole model and other lines, ranging from approximately 150 m/s at the surface to approximately 1000 m/s at the maximum depth of investigation.

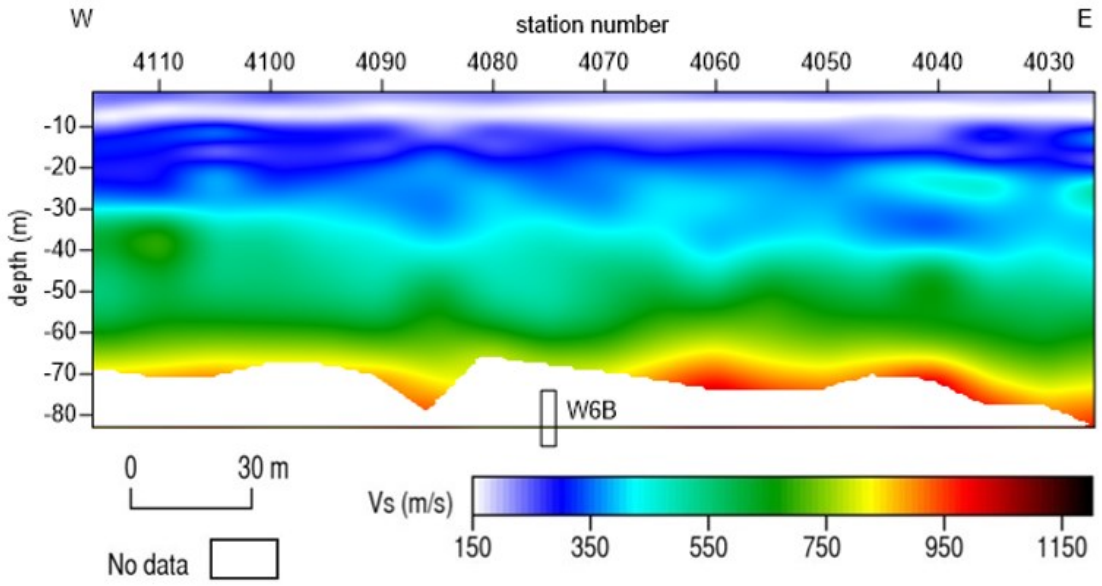

Figure 40: 2D vertical shear-wave velocity profile for Line 4.

Utilizing the combination of multiple sources in the processing of Line 5, the resulting velocity profile (Figure 41), an east-west line, also shows consistency in the velocity structure and gradient as expected from the downhole model. From Table 2, the line orientation and source orientation for line 5 differ by only 6°, producing less than 1% error in the velocity profile from the slightly oblique source. Line 5 crosses Line 2 at station 5080 and Line 11 at station 5093. The velocity gradient at the intersection of both lines are consistent with the velocity profile for Line 5. Depth of sampling is approximately 70 meters across the whole line, which is also in the expected range. The velocities range from approximately 150 m/s at the surface to approximately 950 m/s at the maximum depth of sampling, which is consistent with the other lines, as well as, the model. A slight increasing westward velocity gradient is observed starting between W2B and W4B. This change in velocity is approximately 10% and due to the shape and gentle uniform structure, is likely geologic variation.

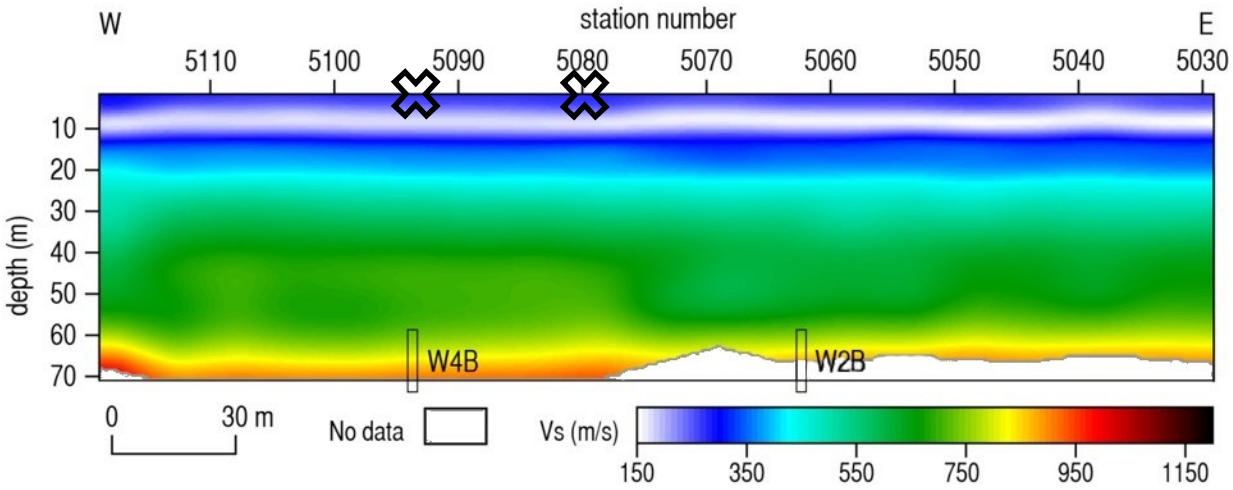

Figure 41: 2D vertical shear-wave velocity profile for Line 5 (modified from (Ivanov et al., 2013)). The 'X' at 5093 highlights the intersection of Line 11. The 'X' at station 5080 highlights the intersection of Line 2.

Line 9 is oriented north-south and covers 5 wells. From Table 2, the source orientation and line orientation only differ by 6°, ensuring a minimal increase in velocity of less than 1% due to the slightly oblique source. Processing for Line 9 was done in a group effort by the KGS staff. The northernmost 75 meters of the velocity profile for Line 9 (Figure 42) are consistent with the velocity structure and velocity gradient for lines 1, 2, 3, 4, and 5. Depths of sampling are approximately 70-80 meters, consistent with other lines at the site. Velocity ranges from approximately 150 m/s at the surface to 1000 m/s at the depth of maximum sampling, also consistent with other lines in this area. Around mid-station 9180, between W17 and W45, the velocity structure appears to transition into an area of elevated velocity. This increase is considered to be due to geologic variation, similar to the structure in Line 5, because of the relatively small increase in velocity (~10%) and the gentle uniform shape of the anomaly. A significant velocity anomaly, representing an approximately 20% increase in velocity is observed over W53, or midstation 983. This increase in velocity could suggest stress accumulation above the void. A third velocity anomaly is observed over W52. However, this anomaly is represented by an approximate 15% decrease in velocity. This decrease in velocity could be suggestive of a recent cyclical migration/expansion collapse event.

During this void migration process, low velocity zones are expected when fracture/collapse of overlying rock results in a decrease of shear stress. The bulking of rock fragments through void migration is expected to leave a trail of low shear-wave velocity because mechanically altered rock possess lower velocities than consolidated rock. Bulking can also arrest vertical migration and stabilize the overburden. As the void expands, the roof span also increases. This increase in the roof span will cause the accumulation of stress above the

void. The void associated with W52 has likely undergone a series of minor bulking and vertical void migration, followed by slight horizontal expansion. However, this velocity structure overlying this void does not suggest a serious threat at this time because the stresses associated with the overburden load have not started accumulating over these wells again.

Line 10 is a relatively short profile oriented east-west covering W2A. Line 10 crosses Line 11, Line 1, and Line 2, but the resulting velocity profiles for Line 10 only overlaps with Line 11 at station 2046. The velocity structure at this intersection is consistent on both velocity profiles. From Table 2, the source orientation and line orientation for Line 10 differ by approximately 11°, allowing for an increase in velocity of approximately 2%. The resulting velocity profile has been adjusted to eliminate the velocity error due to the oblique source orientation. The velocity profile for Line 10 (Figure 43) is consistent with other lines and the downhole model. The depths of sampling (80-90 meters) are consistent with other lines in the survey. The layered velocity structure features approximately 150 m/s at the surface and approximately 1000 m/s at the maximum depth of sampling. A slight velocity gradient increasing westward can be observed, but still does not contain drastically elevated velocity anomalies.

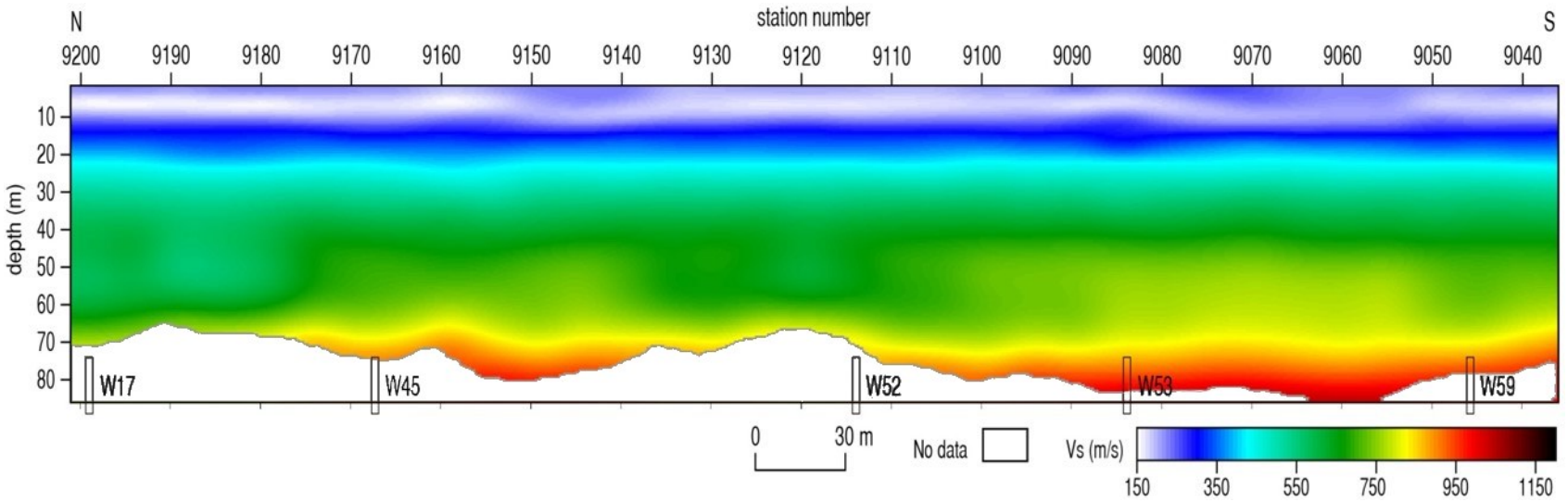

Figure 42: 2D vertical shear-wave velocity profile for Line 9.

Line 11 is oriented north-south and crosses two wells (W2A and W4B). Line 11 crosses Line 3, Line 4, Line 5 (station 1027), Line 10 (station 1052), and Line 1 (station 1055). However, no overlap in the final velocity profiles in Line 3 or Line 4 (Figure 44). As mentioned before, the velocity structure at the intersection of Line 10 and Line 11 is consistent. This line crosses a building, therefore multiple stations in the middle of the spread are left vacant. This is likely the reason for the greater variability in the sampling depth (60-100 meters). The velocity ranges from approximately 150 m/s at the surface to approximately 1100 m/s at the maximum sampling depth. The layered velocity structure and velocity gradient are consistent with the intersecting Line 10, other lines within the site, and the calculated model.

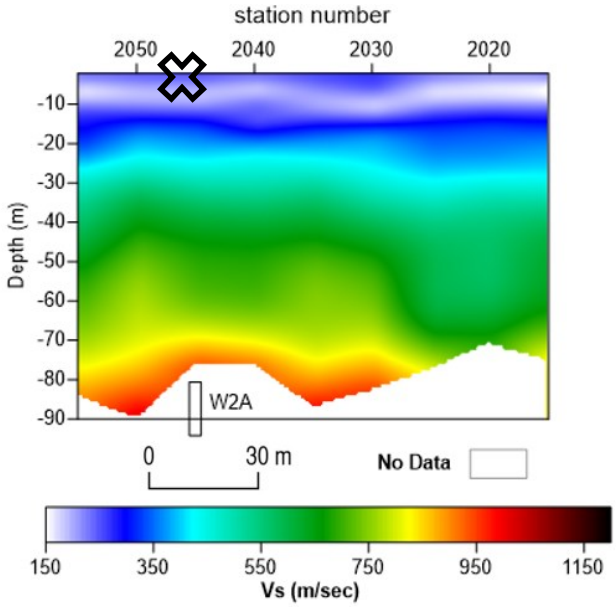

Figure 43: 2D vertical shear-wave velocity profile for Line 10. The 'X' at 2046 highlights the intersection of Line 11.

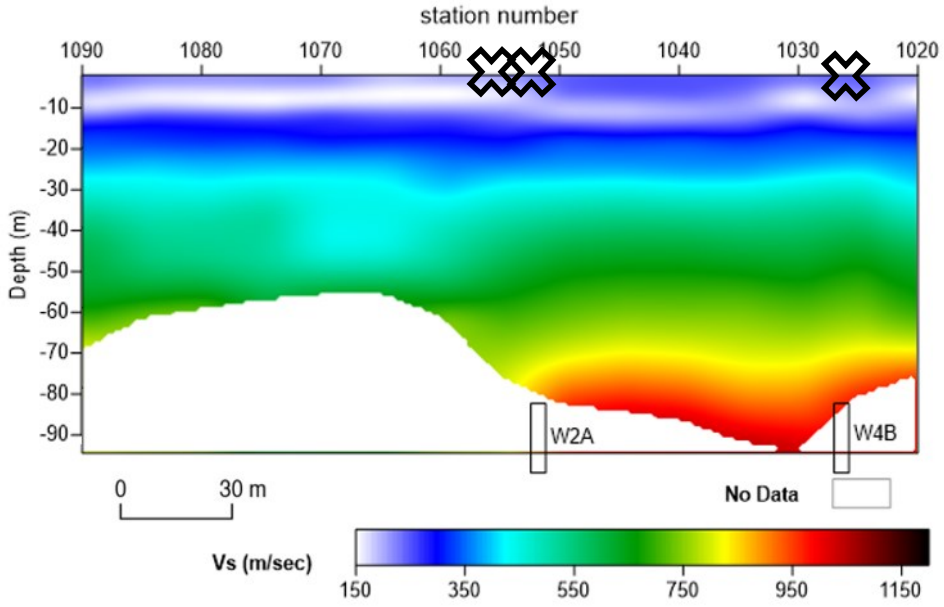

Figure 44: 2D vertical shear-wave velocity profile for Line 11. The 'X' at 1055 highlights the intersection of Line 1. The 'X' at 1052 highlights the intersection of Line 10. The 'X' at 2037 highlights the intersection of Line 5.

DISCUSSION

The characterization of the velocity structure overlying salt solution voids within the study area was effective. Velocity anomalies at this site have been identified within the velocity profiles which suggest void migration and/or lateral expansion has begun in some of the subsurface voids. The acquisition of these data reaches similar depths of investigation as a previous passive surface-wave investigation (Leitner, 2015). This site provides very good passive seismic energy sources capable of producing frequencies down to approximately 4 Hz. The acquisition of the 2D grid ensured the accuracy of all velocities by providing an azimuthal direction of dominant surface-wave energy propagation. By identifying the source orientation on the 2D grid, the elevated apparent velocity due to the oblique source can be corrected to eliminate one source of error. The enhanced processing procedures, such as time-window stacking and combining multiple passive sources increased the coherency and produced overtone images with a more pronounced fundamental mode across records with higher signal-to-noise ratios (Figure 33 and Figure 34).

The enhancements on the overtone images significantly impact the final velocity profile. By processing these data with the legacy processing procedure, a comparison of the velocity profiles with and without the enhanced processing procedures can be observed (Figure 45). While overall, the general velocity gradients of the two profiles are reasonably consistent, the prominent dome-shaped velocity anomaly on the western side of Figure 45a, is not as well defined in the velocity profile without using enhanced processing procedures in Figure 45b. While the anomaly can be identified in both profiles, the enhanced processing procedures

produced a velocity profile with a prominent velocity anomaly associated with the changes in stress within the overburden.

By acquiring passive seismic data with a 2D grid and numerous 1D survey lines simultaneously, passive MASW techniques can be explored in other areas where other surface-wave methods are not effective. Utilizing the enhanced processing steps within this study can create overtone images with higher signal-to-noise ratios. This, in turn, allows for higher confidence in the extraction of the fundamental mode dispersion curve, which increases the confidence in the final velocity profile. Utilizing this method in other areas where future subsidence events such as karst environments, other salt solution well fields, or other natural or anthropogenic dissolution features could be beneficial to determine areas with elevated risks of surface collapse.

Once the dispersion curve has been extracted and inverted the final velocity profile has interpolation connecting the sample points. To understand the amount of interpolation and the amount of sample points, an overlay of sample points on the final velocity profile is generated (Figure 46). Sampling the data every 5 stations (15 meters) is well within the limits of the horizontal resolution of the MASW technique (Park, 2005). Vertically, the MASW method has proven to match borehole measurements very well (Xia et al., 2000). This overlay shows there is significant coverage throughout the velocity profile, with minimal chance for large scale velocity artifacts produced from the inversion and interpolation.

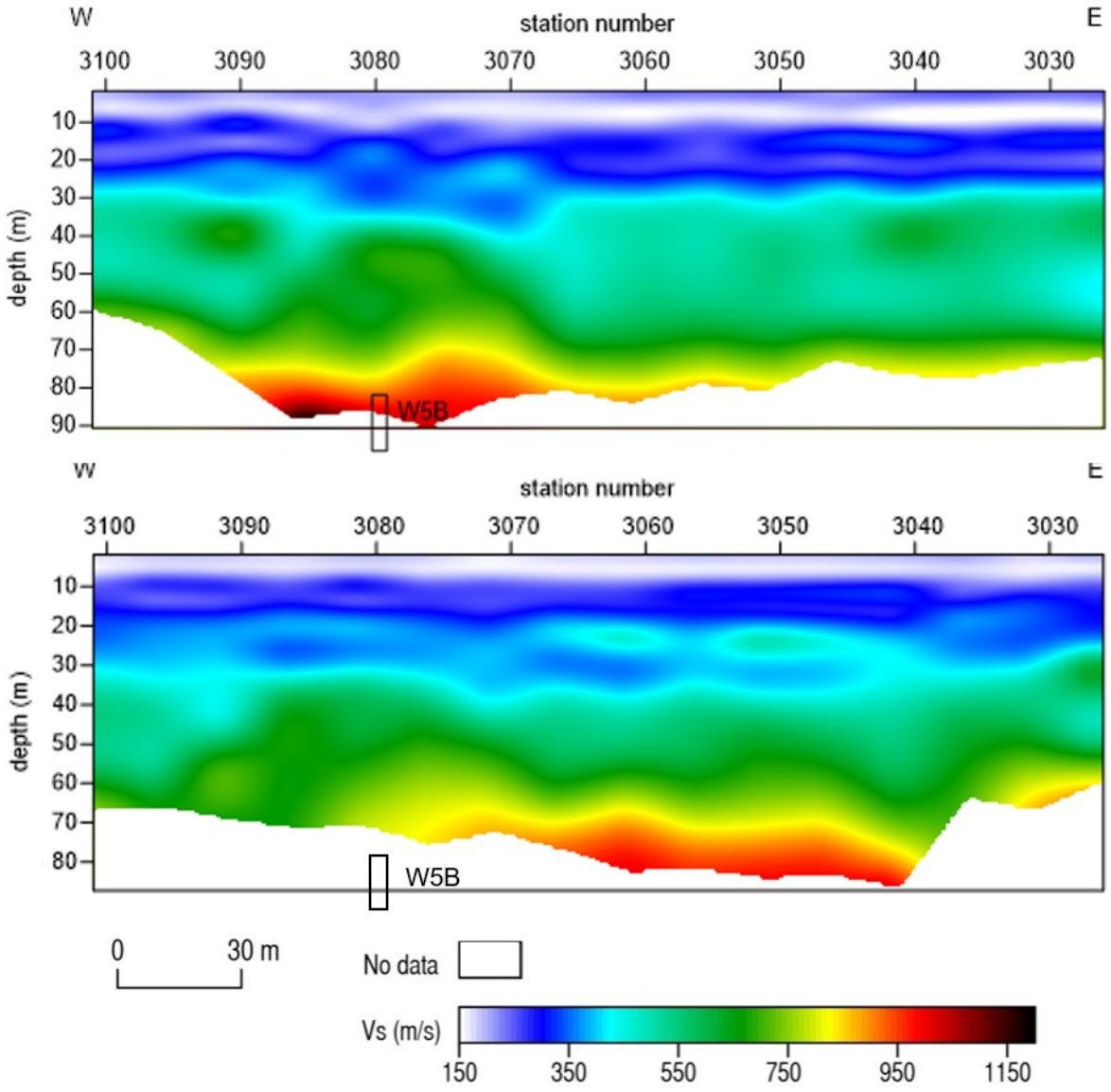

Figure 45: Comparison between the 2D vertical shear-wave velocity profile using enhanced processing procedures (a) (modified from (Ivanov et al., 2013)) and the 2D vertical shear-wave velocity profile for Line 3 using the legacy processing procedure (b). Notice the velocity anomaly centered about the well W5B in (a) is much more defined than the profile in (b).

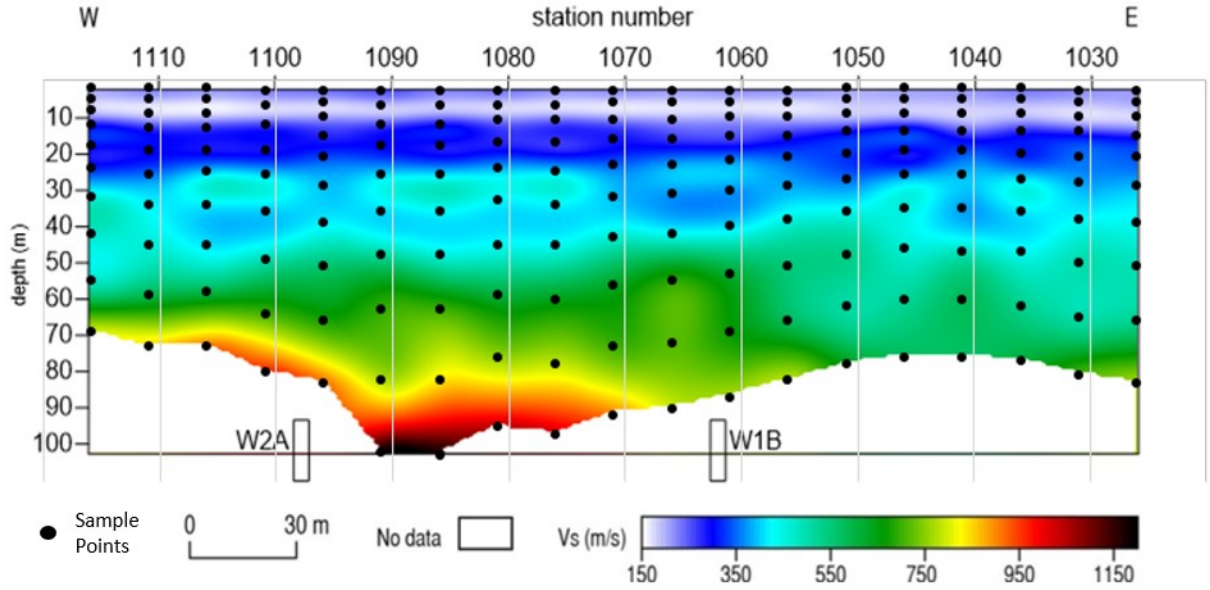

Figure 46: 2D vertical shear-wave velocity profile for Line 1 with an overlay highlighting the sample points with the black dots.

CONCLUSIONS

Enhanced processing procedures on passive multichannel analysis of surface-wave (MASW) data facilitated fundamental mode dispersion curve picking on overtone images, which in turn increased the confidence in the final velocity profile in an abandoned salt solution well field. Enhanced processing procedures unique to this study area include time-window stacking, percent keep, and the vertical stacking of multiple passive sources in the frequency domain. These enhancements can provide excellent opportunities to eliminate undesired “noise” on a passive record. Elimination of the undesired noise in this study significantly boosted the fundamental mode energy, creating a more continuous and coherent fundamental mode dispersion curve on the overtone images. These velocity profiles were then interpreted to determine the relative risk of subsurface, and ultimately surface, collapse.

From previous work in the study area, a preferred orientation of the 2D grid was determined and utilized in this study. The use of this 2D grid ensured velocities on the 1D survey contain in-line wave propagation by providing an azimuthal direction of the dominant surface-wave energy. Apparent velocities in the final velocity models were then corrected based off the source orientation provided by the 2D grid.

Analysis of passive MASW data has provided insight to the status of the overburden without requiring invasive investigations. The status of the overburden above each void has been analyzed and provided sufficient evidence as to the relative potential of each void for subsurface collapse. Shear-wave velocity anomalies identified on the 1D survey lines are suggested to be due to the dynamic stress regime surrounding void migration and void

expansion. None of these velocity anomalies were considered high risk for immediate surface collapse, so no actions were taken as of now based on this study. Aside from the actual analysis of the overburden associated with numerous subsurface voids within the site, this study increased the confidence of the velocity structure at the target depth (Figure 45) by producing overtone images with more pronounced fundamental modes (Figure 33 and Figure 34). Surface-wave studies containing contaminated, incoherent fundamental mode energy can utilized these processing procedures to generate an overtone with a higher signal-to-noise ratio. The sampling depths were much improved from previous active surveys (Miller et al., 1993; Miller et al., 2005; Miller et al., 2009), and were sufficient to identify velocity anomalies associated with the change in the shear modulus.

On a larger scale, these acquisition parameters and processing procedures from this study can be utilized at other sites to analyze the shear-wave velocity structure over similar features in the area. This technique and processing procedures have already been utilized at another site within Hutchinson, Kansas, also using energy from nearby trains as a target source. Assuming the desired frequency range of passive wave signal is available, and the geology allows for the dispersive nature of the surface waves, these acquisition and processing procedures can be utilized at other sites around the world with varying objectives. The analysis of the physical properties of potential subsurface collapse features using this enhanced processing procedures in the passive surface-wave method is a technique that can be utilized in other areas susceptible to subsidence. However, this particular site is an anomaly in itself. The presence of trains oriented in the desired direction is a luxury not all sites possess. The presence of high signal-to-noise, low dominant frequency, and a broad-bandwidth signal source

is a key factor to the accurate and effective characterization of the velocity structure. This is an excellent and rare site for testing and developing the method.

The addition of well logs for each well throughout the study area can add another tool to help determine the collapse process. These well logs could identify impermeable stringers, which likely impedes the migration of the void. While an accumulation of stresses may take some time to build up, relief can occur instantaneously. This means the velocity structure, along with other physical characteristics are not real-time material properties during void migration. The acquisition of time-lapse data would add another dimension to developing the understanding of the status of each void.

REFERENCES

Asten, M. W., and Boore, D. M., 2005, Blind Comparisons of Shear wave Velocities at Closely-Spaced Sites in San Jose, California: U.S. Geological Survey Open-File Report 2005-1169.

Baars, D. L., Watney, W. L, Steeples, D. W., and Brostuen, E. A., 1989, Petroleum: a primer for Kansas: Kansas Geol. Survey, Education.

Barczak, T. M., 2006, A Retrospective Assessment of Longwall Roof Support with a Focus on Challenging Accepted Roof Support Concepts and Design Premises: Proceedings of 25th International Conference on Ground Control in Mining, August 1-3, 2006, S. S. Peng, C. Mark, G. Finfinger, S. Tadolini, A. W. Khair, K. Heasley, and Y. Luo, eds. Morganton, West Virginia: West Virginia University, p. 232-244.

Båth, M., 1973, Introduction to seismology: A Halsted Press Book, 395.

Boiero, D., and Socco, L. V., 2014, Joint inversion of Rayleigh-wave dispersion and P-wave refraction data for laterally varying layered models: Geophysics, 79, no. 4, EN49-EN59.

Davies, W.E., 1951, Mechanics of cavern breakdown: National Speleological Society, 13, 6-43.

Dobrin, M. B., and Savit, C. H., 1988, Introduction to geophysical prospecting, 4th ed.: McGraw Hill, Inc., 867.

Dvorkin, J., Nur, A., and Chaika, C., 1996, Stress sensitivity of sandstones: Geophysics, 61, 444-455.

Eberhart-Phillips, D., D.-H. Han, and M. D. Zoback, 1989, Empirical relationships among seismic velocity, effective pressure, porosity, and clay content in sandstone: Geophysics, 52, 82-89.

Ege, J. R., 1979, Surface subsidence and collapse in relation to extraction of salt and other soluble evaporites: United States Department of the Interior Geological Survey, Open-File Report 79-1666.

Grant, F.S., and West, G.F., 1965, Interpretation theory in applied geophysics: McGraw-Hill Book Company, New York.

Haskell, N. A., 1953, The dispersion of surface-waves on multilayered media: Bulletin of the Seismological Society of America, 43, 17-34.

Hayashi, K., and Hirade, T., 2008, Application of surface-wave method to the evaluation of local site effect of earthquake: SEG Technical Program Expanded Abstracts 2008, 1288-1292.

Hayashi, K., and Inazaki, T., 2006, Surface-wave method using land streamer and its application to civil engineering investigations: Symposium on the Application of Geophysics to Engineering and Environmental Problems (SAGEEP 2006).

Hayashi, K., Inazaki, T., and Suzuki, H., 2005, Buried channel delineation using a passive surface-wave method in urban area: Symposium on the Application of Geophysics to Engineering and Environmental Problems (SAGEEP 2005), 1043-1050.

Hayashi, K., Tamura, M., Hirade, T., Adhikari, K. N., and Shizhou, Y., 2008, Application of surface-wave method to the evaluation of local site effect of 2007 Noto earthquake: Symposium on the Application of Geophysics to Engineering and Environmental Problems (SAGEEP 2008), 1232-1239.

Heisey, J. S., Stokoe II, K. H., and Meyer, A. H., 1982, Moduli of pavement systems from spectral analysis of surface-waves: Transportation Research Record No. 852, 22-31.

Herwanger, J., and S. Horne, 2005, Predicting time-lapse stress effects in seismic data: The Leading Edge, 24, 1234-1242.

Ivanov, J., Leitner, B., Shefchik, W., Schwenk, J., and Peterie, S., 2013, Evaluating hazards at salt cavern sites using multichannel analysis of surface-waves: The Leading Edge, 32, no. 3, 298-305.

Ivanov, J., Miller, R. D., Peterie, S. L., Buchanan, R., McClain, B. E., and Altieri, J., 2011, Passive seismic characterization of high priority salt jugs in Hutchinson, Kansas: Proposal to William T. Shefchik, Burns & McDonnell Engineering Company.

Ivanov, J., Miller, R. D., Peterie, S. L., Schwenk, J. T., Nolan, J. J., Bennett, B., Wedel, B., Anderson, J., Chandler, J., and Green, S., 2013, Preliminary Report: Enhanced Passive Seismic Characterization of High Priority Salt Jugs in Hutchinson, Kansas: Preliminary Report to Ed Lindgren and Peter Burton, Burns & McDonnell Engineering Company.

Ivanov, J., Miller, R. D., and Tsoflias, G, 2008, Some practical aspects of MASW analysis and processing: Symposium on the Application of Geophysics to Engineering and Environmental Problems 2008, 1186-1198.

Ivanov, J., Miller, R. D., Xia, J., and Peterie, S., 2010, Multi-mode inversion of multi-channel analysis of surface-waves (MASW) dispersion curves and high-resolution linear radon transform (HRLRT): SEG Technical Program Expanded Abstracts 2010, 1902-1907.

Ivanov, J., Miller, R. D., Xia, J., Steeples, D., and Park, C. B., 2006, Joint analysis of refractions with surface-waves: An inverse solution to the refraction-traveltime problem: Geophysics, 71, R131-R138.

Kansas Geological Survey, 2001, Gas Storage, USA—Hutchinson Response Project: [http://www.kgs.ku.edu/Hydro/Hutch/GasStorage/index.html] (Aug. 2008)

Kaufmann, R. D., Xia, J., Benson, R. C., Yuhr, L. B., Casto, D. W., and Park, C. B., 2005, Evaluation of MASW data acquired with a hydrophone streamer in a shallow marine environment: Journal of Environmental and Engineering Geophysics, 16, no. 2, 87-98.

Khaksar, A., C. M. Griffiths, and C. McCann, 1999, Compressional- and shear wave velocities as a function of confining stress in dry sandstones: Geophysical Prospecting, 47, 487-508.

Lambrecht, Jamie L., 2006, Time-Lapse High-Resolution Seismic Imaging of a Catastrophic Salt-Dissolution Sinkhole in Central Kansas: Kansas Geol. Survey, Open-file Report No. 2006-23.

Landes, K. K., and Piper, T. B., 1972, Effect upon environment of brine cavity subsidence at Grosse Ile, Michigan, 1971: Solution Mining Research Institute, Inc., Flossmoor, Illinois 60422, p. 52.

Leitner, B., 2015, Passive multichannel analysis of surface-waves (MASW) study over salt dissolution voids: University of Leoben, Austria, Department of Applied Geosciences and Geophysics, Print.

Leitner, B., Miller, R. D., and Ivanov, J., 2011, Optimal spread design for passive MASW: 17th European Meeting of Environmental and Engineering Geophysics, Association of Geoscientists and Engineers.

Leonard, R. B., and Kleinschmidt, H. K., 1976, Saline water in the Little Arkansas River basin area, south-central Kansas: Kansas Geol. Survey, Chem. Quality Series 3, 24.

Louie, J. N., 2001, Faster, better: Shear wave velocity to 100 m depth from refraction microtremor arrays: Bulletin of the Seismological Society of America, 91, no. 2, 347-364.

Luke, B. A., Lee, B., Stokoe, K. H., and Wright, S. G., 1996, Influence of higher modes and test geometry on SASW measurements underwater: SEG Technical Program Expanded Abstracts, 851-854.

Luo, Y., Xia, J., Liu, Q., and Xu, S., 2007, Joint inversion of high-frequency surface-waves with fundamental and higher modes: Journal of Applied Geophysics, 62, 375-384.

Luo, Y., Xu, Y., Xia, J., Miller, R. D., Xu, Y., Liu, J., and Liu, Q., 2008, Rayleigh-wave dispersive energy imaging using a high-resolution linear radon transform: Pure and Applied Geophysics, 165, 903-922.

Martinez, J. D., Johnson, K. S., and Neal, J. T., 1998, Sinkholes in evaporate rocks: American Scientist, 86, 38-51.

Miller, R. D., Ivanov, J., Steeples, D. W., Watney, W. L., and Rademacker, T. R., 2005, Unique near-surface seismic-reflection characteristics within an abandoned salt-mine well field, Hutchinson, Kansas: SEG Technical Program Expanded Abstracts 2005, 1041-1044.

Miller, R. D., Sloan, S. D., Walters, S. L., Ivanov, J., Leitner, B., Rech, A., Wedel, B. A., Wedel, A. R., Anderson, J. M., Metheny, O. M., and Schwarzer, J. C., 2009, Shear wave Seismic Study above Vigindustries, Inc. Legacy Salt Jugs in Hutchinson, Kansas: Kansas Geol. Survey, Open-file Report No. 2009-3.

Miller, R. D., Steeples, D. W., Schulte, L., and Davenport, J., 1993, Shallow seismic reflection study of a salt dissolution well field near Hutchinson, KS: Mining Engineering, October, 1291-1296.

Miller, R. D., Xia, J., Park, C. B., and Ivanov, J. M., 1999, Multichannel analysis of surface-waves to map bedrock: The Leading Edge, 18, no. 12, 1392-1396.

Miller, R. D., 2007, High-resolution seismic investigation of subsidence from dissolution: University of Leoben, Austria.

Morton, S. L. C., Ivanov, J., and Miller, R. D., 2015, A modified FK filter for removing effects of higher-mode dispersion patterns from surface-wave data: Symposium on the Application of Geophysics to Engineering and Environmental Problems 2015, 445-451.

Nazarian, S., and Stokoe II, K. H., 1983, Evaluation of moduli and thicknesses of pavement systems by spectral-analysis-of-surface-waves method: Texas University Austin Report, Vol. 1.

Nazarian, S., Stokoe II, K. H., and Hudson, W. R., 1983, Use of spectral analysis of surface-waves method for determination of moduli and thicknesses of pavement systems: Transportation Research Record No. 930, 38-45.

Nelson, A., 1965, Dictionary of Mining: New York City, New York: Philosophical Library Inc.

Nissen, S. E., and Watney, W. L, 2003, Detailed mapping of the Upper Hutchinson Salt and Overlying Permian strata beneath Hutchinson, Kansas: Kansas Geol. Survey, Open-file Report No. 2003-66.

O'Neill, A., and Matsuaka, T., 2005, Dominant higher surface-wave modes and possible inversion pitfalls: Journal of Environmental and Engineering Geophysics, 10, 185-201.

Park, C. B., 2005, MASW—Horizontal Resolution in 2D Shear-Velocity (Vs) Mapping: Kansas Geological Survey Open-File Report 2005-4.

Park, C., and Miller, R., 2005, Multichannel analysis of passive surface-waves-modeling and processing schemes: Site Characterization and Modeling. October 2005, 1-14.

Park, C. B., and Miller, R. D., 2006, Roadside passive MASW: Symposium on the Application of Geophysics to Engineering and Environmental Problems (SAGEEP 2006), 1116-1127.

Park, C. B., and Miller, R. D., 2008, Roadside passive multichannel analysis of surface-waves (MASW): Journal of Environmental & Engineering Geophysics, 13, no. 1, 1-11.

Park, C. B., Miller, R. D., Ryden, N., Xia, J., and Ivanov, J., 2005a, Combined use of active and passive surface-waves: Journal of Environmental and Engineering Geophysics, 10, is. 3, 323-334.

Park, C. B., Miller, R. D., and Xia, J., 1997, Multi-channel analysis of surface-waves (MASW) "A summary report of technical aspects, experimental results, and perspective:" Kansas Geological Survey Open-file report 97-10.

Park, C. B., Miller, R. D., Xia, J., 1998, Imaging dispersion curves of surface-waves on multichannel record: 68th Annual International Meeting, SEG, Expanded Abstracts, 1377-1380.

Park, C., Miller, R., and Xia, J., 1999a, Multichannel analysis of surface-waves: Geophysics, 64, no. 3, 800-808.

Park, C., Miller, R., and Xia, J., 1999b, Multimodal analysis of high frequency surface-waves: Symposium on the Application of Geophysics to Engineering and Environmental Problems 1999, p. 115-121.

Park, C. B., Miller, R. D., Xia, J., Hunter, J. A., and Harris, J. B., 1999c, Higher mode observation by the MASW method: SEG Technical Program Expanded Abstracts 1999, 524-527.

Park, C. B., Miller, R. D., Xia, J., Ivanov, J., Sonnichsen, G. V., Hunter, J. A., Good, R. L., Burns, R. A., and Christian, H., 2005b, Underwater MASW to evaluate stiffness of water-bottom sediments: The Leading Edge, 24, no. 7, 724-728.

Park, C., Miller, R., Xia, J., and Ivanov, J., 2007, Multichannel analysis of surface-waves (MASW)—active and passive methods: The Leading Edge, 26, no. 1, 60-64.

Park, C. B., and Taylor, C., 2010, 3D MASW Characterization of Sinkhole: A Pilot Study at USF Geology Park, Tamp, FL: Proceedings of the Symposium on the Application of

Geophysics to Engineering and Environmental Problems (SAGEEP 2010), Keystone, CO, April 11-15, 498-507.

Peng, S. S., 1992, *Surface Subsidence Engineering:* Society for Mining, Metallurgy, and Exploration, Inc., 161.

Quiero, C. W., 1977, Current practices in solution mining of salt: in Martinez, J. D., and Thoms, R. L., eds., Symposium on salt dome utilization and environmental considerations, Baton Rouge, 1976.

Ratigan, Joe, April 2016, Phone Communication.

Richart, F. E., Hall, J. R., and Woods, R. D., 1970, Vibrations of soils and foundations: Prentice-Hall, Inc.

Rix, G. J., and Leipski, A. E., 1991, Accuracy and resolution of surface-wave inversion: in: Bhatia, S. K., and Blaney, G. W. Eds, Recent advances in instrumentation, data acquisition, and testing in soil dynamics: Am. Soc. Civil Eng. Geotechnical Special Publication No. 28, 17-23.

Ryden, N., Park, C. B., Ulriksen, P., and Miller, R. D., 2004, Multimodal approach to seismic pavement testing: Journal of Geotechnical and Geoenvironmental Engineering, 130, no. 6, 636-345.

Sayers, C. M., 2004, Monitoring production-induced stress changes using seismic waves: 74th Annual International Meeting, SEG, Expanded Abstracts, 2287-2290.

Sawin, R., and Buchanan, R., 2002, Salt in Kansas: Kansas Geol. Survey, Public Information Circular (PIC) 21.

Schuler, J., 2008, Joint inversion of surface-waves and refracted P- and S- waves: M.S. Thesis, Eidgenössische Technische Hochshule Zurich.

Sheriff, R. E., 2002, Encyclopedic Dictionary of Applied Geophysics, 4th Edition: Society of Exploration Geophysicists.

Siavashpoo, A., and Siahkoohi, H. R., 2012, Simultaneous inversion of fundamental and higher mode Rayleigh wave using sensitivity models: International Geophysical Conference and Oil & Gas Exhibition, Istanbul, Turkey, 17-19 September 2012, 1-4.

Siggins, A. F., 2006, Velocity-effective stress response of CO_2-saturated sandstones: Exploration Geophysics, 37, 98-203.

Sloan, S.D., Miller, R.D., Ivanov, J., Walters, S.L., 2009, Shear wave Velocity as an Indicator of Increased Stress and Failure Potential Associated with Dissolution-Mining Voids: Proceedings of the 22nd Annual Symposium on the Application of Geophysics to Environmental and Engineering Problems, 22, 363-372.

Sloan, S.D., Peterie, S.L., Ivanov, J., Miller, R.D., McKenna, J.R., 2010, Void detection using near-surface seismic methods; in Advances in Near-Surface Seismology and Ground-Penetrating Radar, R.D. Miller, J.D. Bradford, and K. Holliger, eds.: Tulsa, Society of Exploration Geophysicists.

Socco, L. V., Foti, S., Boiero, D., 2010, Surface-wave analysis for building near-surface velocity models—Established approaches and new perspectives: Geophysics, 75, no. 5, A83-A102.

Sofianos, A. I., 1996, Analysis and design of an underground hard rock voussoir beam roof: International Journal of Rock Mechanics, Mining Science, Geomechanics Abstracts, 33, 153-166.

Solution Mining Research Institute, Solution Mining and Cavern Storage; <http://www.solutionmining.org/?title=SolutionMiningandCavernStorage>, accessed: January, 2015.

Spinazola, J. M., Gillespie, J. B., and Hart, R. J., 1985, Ground-water flow and solute transport in the Equus beds area, south-central Kansas, 1940-1979: U.S. Geological Survey, Water-Resources Investigations Report 85-4336, 68.

Stephenson, W. J., Williams, R. A., Odum, J. K., and Worly, D. M., 2005, Comparison of ReMi, and MASW Shear wave velocity techniques with the CCOC borehole to 100 m, Santa Clara Valley: part of U.S. Geological Survey Open-File Report 2005-1169 at [http://pubs.usgs.gov/of/2005/1169.

Stokoe II, K. H., Wright, G. W., Bay, J. A., and Roesset, J. M., 1994, Characterization of geotechnical sites by SASW method: in Woods, R. D., Ed., Geophysical characterization of sites: Oxford Publishers.

Taft, R., 1946, Kansas and the nation's salt: Kansas Academy of Science, Trans., 49, 223-272.

Tasch, P., 1964, Periodicity in the Wellington Formation of Kansas and Oklahoma, Symposium on Cyclic Sedimentation, Merriam, D. F., ed: Kansas Geol. Survey Bull. 169, v. 2, p. 481-496.

Turpening, R. M., 1976, Cavity detection by means of seismic shear and compressional wave refraction techniques: Report 116400-1-F, Environmental Research Institute of Michigan.

Walters, R. F., 1978, Land subsidence in central Kansas related to salt dissolution: Kansas Geological Survey Bulletin 214, 82.

Watabe, Y., and Sassa, S., 2008, Application of MASW technology to identification of tidal flats stratigraphy and its geoenvironmental interpretation: Marine Geology, 252, 79-88.

Watney, W. L., Berg, J. A., Paul, S., 1988, Origin and Distribution of the Hutchinson Salt (Lower Leonardian) in Kansas; *in,* Permian Rock of the Midcontinent, W. A. Morgan and J. A. Babcock, eds.: Midcontinent Society of Economic Paleontologists and Mineralogists, Special Publication 1, 113-135.

Watney, W. L., Byrnes, A. P., Bhattacharya, S., Nissen, S. E., and Anderson, A. K., 2003, Natural gas explosions in Hutchinson, Kansas: Geologic factors [abstract]: Geological Society of America Abstracts with Programs, 35, no. 2, 33.

Watney, W. L., Nissen, S. E., Bhattacharya, S., and Young, D, 2003, Evaluation of the role of evaporite karst in the Hutchinson, Kansas, gas explosions, January 17 and 18, 2001; in K. S. Johnson and J. T. Neal, eds., Evaporite karst and engineering/environmental problems in the United States: Oklahoma Geological Survey Circular 109, 119-147.

Williams, C. C., and Lohman, A. R., 1949, Geology and ground-water resources of a part of south-central Kansas, with special reference to the Wichita municipal water supply: Kansas Geol. Survey, Bull. 79, 455.

Winkler, K. W., 2005, Borehole damage indicator from stress-induced velocity variations: Geophysics, 70, no. 1, F11-F16.

Xia, J., Chen, C., Tian, G., Miller, R. D., and Ivanov, J., 2005, Resolution of high-frequency Rayleigh-wave data: Journal of Environmental and Engineering Geophysics, 10, 99-110.

Xia, J., Miller, R. D., and Ivanov, J., 2007a, Sensitivity of high-frequency Rayleigh-wave data revisited: Society of Exploration Geophysicists, Expanded Abstracts, 77th Annual Meeting, San Antonio, TX, 1142-1146.

Xia, J. H., Miller, R. D., and Park, C. B., 1999, Estimation of near-surface shear wave velocity by inversion of Rayleigh waves: Geophysics, 64, no. 3, 691-700.

Xia, J., Miller, R. D., Park, C. B., Hunter, J. A., and Harris, J. B., 2000, Comparing shear wave velocity profiles from MASW with borehole measurements in unconsolidated sediments, Fraser River Delta, B. C., Canada: Journal of Environmental and Engineering Geophysics, 5, 1-13.

Xia, J., Miller, R. D., Park, C. B., and Tian, G., 2003, Inversion of high frequency surface-waves with fundamental and higher modes: Journal of Applied Geophysics, 52, 45-57.

Xia, J., Nyquist, J. E., Xu, Y., and Roth, M. J. S., 2006a, Feasibility of Detecting Voids with Rayleigh-Wave Diffraction: Symposium on the Application of Geophysics to Engineering and Environmental Problems (SAGEEP 2006), 1168-1180.

Xia, J., Nyquist, J. E., Xu, Y., Roth, M. J., and Miller, R. D., 2007b, Feasibility of detecting near-surface feature with Rayleigh-wave diffraction: Journal of Applied Geophysics, 62, is. 3, 244-253.

Xia, J., Xu, Y., Chen, C., Kaufmann, R. D., and Luo, Y., 2006b, Simple equations guide high-frequency surface-wave investigation techniques: Soil Dynamics and Earthquake Engineering, 26, 395-403.

Xia, J., Xu, Y., Miller, R. D., and Nyquist, J. E., 2006c, Rayleigh-wave diffractions due to a void in the layered half space: SEG Technical Program Expanded Abstracts 2006, 1406-1410.

Yoon, S., and Rix, G., 2004, Combined active-passive surface-wave measurements for near-surface site characterization: Symposium on the Application of Geophysics to Engineering and Environmental Problems (SAGEEP 2004), 1556-1564.

Zeng, C., Xia, J., Miller, R. D., and Tsoflias, G. P., 2009, Modeling results on detectability of shallow tunnels using Rayleigh-wave diffraction: SEG Technical Program Expanded Abstracts 2009, 1425-1429.

Appendix I

Passive MASW Workflow

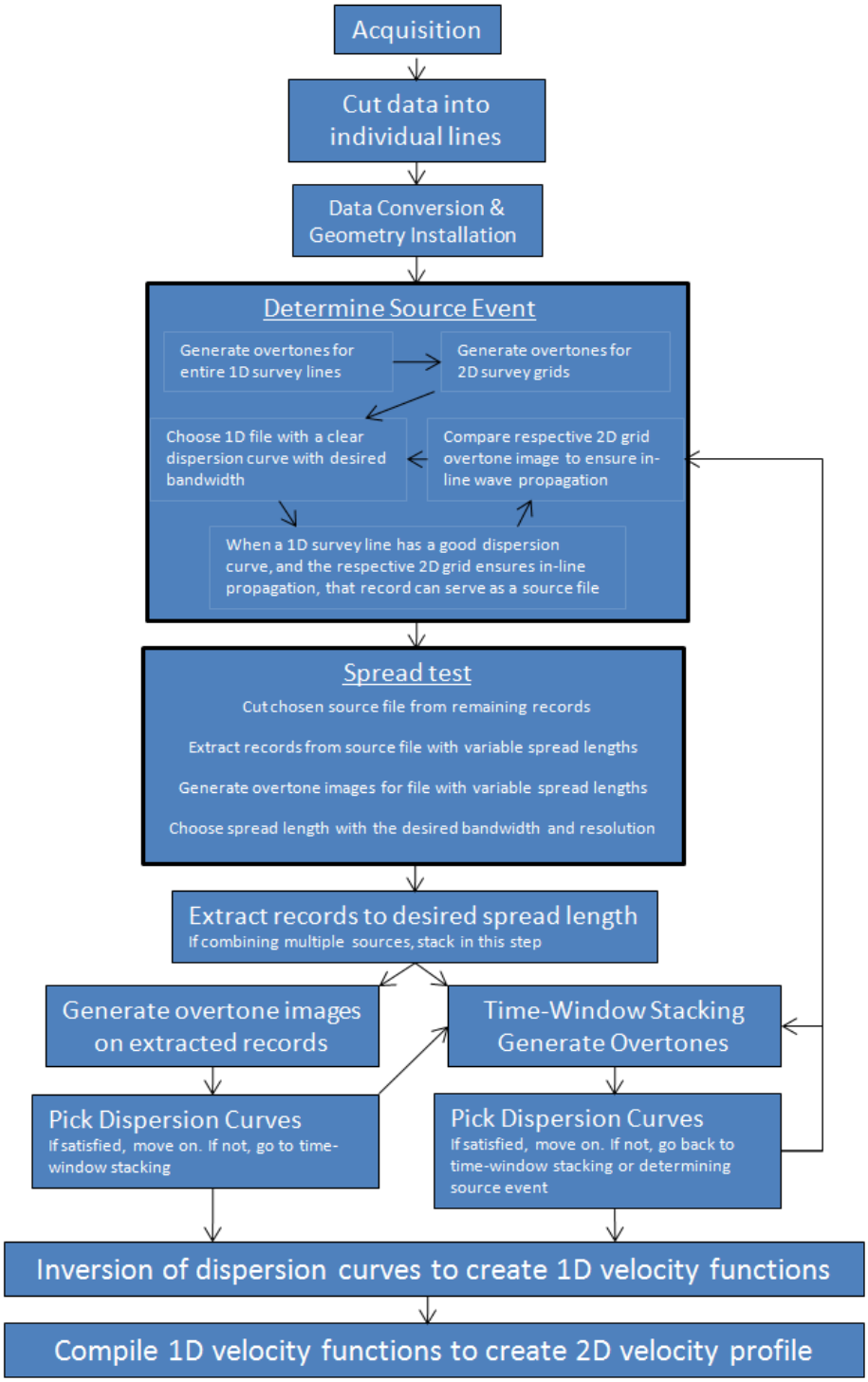

Appendix II

Abbreviations List

1D	One-dimensional
2D	Two-Dimensional
3D	Three-Dimensional
CMP	Common Mid-Point
DC	Dispersion Curve
KGS	Kansas Geological Survey
Hz	Hertz
m	Meter
m/s	Meters/Second
MASW	Multichannel Analysis of Surface-waves
ms	Milliseconds
OT	Overtone Image
P-	Primary, compressional-wave
ReMi	Refraction Microtremor Method
s	Second
S-	Secondary, shear-wave
SASW	Spectral Analysis of Surface-waves
V_P	Compressional-wave velocity
vs	Versus
VSP	Vertical Seismic Profile
V_S	Shear-wave velocity
W1B	Well 1B
W2A	Well 2A
W2B	Well 2B
W3B	Well 3B

W4B	Well 4B
W5B	Well 5B
W6B	Well 6B
W8B	Well 8B
W10B	Well 10B
W11B	Well 11B
W12B	Well 12B
W13B	Well 13B
W14B	Well 14B
W15B	Well 15B
W17	Well 17
W18	Well 18
W22A	Well 22A
W42	Well 42
W45	Well 45
W52	Well 52
W53	Well 53
W59	Well 59
W60	Well 60